Towards Understanding Multicomponent Chemistry Interaction Using Direct Numerical Simulation

Vom Fachbereich Maschinenbau
an der Technischen Universität Darmstadt
zur Erlangung des akademischen Grades
Doktor-Ingenieur (Dr.-Ing.)
genehmigte

Dissertation

vorgelegt von

Dipl.-Ing. Roozbeh Haghighi

aus Tehran

Berichterstatter:	Prof. Dr.-Ing. Johannes Janicka
Mitberichterstatter:	Prof. Dr.-Ing. Peter Stephan
Tag der Einreichung:	25. Februar 2015
Tag der mündlichen Prüfung:	6. Mai 2015

Darmstadt 2015

D17

Acknowledgment

This work was done at the Institute for Energy and Power Plant Technology (EKT) at the Darmstadt University of Technology, under the supervision of the head of department Prof. Dr.-Ing. Johannes Janicka.

My special thanks and appreciation goes to professor Janicka for his support and the opportunity for PhD under his supervision. I am particularly thankful for his trust in me and in my work from the first moment on, and the wonderful discussions we had during this time. Additionally I would also like to mention his insightful lectures on “Sustainable Combustion” and “Modeling of Turbulent Flows”, which I learned a lot from.

I also wish to thank Prof. Dr.-Ing. Peter Stephan, the head of the Institute of Technical Thermodynamics at Darmstadt University of Technology for his willingness to referee my work.

I am indebted to all of the colleagues at the institute. Among them I would especially like to mention the Prof. Dr. rer. nat. Andreas Dreizler and Prof. Dr. rer. nat. Amsini Sadiki who always offered their valubale advice and help. I enjoyed very much the scientific discussions I had with them as well as with many others of whom I would like to mention Ferhat Oezdogan, Samim Doost , Fernando Sacomano, Florian Ries, Chao He and Dr.-Ing. Guido Künne. They all provided the friendly, communicative, and cooperative atmosphere at the institute.

To Dr.ir. Jeroen van Oijen from Technical University of Eindhoven I am grateful for providing me with the code Chem1D and additional supports.

I would most like to thank my roommate Pradeep Pantangi for his inspirations, encouragement, and guidance during the first two years of my research. I am very grateful for his support, patience, and friendship.

I am also thankful to Arash Hosseinzadeh for his friendship, support and being always available to give advice on problems during my PhD. I would also like to thank Mehdi Goodarzi and Ghazal Alipour for spending their leisure time with meticulous revision of the complete manuscript and editing my text. This work would have taken much longer without their support.

I also wish to thank my old friends and buddies back home, Bahram Rafati and Kaveh Ghorbani and also my friend in Bochum, Kamran Azizi.

Finally and most importantly, I appreciate the love, support and encouragement from my parents, sister and brother all the years.

Roozbeh Haghighi Darmstadt, den 25. Februar 2015

Hiermit erkläre ich, dass ich die vorliegende Arbeit, abgesehen von den in ihr ausdrücklich genannten Hilfen, selbstständig verfasst habe.

Roozbeh Haghighi

Darmstadt, den 25. Februar 2015

Contents

Nomenclature

Upper case latin letters

Symbol	Description	Unit
D_{jk}	Binary diffusion coefficient of the species j in species k	m^2/s
D_{km}	Mixture averaged diffusion coefficient of the species k in the mixture	m^2/s
D_{th}	Thermal diffusion coefficient	m^2/s
E_a	Activation energy	J/mol
$F(\psi, t)$	General right hand side of an equaion	-
K_c	Equilibrium constant	$-$
Le_k	Lewis number of the species k	-
N	Number of reactions	-
$\dot{Q}$	External source or sink of the enthalpy	J/m^3s
R	Perfect gas constant	$J/moleK$
S_{ij}	Deformation tensor	$1/s$
S_k	General surface	m^2
T	Temperature	K
T_{ad}	Adiabatic flame temperature	K
U_c	Convective outflow velocity	m/s
V	General volume	m^3
$V_{k,j}$	Diffusion velocity of the species k in direction j	m/s
W	Mean molar mass of the mixture	$kg/kmol$
W_k	Molar mass of the species k	$kg/kmol$
X_k	Mole fraction of the species k	-
Y_k	Mass fraction of the species k	-
Y_{pv}	reaction progress variable	-

Lower case Latin letters

Symbol	Description	Unit
c_p	Specific heat capacity of the mixture at constant pressure	J/kgK
c_{pk}	Specific heat capacity of the species k at constant pressure	$J/molK$
$c_{p_{mix}}$	Specific heat capacity of the mixture at constant pressure	J/kgK
$f_{k,j}$	Volume force acting of the species k in direction j	m/s^2
f	Mixture fraction	-
g_i	Acceleration of gravity in direction i	m/s^2
h	Sensible enthalpy	kJ/kg
h_{ch}	Chemical enthalpy of the mixture	kJ/kg
h_k	Standard enthalpy of the species k	kJ/mol
k_b	Backward reaction constant	$-$
k_f	Forward reaction constant	$-$
m_{tot}	Total mass of the mixture	kg
m_k	Mass of the species k	kg

$\dot{m}$	Mass flux	kg/m^2
n_j	Normal vector to cell surface	-
p_k	Partial pressure of the species k	Pa
q_j	Enthalpy flux in direction j	J/m^2s
q_i	Rate of progress variable for the ith elementary reaction	
s	Mass stoichiometric ratio	-
s_l	Laminar burning velocity	m/s
t	Time	s
x_j or x, y, z	Cartesian coordinates	m
u_j	Velocity in direction j	m/s
$v^{'}$	Stoichiometric coefficient of the species k on the reactant side	-
$v^{''}$	Stoichiometric coefficient of the species k on the product side	-

Upper case greek letters

Symbol	**Description**	**Unit**
$\sum_{k=1}^{N} \Delta h^{\circ}_{f,k}$	Enthalpy of formation of the species k	kJ/mol
ΔH°_{j}	Enthalpy change for reaction j	J
ΔS°_{j}	Enthropy change for reaction j	J/K
Δt	Time step size	s
Δx	Grid size	m

Lower case greek letters

Symbol	**Description**	**Unit**
α_i	Runge-Kutta stage coefficient	-
Γ	General diffusion coefficient	-
δ_f	Flame thickness	m
δ°_{f}	Flame thickness	m
$\epsilon_{\dot{m}}$	Mass lack in the pressure correction scheme	kg/s
ρ	Density of the mixture	kg/m^3
ρ_k	Density of the species k	kg/m^3
λ	Thermal conductivity	W/mK
μ	Dynamic viscosity	kg/ms
μ_k	Dynamic viscosity of the species k	kg/ms
ζ	General coordinate	-
τ_{chem}	Characteristic time for chemical reaction	s
τ_{mix}	Characteristic time for flow	s
τ_{ij}	Components of the viscous stress tensor	kg/s^2m
ϕ	Equivalence ratio	-
ψ	General scalar	-
$\dot{\omega}_k$	Chemical source term of the species k	kg/m^3s

$\dot{\omega}_T$	Heat release rate	W/m^3

Dimensionless numbers

Symbol	**Description**	**Unit**
Da	Damköhler number	-
Le	Lewis number	-
Ma	Mach number	-
Re	Reynolds number	-
Sc	Schmidt number	-

Chapter 1

Introduction

Controlled use of fire was a milestone discovery for humans that served a great evolutionary advantage. Utilization of fire by man first started almost a million years ago; new evidence suggests; and enabled our ancestors to cook their food which would eventually lead to a significant growth in brain size. Fire was also used for heating, defending, illuminating, and ultimately for advanced craftsmanship. It is no overstatement to say that learning how to control and employ fire set the stage for human civilization as we know it today. But as we have evolved, the humble story of fire has turned into an ever more intricate issue of energy which encompasses numerous branches of science and socioeconomic.

Looking at the global figures of energy supply and consumption, despite major concerns about environmental impact and sustainability, fossil fuels have remained by far the main source of energy. At the same time the demand for energy has been steeply on the rise in the past 200 years after the industrial revolution. Due to various technological and financial factors, the consumption patterns, however, have changed from wood, charcoal and coke in the nineteenth century towards oil and natural gas in the twentieth century and in the present time. These trends are going to continue.

The IEA estimates that the *primary energy* consumption is going to increase around 50% by 2030 as compared to 2005. In an alternative scenario suggested by the World Energy Outlook (WEO), it is anticipated that the global energy demand is going to increase by 37% until 2040 as compared to 2014, where in developed countries the energy consumption remains essentially unchanged and the developing countries will face substantially greater demand. The current pace of population and economic growth in China and India alone, indicates that they will soon overtake Europe and the US combined in energy consumption which is to be supplied mostly through fossil fuels.

Currently about 80% of the converted primary energy is provided using fossil fuels (IEA 2012). How long it takes to exhaust all the available fossil energy is unknown. But the most optimistic predictions do not exceed a century for natural gas and oil, and three centuries for coal.

Despite all the effort to develop alternative renewable energies we have not come very far. In the coming 30 years, the primary supply of energy will still consist of oil, gas, coal and low-carbon sources with only slight variations in their share of total consumption. International campaigns have not been much effective either. The signatories of the 1997 Kyoto protocol, among them the most developed countries, are still far from fulfilling their designated commitment to limiting greenhouse gas emissions. Even if the share of fossil fuels were to reduce by 25% compared to the current figures, still it would not be enough to stabilize the greenhouse effect. Keeping its current pace, the carbon dioxide emission into the atmosphere is bound to result in an average increase of 3.6 Celsius of global temperature by the 2040, while it is critical to keep this temperature increase less than 2 Celsius in order to avoid catastrophic climate changes. For this, the annual CO_2 emission worldwide must not exceed 1000 giga tonnes after 2014. Other organizations have set even stricter target values for emissions. ACARE, the Advisory Council of Aeronautical Research in Europe, aims to reduce the CO_2 emission by 20%, the NO_x by 80% per passenger [39].

These facts set forth two major challenges, namely the limitation of energy sources, and the greenhouse gas emissions. As fossil fuels deliver their energy through combustion, an immediate technical response to these issues would be to investigate the combustion processes thoroughly, in order to improve efficiency and in order to better understand the underlying reactions that result in emissions. This line of research encompasses a broad range of combustion devices employed in various technical and industrial contexts from combustion chambers in aero-engines, gas turbines, and furnaces all the way to internal combustion engines, to name a few.

Considering the methodologies, experimental methods play an important role in fluid dynamic research, especially when it comes to combustion. Empirical tests of prototypes and scaled models are still the most reliable and the least dispensable parts of this body of research, whenever available. It must be noted, however, that it is very improbable, if not impossible, to experimentally investigate real combustion devices in detail due to the very high costs and eventually due to technical limitations of measurement instruments and methods. Fortunately for us, the rapid advancement of computational technology specially in the last two decades, has made it possible to simulate such complicated cases numerically. Computational fluid dynamics is becoming ever more popular because of its efficiency. This has paved the path to obtaining a deeper insight into complex flows to the extent that we are able to build computational models that can predict characteristics of thermo-fluid phenomenon. At the very least where conducting experiments is an absolute requirement, one can reduce the number of expensive prototypes and trials if a proper computational simulation is carried out beforehand.

From a mere computational perspective, one has to keep in mind that simulation of reacting flows is no rudimentary task even in simpler cases such as isothermal regimes. And it becomes more challenging where energy and species transport together with molecular and turbulent diffusion and various other factors have to be considered in order to establish more realistic models. Such complex formulations require immense computation capacities that were not available until recently.

The availability of affordable high performance computing has enabled the researchers to tackle the direct numerical simulation (DNS) of technical combustion devices; a deed far beyond imagination even a decade ago. DNS is becoming more favored in computational combustion [46, 50, 17, 16], because the computation takes place at the smallest length scales and no sub-grid scale models are included. Therefore the results are considered to be reliable enough to be a viable alternative for experimens and potentially an effective substitute in providing the validation data for simpler methods such as Reynolds-averaged Navier-Stokes (RANS) or Large Eddy Simulation (LES). DNS also provides calibration data for experimental measurements. And in the areas where experiments are rendered ineffective, due to aforementioned issues, direct numerical simulation appears as the best possible solution.

One of such areas where measurements have very limited applicability is the so called *near-wall combustion*. This topic is of high significance in combustion research since the flame is controlled by solid walls in most technical combustion devices e.g. combustion chambers and internal combustion engines. Among the myriad of aspects to this problem is the maximum allowable temperature imposed by thermal strength of the solid wall material. To avoid material failure due to overheating, designers implement cooling mechanism at the walls. This cooling process causes a heat flux within the flame at the vicinity of the wall. This heat flux has substantial impact on the chemical pathways and mechanism of near-wall combustion. Even slight changes of the chemical pathway may result in radical recombination and species accumulation at the wall, as well as unburnt hydrocarbon (UHC) and consequently elevated emission of pollutant gases.

In recent years the automobile and aviation industries, as well as other energy intensive branches, have moved towards *downsizing* as a new trend. Downsizing essentially means to reduce the dimensions of the device while power and efficiency is kept at least the same. The immediate consequence of downsizing for combustion devices is a higher area-to-volume-ratio in which case the near-wall combustion attains greater influence on the overall behavior of the device. On these accounts, the near-wall combustion and the flame-wall interaction becomes an increasingly attractive area of scientific investigation.

1.1 Flame-wall interaction, state of the art

The first major technical application of flame-wall interaction goes back to almost two hundred years ago in 1815 when Sir Humphery Davy invented a mine lamp which worked based on flame-wall interaction in a channel, which is called tube quenching now. A systematic research concerning flame-wall interaction, however, was not reported until 1950 when Friedman and Johnston [40, 41] tried to measure the dependency of the quenching distance of propane-air mixture on pressure and temperature. With the available measurement instruments at the time, they found that this distance is about $2mm$.

There is consensus among the workers of the field that the unwanted byproducts of combustion, like unburnt hydrocarbons and $\mathrm{NO_x}$, are the result of inefficient combustion mostly in locations where flame and wall interact (they do not interact everywhere) [29]. The aforementioned downsizing boosts these effects even further.

Another important topic is the thermo-chemical interaction between the flame and the wall, dictated by thermomechanical design requirements. The adiabatic flame temperatures normally exceed the allowable temperatures for the typical metallic walls surrounding flames in combustion devices. This requires that a carefully designed cooling system encloses the walls to keep the operating temperatures within the bounds of thermal strength. Daniel [27], Bellenoue et al. [6], and Popp et al. [103] show that flame-wall interaction relates strongly to high heat fluxes toward the wall. One can generally imagine that the flame propagates toward the wall, consumes the unburned fuel-oxidator mixture, reaches a cold wall and during this process gives the wall some amount of heat, cools down in this zone and eventually quenches. It is presupposed that radical recombination is responsible for quenching during the interaction between flame and the cold wall.

Flame-wall interaction can happen in both turbulent and laminar flow regimes. Poinsot et al.[102] studied the laminar premixed FWI numerically, while Whichman carried out a theoretical study [129]. There is also a host of experimental investigations of FWI [9, 10, 42, 133, 89, 124, 61, 60].

Flame-wall interactions in full-scale combustion devices are complex to such degree that in most situations a real physical understanding is very hard to achieve. This is mainly due to multitude of parameters and also due to the nonlinearities involved. To mention a few of these numerous parameters, for instance, one could consider the influence of equivalence ratio, the effect of wall temperature, the impact of pressure.

There are some studies in which the net mass fraction rate of produced UHCs are investigated [54, 67, 128]. Heat flux to the wall is studied by Popp et al. [103] and Owston et al. [93] numerically, and by Sotton et al. [114], Ezekoye et al. [35], and by Connelly [24, 25] experimentally. There are works in which hydrogen flame interactions with the walls have been looked into, for instance Dabireau et al. [26] and Owston et al. [93]. A three-dimensional DNS was carried out by Gruber et al. [46].

The behavior of flame near the wall for various hydrocarbon fuels has been thoroughly explored by Boust et al. [11] who performs simulations based on simple chemistry, and by Westbrook et al. [128] and Hasse et al. [49] who ran similar simulations based on detailed chemistry for methane and higher hydrocarbons. How the wall and flame interact at different inlet temperatures is examined by Westbrook et al. [128] and by Wu et al. [134]. Research on the influence of the wall temperature is done by Owston et al. [93], Owston and Abraham [94], and Popp et al. [103]. Sotton et al. [114] examined the impact of the pressure on the heat flux toward the wall. This same topic has been later researched by Owston et al. [93] and many others [40, 75, 7, 84, 45, 117, 117].

There are cases where the wall is directly involved in the reaction. This has been inspected and theorized. Among others Popp showed that the rate of heat release at the wall decreases if the surface chemistry is account for [104]. The equivalence ratio and its influence on near-wall combustion has been looked into by Vosen et al. [123], Ezeyoke et al. [37], and others [11, 40, 87, 31, 45, 48, 86, 35, 37, 58, 59, 55, 123, 80, 18].

Quenching is a major topic FWI research. This phenomenon is classified based on the configuration of the combustion device into Head-on quenching and side wall quenching. These will be described extensively in the sequel. The head-on configuration has been studied theoretically by Wichman and Bruneaux [129] and by Boust et al. [11], and numerically by Popp and Baum [103], Westbrook et al. [128], Poinsot et al. [102], Hasse et al. [49], Wu et al. [134], Owston et al. [93]. Owston and Abraham [94] and Huang et al. [55] consider different parameters involved in near wall combustion. On the side wall quenching, however, there are still many open issues yet to be researched. There is some analytical work by von Kármán, Millan [62], and Makhviladze and Melikov [85]. Lu et al. [80] and Clendening et al. [23] conducted almost similar experiments regarding side wall quenching. Numerically, the side wall quenching has been investigated to some extent by Gruber et al. [46], and Gruber and Chen [47].

Various parameters have been investigated in head-on and side-wall quenching. Especially, there is abundant theoretical, experimental, and numerical research about the head-on configuration. There are, however, much fewer works concerning the side-wall configuration, either in laminar or in turbulent regimes. Despite the myriad of experimental studies on the subject, the high costs of setups and complexity of FWI hinders a comprehensive empirical work. Short time scales and small characteristic length scales require especially high-precision measurements in this case. Since, for instance, the flame quenching distance at atmospheric pressure is of the order of 100 micrometer and less, there are no reliable experiments for capturing the flame wall interaction at this time. This leaves CFD as the only feasible option which has only become possible by the arrival of the recent computing technologies. One would say that the role of computational fluid dynamics is getting more pronounced than ever in areas of fluid dynamics research where complexity has been unsurmountable so far.

Gruber et al. [46] has recently performed a three-dimensional direct numerical simulation on the interaction of the wall with a turbulent hydrogen-air flame using multi-component reaction mechanism. Before that, most of the reports are either experimental and theoretical. Limited numerical works were performed using simple chemistry. For instance Alshaalan et al. [1] tried to study turbulent premixed flame interactions with a wall in a Couette channel flow and performed some DNS only for a single-step reaction where heat release is emplyed. Long before that, Ezekoye [36] performed some DNS and tried to characterize the side-wall quenching configuration.

1.2 Objective of the present work

We carry out a quasi-three-dimensional direct numerical simulation to investigate the side-wall quenching configuration of a laminar premixed methane-air flame. The authors do not know of any previous reports on direct numerical simulation of methane-air mixture using detailed chemical kinetics that provides a comprehensive investigation of similarities and differences between the head-on and side-wall quenching in a systematic way. We suspect that the reason is the cost of computation. Although HOQ simulations can be performed using one-dimensional finite difference method, the side-wall quenching has to be simulated in two dimensions for laminar combustion and in three dimensions in the turbulent case. The goal of this work is first to investigate the flame-wall interaction in the head-on quenching configuration concerning different phases of simulation where the flame behaves differently from the transient phase exactly after simulation until after quenching. Secondly, the amount of produced carbon monoxide in different distances from the wall will be examined and compared to experiments. The last step is to gain better insight into the side-wall quenching of stoichiometric methane-air mixtures in configurations where the wall is parallel to the flow.

1.3 Outline of this writing

The basic theoretical background on mathematical description of reacting flows and the equations describing them are given in the next chapter. After that, in chapter 3, the chemical kinetics and the theory of combustion is explained. Chapter 4 is dedicated to numerical treatment of equations provided in chapter 2, as well as the basic explanations of the temporal and spatial discretization methods utilized. Chapter 5 presents the simulations used to verify the implementation in different applications and in 1D and 2D geometries.

Chapter 6 is devoted to application of FASTEST-3D which is equipped with detailed chemistry to analyze the stratified flames. In chapter 7 the near wall combustion or the so called flame-wall interaction will be explored using two completely different possible quenching configurations and next, their similarity and differences will be studied. In the final chapter the whole work and its results will be summarized and some ideas of possible extensions will be laid down.

Chapter 2

Mathematical Description and Modeling of Flows

As everyone knows the velocity of a solid body can be easily described. To define the velocity of a fluid flow, one should take more care. Generally, a fluid consists of lots of molecules moving with higher degree of freedom comparing to those of a solid body, so that theoretically for each molecule a velocity can be defined.

Practically, it does not make sense to have such amount of velocities to be considered. Alternatively the velocity field of a fluid as an average velocity of the fluid at each point of each molecule can be defined. This is allowed if the velocity field is represented as a continuum field. Here should the Knudson number, Kn be described which is a dimensionless number, defined as the ratio of the molecular mean free path length to the smallest physical length scale to be resolved.

A field is represented as continuum if the Knudson number is less than 0.1. This means if there are enough molecules in a given fluid packet, one can measure macroscopic variables to define the fluid characteristics. Depending on application, the fluid packet can be considered as continuum or not. In most of the technical applications as well as in this work, continuum hypothesis is satisfied and accordingly flow field can be assumed continuum.

In this chapter the equations through which the flow field can be described will be given. then the changes needed to simulate the reacting flow with multi species mechanism are provided. These equations are Navier-Stokes equations which are continuity and momentum equations, state equations. Then the energy transport equation and scalar transport equation are provided and the changes needed will be extensively explained. The latter equation provides mass fraction Y_k of each species participating in reaction.

2.1 Basic equations for gas mixtures

Generally, to be able to investigate a reacting flow numerically, variables characterizing the flow, energy and chemical changes must be calculated through some coupled transport equations stated above as well as through a second group of equations called state equations. Since we just consider reacting flow in gas phase, gas is considered as a mixture consisting of different species.

2.1.1 Thermochemistry

As said above, to describe the reacting flows, as well as the transport equations some additional terms should be applied so before providing other transport equations it is better to discuss the thermochemistry considering a reacting mixture in gas phase.

2.1.1.1 Mass fraction

A reacting mixture consists of different species that can be characterized through mass fraction Y_k as follows:

$$Y_k = \frac{m_k}{m_{tot}} \tag{2.1}$$

Y_k delivers the mass percentage of species k in the mixture. m_k and m_{tot} denote the mass of species k in the noted volume element and the total mass of the mixture in the same element.

2.1.1.2 Mean molar mass

Based on this definition, the mean molar mass of the mixture can be defined as follows:

$$W = \frac{1}{\sum\limits_{k=1}^{N} \frac{Y_k}{W_k}} \tag{2.2}$$

in which W is the mean molar mass and W_k is the molar mass of the species k.

2.1.1.3 Mole fraction

It is common in combustion literature and especially in experimental measurements to use mole fraction of the species instead of mass fraction. This can be easily derived from mass fraction as follows:

$$X_k = Y_k \frac{W}{W_k}. \tag{2.3}$$

Analog to previous extraction of the mean molar mass, we can extract the mean molar masses having mole fractions of the species:

$$W = \sum_{k=1}^{N} X_k W_k \, . \tag{2.4}$$

2.1.1.4 Pressure and density of a mixture

Using the thermal equation of state for each species in the gas mixture, one can obtain the pressure of each species in the mixture:

$$p_k = \rho_k \frac{R}{W_k} T \, , \tag{2.5}$$

where p_k and ρ_k and T are the pressure in $[Pa]$ and the density in $[kg/m^3]$ of the each specie in the mixture and temperature in $[K]$ respectively and $R = 8.314 J/molK$ is the prefect gas constant. Having this, one is able to get pressure of the mixture and consequently the density of the mixture:

$$p = \sum_{k=1}^{N} p_k \,, \tag{2.6}$$

$$\rho = \frac{pW}{RT} \,. \tag{2.7}$$

2.1.1.5 Heat capacity

Heat capacity of a gas phase mixture at constant pressure can also be derived from specific heat of each species. To get the latter, one way is to use the gas phase thermochemistry data bases and extract the coefficients which are needed to calculate the suggested polynomial as a function of temperature. As an example the polynomial suggested in NIST web book[79]

$$c_{pk} = A + BT + CT^2 + DT^3 + E/T^2 \tag{2.8}$$

which delivers the c_{pk} in $[J/molK]$. Having c_{pk} of each species, the $c_{p_{mix}}$ of the mixture can be simply calculated using:

$$c_{p_{mix}} = \sum_{k=1}^{N} c_{pk} \frac{Y_k}{W_k} \quad Jkg^{-1}K^{-1} \tag{2.9}$$

2.1.1.6 Different kinds of enthalpy

There are different ways to represent energy for a reacting flow. In this work, **Sensible enthalpy**, **Chemical enthalpy** and **Sensible+Chemical enthalpy** are used.

Sensible Enthalpy

Similar to heat capacity, to calculate the sensible enthalpy of each species of a gas mixture, one can get the coefficients from a thermodynamic data base like those provided by NIST [79]

$$h_k - h_{k298[K]} = AT + \frac{BT^2}{2} + \frac{CT^3}{3} + \frac{DT^4}{4} + \frac{E}{t} + F - H \,, \tag{2.10}$$

where h_k is the standard enthalpy of species k in $[kJ/mole]$ and T is the temperature in $[K]$. Sensible enthalpy of the mixture can be easily calculated from the sensible enthalpy and the mass fraction of each species

$$h = \sum_{k=1}^{N} h_k \frac{Y_k}{W_k} \,. \tag{2.11}$$

Chemical enthalpy

Chemical enthalpy of a mixture can be calculated analogous to the sensible enthalpy as follows

$$h_{ch} = \sum_{k=1}^{N} \Delta h^{\circ}_{f,k} \frac{Y_k}{W_k} \,, \tag{2.12}$$

where $\Delta h^{\circ}_{f,k}$ and h_{ch} are enthalpy of formation of the species k in $[kJ/mole]$and chemical enthalpy of the mixture in $[kJ/kg]$

2.1.2 Gas phase multi-component transport properties

To describe the characterization of the molecular transport, momentum and energy of each species in a multicomponent gas mixture, one needs to determine thermal conductivities, viscosities, diffusion coefficients and also thermal diffusion. Before explaining these variables, it is better to introduce the Le number which is a unit-less number that compares D_{km}, the diffusion coefficient of species k in the mixture and thermal diffusion coefficient D_{th},

$$Le_k = \frac{\lambda}{\rho c_p D_{km}} = \frac{D_{th}}{D_{km}} \,, \tag{2.13}$$

with

$$D_{th} = \frac{\lambda}{\rho c_p} \quad m^2 s^{-1} \,, \tag{2.14}$$

where λ is the thermal conductivity. Le_k is a local variable but in most of the gas mixtures, it is varying by a few percent in the flame [53]. Depending on application and the simulation setting, different codes may use different settings/simplifications for transport properties. These settings are based on Le number whether it is equal to unity or different from unity. In this work, the simulations with **Le=1** and **Mixture averaged transport coefficients** were performed which will be explained briefly. For more information see [53] or [64].

2.1.2.1 Le=1

Setting $Le = 1$ means assuming equality of diffusion coefficients of all of the species to thermal diffusion coefficient. To obtain this, the thermal conductivity and dynamic viscosity need to be specifically treated so that this assumption is satisfied. To be able to verify the code with the results gotten by "Chem1D" [120], λ and μ are calculated by temperature dependent polynomials suggested by Smooke et. al. [111] implemented by van Oijen in "Chem1D" for methane-air mixture. Hence,

$$\lambda = 2.58 \times c_{p_{mix}} \times 10^{-5} (\frac{T}{298K})^{0.69} \quad J s^{-1} m^{-1} K^{-1} \,, \tag{2.15}$$

$$\mu = 1.67 \times c_{p_{mix}} \times 10^{-8} (\frac{T}{298K})^{0.51} \quad kg s^{-1} m^{-1} \,. \tag{2.16}$$

Herein the μ is the dynamic viscosity. Having these, based on the formula for Le number equal to unity, one can derive D_{th} and D_{km}.

2.1.2.2 Mixture averaged transport coefficients

As it can be obviously understood from the name of this formulation, to get mixture averaged transport coefficients needs calculating the averaged values of thermal conductivity, dynamic viscosity, specific heat and thermal diffusion of the gas mixture as well as the diffusion coefficient of each species in the whole mixture in each specific point of the domain has to be determined.

To calculate the properties in mixture averaged formulations, first μ and λ of the pure species and the binary diffusion coefficients for each pair of species has to be determined using a polynomial fit of the logarithm of the property versus the logarithm of the temperature implemented in TRANSPORT sub-packet [63] of PREMIX [65]. For viscosity,

$$ln\mu_k = A_{\mu,k} + B_{\mu,k} lnT + C_{\mu,k}(lnT)^2 + D_{\mu,k}(lnT)^3 \,, \tag{2.17}$$

where μ_k, $A_{\mu,k}$, $B_{\mu,k}$, $C_{\mu,k}$ and $D_{\mu,k}$ are the dynamic viscosity of the pure species k, the coefficients taken from the polynomial fit and T is the temperature in $[K]$ respectively. Similar to viscosity, the thermal conductivity can be also determined using

$$ln\lambda_k = A_{\lambda,k} + B_{\lambda,k} lnT + C_{\lambda,k}(lnT)^2 + D_{\lambda,k}(lnT)^3 \,, \tag{2.18}$$

in which λ_k is the thermal conductivity of the pure species k and the coefficients A, B, C and D are obtained using a polynomial fit.

Calculating the mixture averaged diffusion coefficients is more complicated. Here, polynomial fits for each pair of species have to deliver the binary diffusion coefficients between each pair

$$lnD_{jk} = A_{jk} + B_{jk} lnT + C_{jk}(lnT)^2 + D_{jk}(lnT)^3 \,, \tag{2.19}$$

where D_{jk} is the diffusion coefficient of the species j in species k and A_{jk}, B_{jk}, C_{jk} and D_{jk} are similarly gotten from fitting procedure. Having binary diffusion coefficients and the pure species properties, one can compute the mixture averaged diffusion coefficients using Hirschfelder and Curtiss [53] approximation as follows:

$$D_{km} = \frac{1 - Y_k}{\sum\limits_{j \neq k}^{N} X_j / D_{jk}} \,. \tag{2.20}$$

D_{km} represents the diffusion coefficient of the species k into the rest of the mixture.

Wilke [130] suggested a semi-empirical formula for computing mixture averaged dynamic viscosity from dynamic viscosities of pure species of a mixture. This has been modified later by Bird et al. [8] which is given by

$$\mu = \sum_{k=1}^{N} \frac{X_k \mu_k}{\sum\limits_{j=1}^{N} X_j \Phi_{kj}} \,, \tag{2.21}$$

with μ representing the mixture averaged viscosity and Φ being calculated from

$$\Phi_{kj} = \frac{1}{\sqrt{8}} \left(1 + \frac{W_k}{W_j}\right)^{-\frac{1}{2}} \left(1 + \left(\frac{\mu_k}{\mu_j}\right)^{\frac{1}{2}} \left(\frac{W_j}{W_k}\right)^{\frac{1}{4}}\right)^2 \,. \tag{2.22}$$

In a similar fashion, the mixture averaged thermal conductivity can be determined by the formulation suggested by Bird et al. [8] as

$$\lambda = \frac{1}{2} \left(\sum_{k=1}^{N} X_k \lambda_k + \frac{1}{\sum\limits_{k=1}^{N} X_k / \lambda_k} \right) \,. \tag{2.23}$$

2.2 Conservation equations

2.2.1 Conservation of mass

Let us consider an infinitesimal volume of fluid which still satisfies the continuum hypothesis. In this volume as long as there is no nuclear reaction leading to mass production, there will be neither mass destruction nor production. So that the conservation of mass will be delivered as follows:

$$\frac{\partial \rho}{\partial t} + \frac{\partial}{\partial x_j}(\rho u_j) = 0\,, \tag{2.24}$$

where ρ and u_j are density and three velocity components respectively. This relation means the temporal changes of mass in the given volume element is equal to the sum of the mass fluxes in all three directions through that element. Here, it should be noticed that there is no difference between above equation and the continuity equation written for a non-reacting flow.

2.2.2 Conservation of momentum

Again consider the infinitesimal continuum volume element of fluid. The conservation of momentum is nothing but applying the second law of Newton to this fluid element. Writing the transport equation for the ρu_i gives

$$\frac{\partial}{\partial t}(\rho u_i) + \frac{\partial}{\partial x_j}(\rho u_i u_j) = \frac{\partial}{\partial x_j}\tau_{ij} - \frac{\partial p}{\partial x_i} + \rho g_i \qquad i,j \in \{1,2,3\}\,, \tag{2.25}$$

where ρu_i is the momentum of the given fluid element, g_i is the gravity force which represents a body force and τ_{ij} is the stress tensor. This equation declines that the temporal change of the momentum ρu_i in the continuum fluid element is equal to the sum of convective transport of ρu_i with the convective velocity u_j, the stress acting on the fluid element τ_{ij}, pressure and body forces (here just gravity force) to the fluid element.

Based on Stokes hypothesis [115] and the assumption Newtonian fluid, the stress tensor τ_{ij} can be defined as

$$\tau_{ij} = \mu\left(2S_{ij} - \frac{2}{3}\frac{\partial u_k}{\partial x_k}\delta_{ij}\right)\,, \tag{2.26}$$

where S_{ij} is the deformation tensor and is equal to

$$S_{ij} = \frac{1}{2}\left(\frac{\partial u_i}{\partial x_j} + \frac{\partial u_j}{\partial i_i}\right)\,. \tag{2.27}$$

Hence, the transport equation of the momentum can be rewritten as follows

$$\frac{\partial}{\partial t}(\rho u_i) + \frac{\partial}{\partial x_j}(\rho u_i u_j) = \frac{\partial}{\partial x_j}\left(\mu\left(\frac{\partial u_i}{\partial x_j} + \frac{\partial u_j}{\partial i_i}\right) - \frac{2}{3}\mu\frac{\partial u_k}{\partial x_k}\delta_{ij}\right) - \frac{\partial p}{\partial x_i} + \rho g_i\,. \tag{2.28}$$

This equation delivers three equations in all three space directions i, j, k. They together, along with continuity equation, are the so called **Navier-Stokes** equations.

2.2.3 Transport equation for species

In a gas mixture of a reacting flow, there are different species consisting of the reactants, products and radicals or intermediate species. To investigate the behavior of these species in detail one should write the transport equation for all of these species. Assume m_k is the mass of each species in gas mixture consisting N species and m the total mass of the mixture. According to the continuity equation for the mass, the total mass must be conserved, we have

$$\sum_{k=1}^{N} m_k = m\,, \tag{2.29}$$

and also consequently

$$\sum_{k=1}^{N} Y_k = 1\,. \tag{2.30}$$

Having this, one can easily interpret that the transport equation of the species could be nothing but a rewritten form of the conservation equation of the mass. Hence

$$\frac{\partial}{\partial t}(\rho Y_k) + \frac{\partial}{\partial x_j}(\rho(u_j + V_{k,j})Y_k) = \dot{\omega}_k \quad \text{for} \quad k = 1, \dots, N\,, \tag{2.31}$$

is the transport equation for each species of the mixture. In this equation the first term represents the temporal change of the mass fraction of the species k, the first part of the second term $\frac{\partial}{\partial x_j}(\rho u_j Y_k)$ shows the convective flux of this species,V_k is the diffusion velocity of the species k and $\dot{\omega}_k$ source term/reaction rate of the species k. Again here to satisfy the continuity, it can be derived that

$$\sum_{k=1}^{N} \dot{\omega}_k = 0\,. \tag{2.32}$$

How to calculate the reaction rates will be later explained in the chapter 3.

Diffusion velocities follow also the same rule to fulfill the conservation of mass. Hence,

$$\sum_{k=1}^{N} V_{k,j} Y_k = 0\,. \tag{2.33}$$

To obtain the diffusion velocities V_k of the N species a complicated equation system of size N^2 must be solved [131]. This needs a huge computing capacity [33]. For most of the codes, more simplified forms of diffusion velocity are implemented and reduced to

$$V_{k,j} Y_k = -D_k \frac{\partial Y_k}{\partial x_j}\,, \tag{2.34}$$

which is an approximated version of diffusion coefficients by Fick's Law and very easy to implement in combustion codes. D_k can be computed depending on the complexity of the calculation method of the transport properties (as said in the previous section) through formulation for $Le = 1$ assumption which means constant diffusion coefficient for all of the species or mixture averaged formulation or other methods like the setting different *Le* numbers for each species.

For multi-component systems using Hirschfelder approximation, the Fick's law for the diffusion coefficients has to be slightly changed as suggested by Poinsot et al. [101], so that the transport equation for the species can be rewritten as

$$\frac{\partial}{\partial t}(\rho Y_k) + \frac{\partial \rho u_j Y_k}{\partial x_j} = \frac{\partial}{\partial x_i}\left(\rho D_{km}\frac{W_k}{W}\frac{\partial X_k}{\partial x_j}\right) + \dot{\omega}_k \,, \tag{2.35}$$

where X_k is the mole fraction of the species k. In this system to satisfy the global mass conservation and also to prevent the over determination of the equation system, one can solve the continuity equation and $N-1$ out of N transport equations for all of the species mass fractions. The last species will be usually the inert one! Mostly, Nitrogen is chosen. The mass fraction of the Nitrogen can be determined through

$$Y_{N2} = 1 - \sum_{k=1}^{N-1} Y_k \,. \tag{2.36}$$

This relaxes the possible inconsistencies which could occur regarding mass conservation because of using Hirschfelder approximation [101].

2.2.4 Enthalpy balance

As mentioned before, the aim of this work is to investigate the flame/reacting flow-wall interaction. The most important parameter distinguishing a reacting flow from a normal cold non-reacting aerodynamic flow is the temperature/enthalpy gradient within the flow. Besides, one of the most interesting parameter to be examined in the near wall combustion is the heat flux at the wall which can be also determined having enthalpy/temperature behavior in the flow near wall.

In the literature, different types of possible variables are described to represent the energy [15, 121, 113, 95, 96, 57, 56], among which the sensible energy/enthalpy, chemical energy/enthalpy, and the sum of sensible and chemical enthalpies can be mentioned. They are applied based on the application and type of the code (compressible/incompressible)(for more information see [3, 21, 38, 52, 68, 122, 101].

In the code used for this work, the sensible enthalpy is transported and also the sum of sensible and chemical enthalpies is used for post-processing. The enthalpy h_k of the species k in a gas mixture can be expressed as

$$h_k = \int_{T_0}^{T} c_{pk} dT + \Delta h_{f,k}^0 \,. \tag{2.37}$$

This has two terms on the right-hand-side. The first term in this relation represents the share of h_s, the sensible enthalpy in the total enthalpy of the species k. T_0 is the reference temperature at which usually the sensible enthalpy is set to zero (Consider that here just the sensible enthalpy is set to zero and not all other forms of it). h_s is calculated adding the sensible enthalpies of the species k for each infinitesimal temperature interval from a reference temperature to a given temperature.

The second term of this equation is the so called chemical enthalpy and serves as the mass enthalpy of formation of the species k at the reference temperature T_0. The **Chemical+Sensible** enthalpy of the gas mixture can also be calculated following the weighing method previously used for other parameters. Hence

$$h = \sum_{k=1}^{N} h_k \frac{Y_k}{W_k} \,. \tag{2.38}$$

It is also possible to sum the chemical enthalpies of all of the species and add it to the sensible enthalpy at the same time

$$h = \int_{T_0}^{T} c_p dT + \sum_{k=1}^{N} \Delta h_{f,k}^{0} Y_k \,, \tag{2.39}$$

but here it should be considered the heat capacity c_p is that of the mixture and not of a specific species. Knowing these, the energy conservation equation in the form of enthalpy can be written as

$$\frac{\partial}{\partial t}(\rho h) + \frac{\partial}{\partial x_j}(\rho u_j h) = \frac{Dp}{Dt} + \tau_{ij}\frac{\partial u_i}{\partial x_j} + \dot{Q} + \rho \sum_{k=1}^{N} Y_k f_{k,j} V_{k,j} - \frac{\partial q_j}{\partial x_j} \,. \tag{2.40}$$

Where the first term of the RHS represents the production of enthalpy due to pressure changes in the domain and the second term serves as viscous heating source term. $\dot{Q}$ is the external heat source term (not to be mistaken for heat reaction rate) which is the case, if there is an electric spark igniter or if radiation is considered. The next term is the power produced by body forces $f_{k,j}$. The last term on the RHS, q_i represents the energy flux and can be expanded as

$$q_j = -\lambda \frac{\partial T}{\partial x_j} + \rho \sum_{k=1}^{N} Y_k h_k V_{k,j} \tag{2.41}$$

This is the complete form of the transport equation of energy for the enthalpy.

Since in this work the sensible enthalpy is transported, we convert the equation using the relation $(h_s = 1 - \sum_{k=1}^{N})\Delta h_{f,k}^{\circ} Y_k$, the conservation equation of energy can be rewritten in the form of sensible enthalpy

$$\begin{aligned} \frac{\partial}{\partial t}(\rho h_s) + \frac{\partial}{\partial x_j}(\rho u_j h_s) =& \frac{Dp}{Dt} + \tau_{ij}\frac{\partial u_i}{\partial x_j} + \rho \sum_{k=1}^{N} Y_k f_{k,j} V_{k,j} + \\ & \frac{\partial}{\partial x_j}\left(\lambda \frac{\partial T}{\partial x_j}\right) - \frac{\partial}{\partial x_j}\left(\rho \sum_{k=1}^{N} Y_k h_{s,k} V_{k,j}\right) + \dot{\omega}_T \,, \end{aligned} \tag{2.42}$$

where $\dot{\omega}_T$ is the heat release rate and can be calculated from

$$\dot{\omega}_T = -\sum_{k=1}^{N} \Delta_{f,k}^{\circ} \dot{\omega}_k \,. \tag{2.43}$$

As stated earlier the way $\dot{\omega}_k$ is calculated will be later described in detail in the next chapter.

The transport equation of sensible enthalpy can be simplified if the so called **low Mach number assumption** [101] is applied so

$$\frac{Dp}{Dt} \approx 0, \quad \textit{and} \quad \tau_{ij}\frac{\partial u_i}{\partial x_j} \approx 0\,. \tag{2.44}$$

If there is also no volume force (which is the case in this work) the third term of the RHS can be also eliminated

$$\rho \sum_{k=1}^{N} Y_k f_{k,j} V_{k,j} \approx 0\,. \tag{2.45}$$

So after applying all these simplifications, the whole equation can be rewritten in the simplified form as follows

$$\frac{\partial}{\partial t}(\rho h_s) + \frac{\partial}{\partial x_j}(\rho u_j h_s) = \frac{\partial}{\partial x_j}\left(\lambda \frac{\partial T}{\partial x_j}\right) - \frac{\partial}{\partial x_j}\left(\rho \sum_{k=1}^{N} Y_k h_{s,k} V_{k,j}\right) + \dot{\omega}_T\,. \tag{2.46}$$

And this closes the system of governing equations for our simulations. Now, in order to obtain an overall view we put all of these equations together.

2.3 Formulation of reacting flows

2.3.1 Simplified formulation, Le=1

- Conservation of mass

$$\frac{\partial \rho}{\partial t} + \frac{\partial}{\partial x_j}(\rho u_j) = 0 \tag{2.47}$$

- Conservation of momentum

$$\frac{\partial}{\partial t}(\rho u_i) + \frac{\partial}{\partial x_j}(\rho u_i u_j) = \frac{\partial}{\partial x_j}\left(\mu\left(\frac{\partial u_i}{\partial x_j} + \frac{\partial u_j}{\partial i_i}\right) - \frac{2}{3}\mu\frac{\partial u_k}{\partial x_k}\delta_{ij}\right) - \frac{\partial p}{\partial x_i} + \rho g_i. \tag{2.48}$$

- Transport equations for species

$$\frac{\partial}{\partial t}(\rho Y_k) + \frac{\partial \rho u_j Y_k}{\partial x_j} = \frac{\partial}{\partial x_i}\left(\rho D \frac{\partial Y_k}{\partial x_j}\right) + \dot{\omega}_k \tag{2.49}$$

- Transport equations for enthalpy

$$\frac{\partial}{\partial t}(\rho h_s) + \frac{\partial}{\partial x_j}(\rho u_j h_s) = \frac{\partial}{\partial x_j}\left(\rho D \frac{\partial h_s}{\partial x_j}\right) + \dot{\omega}_T \quad \textit{with} \quad \rho D = D_{th} \tag{2.50}$$

- Diffusion coefficients

$$D = \frac{D_{th}}{\rho} = 2.58 \times 10^{-5} \times \left(\frac{T}{298K}\right)^{0.69} kgm^{-1}s^{-1} \tag{2.51}$$

- Dynamic viscosity

$$\mu = 1.67 \times c_{p_{mix}} \times 10^{-8} \times \left(\frac{T}{298K}\right)^{0.51} \quad kgs^{-1}m^{-1} \tag{2.52}$$

- State equation

$$\rho = \frac{pW}{RT} \tag{2.53}$$

2.3.2 Mixture averaged formulation, the summary

- Conservation of mass

$$\frac{\partial \rho}{\partial t} + \frac{\partial}{\partial x_j}(\rho u_j) = 0 \tag{2.54}$$

- Conservation of momentum

$$\frac{\partial}{\partial t}(\rho u_i) + \frac{\partial}{\partial x_j}(\rho u_i u_j) = \frac{\partial}{\partial x_j}\left(\mu\left(\frac{\partial u_i}{\partial x_j} + \frac{\partial u_j}{\partial i_i}\right) - \frac{2}{3}\mu\frac{\partial u_k}{\partial x_k}\delta_{ij}\right) - \frac{\partial p}{\partial x_i} + \rho g_i. \tag{2.55}$$

- Transport equations for species

$$\frac{\partial}{\partial t}(\rho Y_k) + \frac{\partial \rho u_j Y_k}{\partial x_j} = \frac{\partial}{\partial x_i}\left(\rho D_{km}\frac{W_k}{W}\frac{\partial X_k}{\partial x_j}\right) + \dot{\omega}_k \tag{2.56}$$

- Transport equations for enthalpy

$$\frac{\partial}{\partial t}(\rho h_s) + \frac{\partial}{\partial x_j}(\rho u_j h_s) = \frac{\partial}{\partial x_j}\left(\rho D\frac{\partial h_s}{\partial x_j}\right) - \frac{\partial}{\partial x_j}\left(\rho\sum_{k=1}^{N} Y_k h_{s,k} V_{k,j}\right) + \dot{\omega}_T. \tag{2.57}$$

- Binary diffusion coefficients

$$lnD_{jk} = A_{jk} + B_{jk}lnT + C_{jk}(lnT)^2 + D_{jk}(lnT)^3 \tag{2.58}$$

- Dynamic viscosity of pure species

$$ln\mu_k = A_{\mu,k} + B_{\mu,k}lnT + C_{\mu,k}(lnT)^2 + D_{\mu,k}(lnT)^3 \tag{2.59}$$

- Thermal conductivity of pure species

$$ln\lambda_k = A_{\lambda,k} + B_{\lambda,k}lnT + C_{\lambda,k}(lnT)^2 + D_{\lambda,k}(lnT)^3 \tag{2.60}$$

- Molecular diffusion coefficients

$$D_{km} = \frac{1 - Y_k}{\sum\limits_{j \neq k}^{N} X_j / D_{jk}} \tag{2.61}$$

- Dynamic viscosity of the mixture

$$\mu = \sum_{k=1}^{N} \frac{X_k \mu_k}{\sum\limits_{j=1}^{N} X_j \Phi_{kj}} \tag{2.62}$$

- Thermal conductivity of the mixture

$$\lambda = \frac{1}{2} \left(\sum_{k=1}^{N} X_k \lambda_k + \frac{1}{\sum\limits_{k=1}^{N} X_k / \lambda_k} \right) \tag{2.63}$$

- State equation

$$\rho = \frac{pW}{RT} \tag{2.64}$$

Chapter 3

Fundamentals of Chemical Kinetics and Combustion Theory

3.1 Models for Chemistry

The processes of chemical reaction in a reacting flow system may be described numerically at different complexity levels. In this section the different models for chemistry of a reacting flow is summarized in a table in the order of increasing complexity as it is suggested by Kee [64] .

Combustion Models		
Assumption	Properties	Approach
Fast Chemistry	Diffusion Controlled	Infinite Fast Chemistry
Da≫1	Chemical Equilibrium	
Finite Rate Chmistry	Kinetically Controlled	Analytically Reduced Mechanism
reaction reates are	Detail Mechanism	
calculated using	Global Reaction	
	molecular kinetics	

Table 3.1: Classification of assumptions in combustion simulation.

3.1.1 Fast Chemistry

In this type of modeling it is assumed that the rate of chemical conversion is diffusion or mixing controlled, not kinetically. Generally, a system can be called **kinetically controlled**, if the reaction is slow compared to the mixing. On the other hand, if slow mixing and fast chemistry results in a diffusion or mixing controlled system. To check the correctness of the fast chemistry assumption, one needs to estimate the *Damköhler* number which is a comparison of the chemical time scale and mixing or turbulent time scale.

$$Da = \frac{\tau_{mix}}{\tau_{chem}} , \tag{3.1}$$

where τ_{mix} and τ_{chem} denote the characteristic flow time or mixing time and the characteristic time for chemical reaction respectively. If this number has the value much larger than unity, the chemistry can be considered as fast chemistry and the process is mixing controlled. Small Damköhler number denotes a system in which kinetic is dominant.

3.1.1.1 Infinitely Fast Reaction

In this approach which is also well-known as "mixed is burned" model, the chemical time has a value significantly smaller than mixing time. This assumption makes it possible to simplify the problem in some cases to provide an analytically solution to the flame structure. Most authors classify this as an irreversible chemistry[64].

3.1.1.2 Chemical Equilibrium

In this approach fast chemistry is also assumed. Numerically, it is more complex than infinitely fast chemistry approach. The main difference between this assumption and the infinitely fast approach is the coexistence of the fuel and oxidizer. This leads to a more complex flame structure [101]. Since in this model the chemistry is assumed to be reversible, depending on the reaction type (endothermic or exothermic) and the temperature, the equilibrium could move toward reactants and products. The application is the same as infinitely fast chemistry but could have some shortcomings concerning the calculation of minor concentrations[64].

3.1.2 Finite Rate Chemistry

For this assumption the chemical time scales need too be bigger compared to those of mixing and the assumption of "mixed is burned" is not more valid. The chemical process is described on molecular level. The **Da** takes finite values and accordingly, more advanced models are required to account for finite chemistry.

3.1.2.1 Global Reactions

For this approach chemical process is assumed to be consisted of one global reaction. This global reaction can be interpreted as the final limit of a systematically reduced mechanism. For this global step, an Arrhenius rate is assigned for to calculate the rate of reaction. The shortcoming of this approach is that it is case limited and is valid only under some explicit conditions but not an unlimited wide range of temperatures and concentrations. It can not either be extrapolated to all different kinds of combustion regimes.

3.1.2.2 Detailed Reaction Mechanisms

The detailed reaction mechanism is at the moment numerically the most expensive and sophisticated approach for simulating combustion. It is simultaneously the most accurate, reliable and validated approach for the simulation of combustion systems. Similar to the global reaction, an Arrhenius rate is assigned not to describe a globally defined reaction but to each of reactions of a collection of elementary reactions. For each of these elementary reactions, the reactants, products and rate coefficients ($\boldsymbol{A}$, $\boldsymbol{\beta}$ and **activation energy**) are provided in a table. As stated earlier, the process is depicted on molecular level. Therefore the thermodynamic data, heat of formation, heat capacity of each of the species listed in the mechanism should be provided. Using detailed chemistry, one can calculate a source terms to input in the transport equation of the species. This means that a transport equation in the whole geometric domain has to be solved for each species.

3.1.2.3 Analytically Reduced Reaction Mechanisms

Simulating combustion using analytically reduced mechanism is a compromise between the accuracy and price to lower the simulation cost and keep the precision intact. It is cheaper than the detailed reaction mechanism but it retain the most important characters of the reaction process gotten from detailed mechanisms. There are different methods to systematically reduce a detailed mechanism including quasy steady state assumption [126], ILDM [83], partial equilibrium [126] and so forth.

3.2 Chemical Kinetics

As it is known in the combustion processes, chemical reaction rates control the rate of combustion. That's why understanding the elemental chemical processes is vital in the study of combustion e.g. ignition and flame extinction are strongly affiliated with the chemical processes.The study of the elementary reactions is called chemical kinetics which is a specialized field of physical chemistry. To be able to construct the computer model which can simulate the reacting systems, one needs the information of the detailed chemical path from reactants to products. In this chapter, first the basics of chemical kinetics are explained. Then, the chemical mechanism used in this work is described.

3.2.1 Global Versus Elementary Reactions

3.2.1.1 Global Reactions

It is not difficult to know that combustion is an exothermic conversion of a mixture including fuel and oxidizer into products. This conversion can be globally depicted by the global reaction (in case of a Hydrocarbon combustion) as:

$$C_nH_m + O_2 + N_2 \Longrightarrow CO_2 + H_2O + (C_xHy + CO + soot + NO_x + etc) \tag{3.2}$$

For example, for methane combustion in a global form one can write:

$$CH_4 + 2O_2 \Longrightarrow CO_2 + 2H_2O \tag{3.3}$$

Here the emissions are omitted and it is assumed that the combustion would be stoichiometric. According to experiments, fuel rate consumption can be given as:

$$\frac{d[X_{C_nH_m}]}{dt} = -k_g(T)[X_{C_nH_m}]^n[X_{O2}]^m, \tag{3.4}$$

here $[X_i]$ denotes the molar concentration of the ith species ($kmol/m^3$) in the mixture. The minus sign shows the consumption of fuel with time. The coefficient, k_g is called the

global rate coefficient which is generally not constant but strongly temperature dependent. The two exponents n and m are related to the reaction order. Equation 3.4 implies that this reaction has the mth order considering oxidizer and nth order considering fuel. m and n are gotten experimental data using curve fitting methods. In global reactions, they are not inevitably integer but, in elementary reactions they will only be integers and always constant.

Generally, at equlibrium state, the reverse direction is also possible, so that the equation can be written as:

$$A + B + C + D + \cdots \underset{[k_b]}{\overset{[k_f]}{\rightleftharpoons}} W + X + Y + Z + \cdots , \tag{3.5}$$

Here like before, A, B and C, denote the species and k_f, k_b are the forward and backward reaction coefficients. At equilibrium, on macroscopic level, one sided reaction toward more products or reactants can not be observed but on microscopic level, the reaction rates for both directions are equal to each other. As mentioned earlier, for the reaction rate of the species A, one can write:

$$\frac{d[A]}{dt} = -k_f(T)[A]^n[B]^m[C]^o[D]^p \ldots, \tag{3.6}$$

where n, m, o, ... are the reaction orders. At chemical equilibrium, it is also possible to write:

$$\frac{d[A]}{dt} = -k_b(T)[W]^r[X]^s[Y]^t[Z]^u \ldots \tag{3.7}$$

That means at equilibrium state one can write:

$$\frac{[W]^r[X]^s[Y]^t[Z]^u \ldots}{[A]^n[B]^m[C]^o[D]^p \ldots} = \frac{k_f}{k_b} \tag{3.8}$$

Hereby the ratio of the forward to the backward reaction rate is given by the equilibrium constant.

$$K_c = \frac{k_f}{k_b} \tag{3.9}$$

The equilibrium constant can be directly calculated from thermodynamic data of the reaction j of a mechanism as:

$$K_{cj} = exp(\frac{\Delta S_j^0}{R} - \frac{\Delta H_j^0}{RT})(\frac{p_{atm}}{RT})^{\sum\limits_{k=1}^{N} v_{kj}} \tag{3.10}$$

Using this equation, one can calculate the backward coefficient, if forward coefficient and equilibrium constant are known.

3.2.1.2 Elementary Reactions

Although using the global reaction approach is sufficient and applicable to solve some problems, one can not get detailed information of what exactly happens within the system during the combustion. As an example one can talk about methane combustion

$$CH_4 + 2O_2 \Longrightarrow CO_2 + 2H_2O \tag{3.11}$$

It is clear, to build CO_2 molecules requires C and O atoms which can together form the CO_2 afterward. To have C, means breaking all of the $C-H$ bonds in the CH_4 and to have O atoms requires breaking $O-O$ bonds in O_2 molecules. It may be not impossible but almost improbable that the molecules of one mole of methane collide with the molecules of 2 moles of oxygen and simultaneously all of the $O-O$ and $C-H$ bonds break and form carbon dioxide and water!.

In reality, a lot of sequential steps (reactions) can happen which involve intermediate species. To describe these intermediate reactions, one should write the elementary reactions. An Elementary reaction is a reaction on a molecular level and it appears exactly in the way written by reaction equation. Elementary reactions always have radicals as reactant or product. Radicals or free radicals are atoms or molecules that have unpaired electrons and are unstable. As mentioned, to cover an overall reaction, a lot of elementary reactions occur sequentially, to deliver the product. The collection of these reactions altogether is called **reaction mechanism** which may include a few steps or some hundreds of steps.

As already indicated, the reaction orders in elementary reactions are constant. They can be calculated without difficulty. Indeed, to determine the order of an elementary reaction, just the molecularity needs to be considered.

Bimolecular Reactions

Most of the elementary reactions in combustion are **Bimolecular** in which two molecules collide and react with each other to build the products. They can be presented as

$$A + B \Longrightarrow C + D, \tag{3.12}$$

for which the reaction rate is proportional to the concentration of the species A and B, i.e.

$$\frac{d[A]}{dt} = -k_{bi}[A][B]. \tag{3.13}$$

Bimolecular reactions have overal second order.

Unimolecular Reactions

In the case of isomerization or decomposition of one species to form the products, the reaction is called **Unimolecular**. They are first order and contain the most typical reactions considerable to combustion like dissociation of oxygen or hydrogen.

$$A \Longrightarrow B + C, \tag{3.14}$$

For this type of reaction, the rate at which it proceeds can be determined as

$$\frac{d[A]}{dt} = -k_{uni}[A]\,. \tag{3.15}$$

Trimolecular Reactions

Trimolecular or **Termolecular** reactions can be usually considered as recombination reactions and are third order.

$$A + B + M \Longrightarrow C + M\,. \tag{3.16}$$

The reaction rate for Trimolecular reactions can be calculated as:

$$\frac{d[A]}{dt} = -k_{tri}[A][B][M]\,. \tag{3.17}$$

M in this kind of reactions refers to the **third body**. The third body is needed to take away the released energy produced by radical-radical reactions to form stabilized species.

3.2.1.3 Compact Notation

Generally, it is common to have a compact notation to be able to represent both the individual species and the mechanism. For a mechanism with M reactions and N species to involve elementary steps and all of the species one can write

$$\sum_{j=1}^{N} v^{'}_{ji} X_j \leftrightarrows \sum_{j=1}^{N} v^{''}_{ji} X_j \qquad \text{for} \qquad i = 1, \ldots M\,, \tag{3.18}$$

where $v^{'}$, $v^{''}$ are the **stoichiometric coefficient** of the reactants and products side of the equation, respectively for kth species in the jth reaction. Considering this, one can easily express compact notation for reaction rate of each species in a multi-step mechanism as:

$$\dot{\omega}_j = \sum_{i=1}^{M} v_{ji} q_i \qquad \text{for} \qquad j = 1, \ldots, N\,, \tag{3.19}$$

$$v_{ji} = v^{''}_{ji} - v^{'}_{ji}\,, \tag{3.20}$$

$$q_i = k_f \prod_{j=1}^{N} [X_j]^{v^{'}_{ji}} - k_b \prod_{j=1}^{N} [X_j]^{v^{''}_{ji}}\,. \tag{3.21}$$

Here q_i is the **the rate of progress variable** for the ith elementary reaction and $[X_j]$ represents the molar concentration of the species involved in the reaction. The functional dependency of the reaction rate on temperature is generally given by reaction rate coefficient, k_f. Both reaction rate coefficients k_f and k_b are generally strongly temperature dependent. This temperature dependency can be according to Arrhenius(1889) [4], depicted by a simple formula (Arrhenius law),

$$k_f = A^{'} exp(-\frac{E^{'}_a}{RT})\,, \tag{3.22}$$

or in the modified way of the Arrhenius law

$$k_{f_j} = A_j T^{\beta_j} exp(-\frac{E^{'}_a j}{RT})\,. \tag{3.23}$$

A_j, β_j and E_j are the pre-exponential factor, the temperature exponent and the activation energy respectively. **The activation energy** is the energy needed to start the reaction which can have depending on the type of the reaction, values from zero to the bond energies of the molecule. As an example, in dissociation reaction of CH4, the activation energy is approximately equal to the bond energy of the first $C-H$ bond.

3.2.2 Chain Reactions

Chain reactions are a series of reactions involving radical and intermediate species that react and produce some other radicals. This radicals, in turn, react to generate other intermediates or radicals subsequently. This happens sequentially like a chain of reactions and continues until the chain reaches some reactions involving stable species which are the result of colliding two radicals. After the mechanism reaches this stable products the chain breaks. The intermediates produced during chain reaction are called *chain carriers*. Each chain reaction includes several types of steps or in other words different kinds of reactions:

3.2.2.1 The Chain Initiation Step

The initiation phase describes the step that initially creates a highly reactive intermediate. In most cases, this step does not happen automatically because of high energy barriers involved and the stability of the reactants and the oxidators. Indeed, molecules which get high activation energy (initiation heat) have vigorous intermolecular collisions which cause to free chain carriers from stable reactants. For example, in methane-air combustion, the initiation step involves abstraction of a hydrogen atom from molecular methane.

3.2.2.2 The Chain Propagation Steps

This step describes the chain part of these kind of reactions. The chain carriers are produced in the previous step. Once they (highly reactive intermediate) exist they can react with still existing stable molecules to form new free radicals. These new free radicals continue the chain and help to generate yet more free radicals, and so on. One of the important properties of chain propagating steps is that the number of the chain carriers before and after each reaction does not change.

3.2.2.3 The Chain Branching Steps

A branching step in a chain reaction is defined as one that increases the number of activated intermediates, as opposed to a propagating step, which keeps the number the same. In these reactions, the unstable chain carriers react with other species (does not necessarily need to be stable species) and form more unstable highly reactive intermediates.

3.2.2.4 The Chain Termination Step

The chain termination step is a step where two or more carriers react with each other to form a stable, non-radical educt. It can be easily understood that in these types of reactions, the number of free radicals decreases and there is at least one stable species in the product side of the reaction.

3.2.3 Mechanism

As stated above, to cover a global reaction, a lot of elementary reactions occur sequentially to deliver the product. The collection of these reactions altogether is called **reaction mechanism** which may include a few steps or some hundreds of steps. Each mechanism consists of a chain initiation step, at least one(could be more) propagating step, could have some branching steps and definitely at least one termination step.

In the mechanisms, generally, the reactions are listed in a column showing the reactants and products of each reaction. For each reaction, the following three constants, $\boldsymbol{A}$, $\boldsymbol{\beta}$ and $\boldsymbol{E_a}$ are provided in which $\boldsymbol{A}$ is a exponential factor, $\boldsymbol{\beta}$ is a unitless number of order 1 and $\boldsymbol{E_a}$ is the activation energy in the Arrhenius law. Depending on application, there are different combustion mechanisms. As an example, the huge n-hexane mechanism suggested by Glaude et al. can be mentioned [44]. This mechanism consists of 3662 reactions and includes 470 chemical species.

In this work, the simulations are mainly performed for the methane-air mixture for which a lot of mechanisms can can be found. As an example for this mixture, Smooke mechanism [88] can be mentioned. This mechanism consists of 25 reactions and 16 species and considers only the $C1$ path. GRI-Mech 3.0 [110] is another mechanism developed for methane-air combustion consisting of 325 elementary reactions between 53 species involved.

Results of the simulations performed by van Oijen [120] showed that the popular Smooke mechanism [88] can very well capture the structure of the flame in great details and quantitatively express the global flame characteristics such as burning velocity, and adiabatic flame temperature for lean to rich methane-air mixtures. Since in this work the code is verified through comparison with his results, it is decided to perform the simulations using this mechanism.

In table 3.2 the Smooke mechanism can be found. The reaction with the highest activation energy is always start reaction. Providing this amount of energy helps to separate a H-atom from CH_4-molecules. After this step, the resulting CH_3-radicals react through reaction 13 mainly with O-atoms to give formaldehyde(CH_2O). The next step will be forming HCO-radicals after abstraction of two H-atoms from CH_2O- reactions 14 and 15 while it is reacting with H and OH. The HCO-radicals decompose either through reacting with H-radicals which means through reaction 16 or through collisions with a second body (H_2O, CH_4, CO_2, ...) through reaction 17 yielding CO and H.

The process of the Alkyl(CH_3) formations of composition at this time occurs in the induction zone. The peak of profile of the reaction rate of the CH_3 is always around 0.1 flame thickness away from the peak of the fuel decomposition rate (CH_4) . This is the characteristic reaction path for the combustion of methane, which dictates the flame structure [125]. This pattern is preserved throughout the whole quenching process but with minor differences.

3.3 Combustion theory

3.3.1 Combustion modes

Generally, based on the way the reactable mixture for combustion is provided, different types of flames can be distinguished. They are classified as premixed flames and diffusion flames which are here introduced briefly, but before we begin, some parameters through which the flames can be characterized should be discussed here.

Reaction no.	**Reaction**	**A**	β	E_a
1	H+O2=OH+O	2.00E+14	0.000	16800.
2	O+H2=OH+H	1.80E+10	1.000	8826.
3	OH+H2=H2O+H	1.17E+09	1.300	3626.
4	OH+OH=O+H2O	6.00E+08	1.300	0.
5	H+O2+M=HO2+M	2.30E+18	-0.800	0.
	H2O/6.5/ CO2/1.5/ CO/0.75/	N2/0.4/	O2/0.4/	
6	H+HO2=2OH	1.50E+14	0.000	1900.
7	H+HO2=H2+O2	2.50E+13	0.000	700.
8	OH+HO2=H2O+O2	2.00E+13	0.000	1000.
9	CO+OH=CO2+H	1.51E+07	1.300	-758.
10	CH4=CH3+H	2.30E+38	-7.000	114363.
11	CH4+H=CH3+H2	2.20E+04	3.000	8750.
12	CH4+OH=CH3+H2O	1.60E+06	2.100	2460.
13	CH3+O=CH2O+H	6.80E+13	0.000	0.
14	CH2O+H=HCO+H2	2.50E+14	0.000	10500.
15	CH2O+OH=HCO+H2O	3.00E+13	0.000	167.
16	HCO+H=CO+H2	4.00E+13	0.000	0.
17	HCO+M=H+CO+M	1.60E+14	0.000	14700.
18	CH3+O2=CH3O+O	7.00E+12	0.000	25652.
19	CH3O+H=CH2O+H2	2.00E+13	0.000	0.
20	CH3O+M=CH2O+H+M	2.40E+13	0.000	28812.
21	HO2+HO2=H2O2+O2	2.00E+12	0.000	0.
22	H2O2+M=OH+OH+M	1.30E+17	0.000	45500.
23	H2O2+OH=H2O+HO2	1.00E+13	0.000	1800.
24	H+OH+M=H2O+M	2.20E+22	-2.000	0.
	H2O/6.5/ CO2/1.5/ CO/0.75/	N2/0.4/	O2/0.4/	
25	H+H+M=H2+M	1.80E+18	-1.000	0.
	H2O/6.5/CO2/1.5/	CO/0.75/	N2/0.4/	O2/0.4/

Table 3.2: Smooke combustion mechanism for CH_4

EQUIVALENCE RATIO

Assume reacting the fuel and oxidizer can be described through the following global reaction:

$$\acute{\nu}_F F + \acute{\nu}_O O \longrightarrow Products. \tag{3.24}$$

The ratio,

$$\left(\frac{Y_O}{Y_F}\right) = \frac{\acute{\nu}_O W_O}{\acute{\nu}_F W_F} = s \tag{3.25}$$

is called mass stoichiometric ratio. The equivalence ratio ϕ, of a reaction is the product of the mass stoichiometric ratio and the fraction of fuel to air mass fractions i.e.

$$\phi = s\frac{Y_F}{Y_O} = s\frac{m_F}{m_O} = \left(\frac{Y_F}{Y_O}\right) / \left(\frac{Y_F}{Y_O}\right)_{st}. \tag{3.26}$$

Equivalence ratio provides information in which relation fuel and oxidizer are mixed with each other and how far is the mixture from the stoichiometric condition.Having this parameter, one can characterize the combustion regime. Depending on ϕ, the premixed flames can be categorized as follows

- lean combustion, if $\phi < 1$ more air than needed to be completely consumed
- rich combustion, if $\phi > 1$ more fuel than needed to be completely burned
- stoichiometric combustion, if $\phi = 1$ exact amount of needed fuel and oxidizer to perfectly burn the mixture

This parameter is one of the most important parameters in illustrating the premixed flames. Knowing equivalence ratio, one can predict a lot of behaviors of the flame. The disadvantage of equivalence ratio is that it can be retraced until the reaction zone. Alternatively one can define another parameter called as:

ELEMENT MIXTURE FRACTION

If continuity equation is satisfied, no mass can be produced or disappear. Although one species can convert to another species through reaction process, the amount of each element through the whole domain from unburnt cold reactants to the products remains constant no matter what happens during the reaction. Hence, the element mixture fraction can be defined for example as

$$f = Y_C + Y_H. \tag{3.27}$$

ADIABATIC FLAME TEMPERATURE

In a closed system with constant pressure for a specific mixture, adiabatic flame temperature can be defined as the temperature of the flame after the complete combustion, under isobaric and adiabatic condition. This temperature is a function of equivalence ratio, inlet temperature and the pressure p of the system. For more information see [132], [90], [43], [32] , [97].

3.3.1.1 Diffusion flames

The first type of the flames which were once the most common type of the flames in the industry, are the so called diffusion flames, or in other words, non-premixed flames. In this type of flame the fuel and oxidizer are separately provided to the combustion chamber/flame zone and are not mixed in advance, but they are mixed while they burn. Best example of these type of flames are candles. Nowadays, diffusion flames are also applied as pilot flames to stabilize the premixed flames in the combustion chamber of the stationary gas turbines.

In figure 3.1a the simplified structure of a non-premixed methane-air flame is demonstrated. As it can be observed, the fuel is provided from one side and the oxidizer is supplied from another side of the flame. In Figure 3.1c the profiles of temperature , some important species , source term of the energy equation/heat release rate as well as the mixture fraction profile of a diffusion flamelet are shown. As it can be seen, the reaction occurs just in a thin part of the domain where fuel and oxidizer reach each other. This zone is called **reaction zone**. In this zone the ideal mixing for reaction is provided so that one can say there is a contour at which the reaction happens in stoichiometric condition. Right and left to this line, the mixture is either very rich and far from the stoichiometry or very lean. In these zones, as it can easily be interpreted, nothing can react due to overstepping the flammability limits of the mixture or shortage either of fuel or oxidizer. For more information about diffusion flames please see [126], [98], [14]and [76].

3.3.1.2 Premixed flames

Unlike the diffusion flames, in the premixed flames, the fuel and oxidizer are mixed before entering the chamber. Figure 3.1b demonstrates a simplified sketch of premixed flame. As it is mentioned, in the premixed flames, the reactants enter the burner. In an ideal mixing process, the mixing should be in molecular level. Whether the mixture is flammable is determined by equivalence ratio. If $\phi << 1$, which means the mixture is too lean or if $\phi >> 1$, too rich, the mixture is not within it's flammable limits. These limits are unique for specific mixture and can be measured. For more information see [127], [51].

In figure 3.1d the profiles of the temperature, important species and the heat release rate of a 1-dimensional stoichiometric methane-air flamelet are depicted. In these profiles 3 zones are to be distinguished. In the first zone, the cold premixed reactants enter the domain with the inlet temperature. They approach the flame area with the convective velocity of the flow. In the vicinity of the flame the temperature gradually rises. This increase provides the activation energy needed specially for the chain initiation step of the mechanism (please see reaction no. 10 in the mechanism). This zone is called preheating zone.

The second zone, the so called reaction zone is where the reaction happens. The system got enough energy to sustain go through the chain propagation and chain branching steps. The intermediates/chain carriers are provided in this zone. In the last zone, the radicals are consumed and the products reach their equilibrium level. In some literature [118], the second and third zones together are called the reaction zone and just two zones are identified. There are some parameters which are of considerable importance in investigating the premixed flames and are briefly introduced here:

LAMINAR BURNING VELOCITY

The flame speed or the so called laminar burning velocity, s_l, is the component of the velocity at which the un-stretched unburnt flammable gas mixture consumed normal to the flame front. Here it should be considered that s_l alone, does not provide any information about the propagating direction of the flame front. Comparing this velocity to the convective velocity of the flow, the flame front propagates toward the products, if the convective velocity is lower than s_l, toward the unburnt mixture, if s_l is higher than convective velocity. It has no movement if these two velocities are equal. In this case, we have a stabilized laminar flame.

Burning velocity is an eigenvalue of the reacting system. This means, for a given mixture composition, having p as pressure, T_u as unburnt temperature, the burning velocity has a unique value. It decreases if the pressure increases and the unburnt temperature and mixture composition remain unchanged and increases if unburnt temperature increases and pressure and mixture composition are not changed [126].

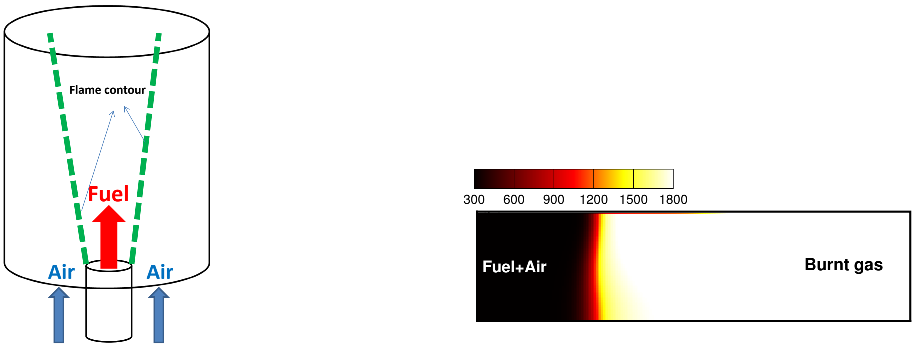

(a) Simplified sketch of a diffusion flame configuration

(b) Simplified sketch of premixed flame configuration

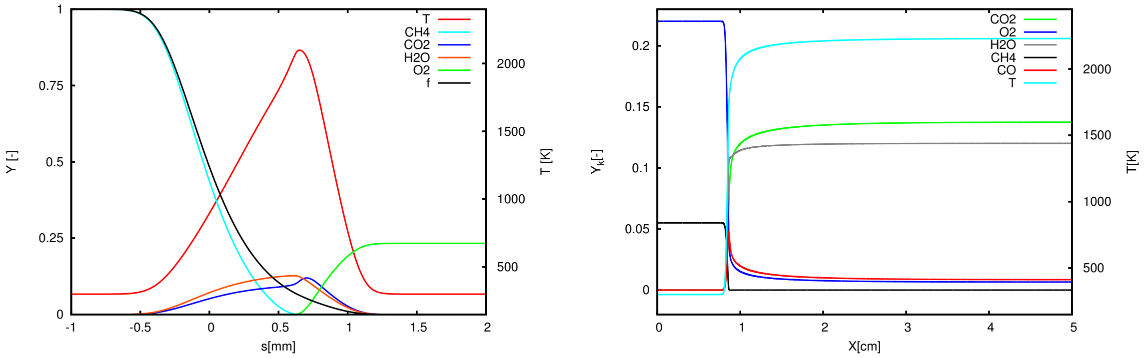

(c) Example of the mass fraction profiles of the main species in a diffusion flamelet

(d) Example of the mass fraction profiles of the main species in premixed flamelet

Figure 3.1: Simplified configurations and flame profiles in diffusion and in premixed flames

There are different ways to calculate the laminar flame speed of which two formulas are introduced [73]. The first method is to obtain the burning velocity through conservation of mass. Writing the continuity equation, s_l can be derived as

$$s_l = \frac{u_b - u_u}{\dfrac{\rho_b}{\rho_u} - 1}\,, \tag{3.28}$$

where the indices b and u represent the burnt or unburnt sides of the flame front respectively and u and ρ are responsible for velocity of the flow and density. Another way to determine the burning velocity is to subtract the absolute flame speed from the convective velocity in the unburnt side of the flame front as follows

$$s_l = u_u - s_a = u_u - \frac{x_F(t_2) - x_F(t_1)}{t_2 - t_1}\,, \tag{3.29}$$

where x_F represents the spatial position of the flame front at time t_1 and t_2.

FLAME THICKNESS

Laminar flame thickness is of considerable interest specially in investigating flame-wall interactions. Like burning velocity there are different ways to define flame thickness. The roughly estimated definition of the flame thickness for simple chemistry is

$$\delta_f = \frac{\lambda_u}{\rho_u c_{p_u} s_l} \,. \tag{3.30}$$

This definition is also called diffusive thickness, knowing the definition of the thermal diffusion coefficient, one can easily derive that

$$\delta_f = \frac{D_{th}}{s_l} \,. \tag{3.31}$$

Some other authors [49] prefer to define flame thickness as follows

$$\delta_f^\circ = \frac{T_2 - T_1}{max\left(\left|\frac{\partial T}{\partial x}\right|\right)} \tag{3.32}$$

which may be more appropriate and precise to define the mesh size in numerical simulations [101].

Chapter 4

Numerical Methods

In the last two chapters, the essential equations needed to simulate the reacting system of a gas mixture are introduced. The mechanism which describes the procedure of the reaction and the method to calculate the source terms from the mechanism are explained. Some vital definitions and models needed to define, perform,verify and post-process the simulations are presented. In this chapter, the way this equation system is solved will be provided. Generally, there is no analytic solution for a non-linear coupled partially differential equation system like the one expressed in the chapter 2 except for extremely special simplified cases. One way to overcome this problem is to solve this equation numerically. To do this, having the system, an appropriate coordinate system is defined. In this coordinate system, the domain is discretized. Using these two, a proper numerical grid is sketched. Over these discretized domain, the non-linear differential equation system is converted to a linear algebraic system over these numerical cells using the so called finite-volume method. This approach is used to integrate the partial differential equation and convert them to linear algebraic equation within each defined cell of the discretized domain. For the discretization either structured (hexahedral discretizing method) or unstructured (tetrahedral discretizing method) is used.

FASTEST-3D is used to perform the simulations in this work. Fastest is abbreviated form of "Flow Analysis Solving Transport Equation System Turbulence 3-Dimensional". Fastest is an open source, academic 3D Navier-Stokes solver written to perform simulations of hydrodynamic-incompressible flows- problems using RANS. It has been first developed by Durst and Schäfer [30] at Chair of Fluid Mechanics, University of Erlangen, Germany. Later Fastest has been used and developed by different research groups which led to diverge from the original code and development of variety of new versions. This code has been used and extenden in the chair of Energy and Power Plant Technology to be able to perform large eddy simulations for reacting flows in continuous/disperse phases using explicit/implicit temporal discretization method.

In this chapter, it will be explained how in Fastest, the Navier-Stokes and skalars transport equations are temporally and spatially discretized based on finite volume method. Afterward, it will be explained, on which coordinate and the vector system, the discretization is performed. The boundary conditions which are implemented in the code will be extensively described.

4.1 Finite volume method

The main idea of finite volume method is to discretize the whole domain to a finite number of smaller control volume (CV) of finite size, so that in each volume the non-linear equations can be approximated as linear algebraic equations. This is performed in Fastest using non-orthogonal hexahedral block structured mesh. Using parallelisation method, for the more complicated geometries, one has the opportunity to use the domain decomposition method. This means to divide the geometry to more hexahedron blocks but in simpler shapes, each of which consists of some control volumes. The blocks can also be fitted to the boundaries. This option is helpful to mesh the curvy sides of the geometry. They are also covered by a layer of cells. These cells are the so called dummy cells. These layers of the cells in each of the six sides of the block are in accompaniment with the first row of the cells in the neighbor block. That is used for the data exchange between the neighbor blocks during parallelisation process.

In figure 4.1 a simplified sketch of a hexahedral control volume in a cartesian (X,Y,Z) coordinate system can be seen. All of the variables are saved in the center of each CV(Same point). This is called collocated grid arrangement suggested by Rhie & Chow (1983) [105]. In this figure the capital letters represent the cell centers. P defines the control volume center and E, W, N, S serve as the centers of eastern, western, northern and southern neighbor cells respectively. T, B are corresponding to top and bottom. The lowercase letters, e, w, n, s, t, b indicate the same outlined direction each of which on the corresponding surface of the control volume knowing the hexahedral control volumes have six plane surfaces. As you can see, defining the domain in this way, to each control volume a computational node can be assigned. This node is positioned in the center of the control volume. Considering the mid-point rule, the value of each variable in the center of the control volume represents the mean over the control volume.

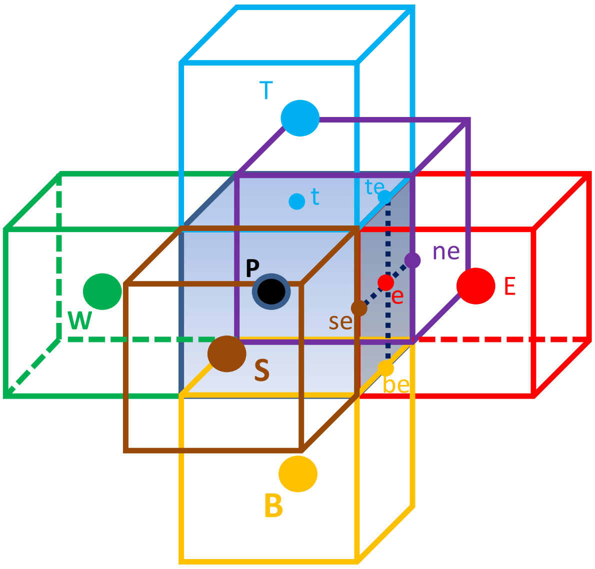

Figure 4.1: Simplified sketch of a hexahedral control volume.

4.1.1 Discretization of the generic form of transport equation

Assume ψ is an arbitrary conserved transport variable (can be velocity, density, enthalpy, mass fraction, etc.). Writing transport equation for ψ in the conserved form yields:

$$\frac{\partial}{\partial t}(\rho\psi) + \frac{\partial}{\partial x_j}(\rho u_j \psi) = \frac{\partial}{\partial x_j}\left(\Gamma_\psi \frac{\partial \psi}{\partial x_j}\right) + \dot{\omega}_\psi, \tag{4.1}$$

where Γ_ψ and $\dot{\omega}_\psi$ represent the diffusion coefficient of the conserved variable, ψ and its source term correspondingly. Integrating this equation over the previously shown control volume delivers

$$\int_V \frac{\partial}{\partial t}(\rho\psi) dV + \int_V \frac{\partial}{\partial x_j}(\rho u_j \psi) dV = \int_V \frac{\partial}{\partial x_j}\left(\Gamma_\psi \frac{\partial \psi}{\partial x_j}\right) dV + \int_V \dot{\omega}_\psi dV, \tag{4.2}$$

herein V is the volume of the represented control volume. Converting volume integrals to surface integrals using Gaussian divergence theorem

$$\int_V \frac{\partial}{\partial t}(\rho\psi)\, dV + \int_S \rho u_j \psi n_j \, dS = \int_S \left(\Gamma_\psi \frac{\partial \psi}{\partial x_j}\right) n_j \, dS + \int_V \dot{\omega}_\psi \, dV \tag{4.3}$$

having divergence theorem as

$$\int\int\int_V (\nabla.\psi)\, dV = \int\int_{SV} (\psi.n)\, dS\,, \tag{4.4}$$

where n denotes the normal vector toward the outside of the control volume. This means, in variable field, if ψ is a continuous and differentiable vector over the nominated control volume, the volume integral of the divergence of ψ over V is equal to the *sum* of the fluxes of ψ through all of the surfaces of the control volume. This helps to convert the volume integrals to surface integrals and obtain algebraic equations for particular CV. Knowing this, the equation 4.3 can be rewritten as

$$\underbrace{\int_V \frac{\partial}{\partial t}(\rho\psi) dV}_{TT} + \sum_k \underbrace{\int_{S_k} \rho u_j \psi n_j dS_k}_{F_k^C T} + \sum_k \underbrace{\int_{S_k} \left(\Gamma_\psi \frac{\partial \psi}{\partial x_j}\right) n_j dS_k}_{F_k^D T} + \underbrace{\int_V \dot{\omega}_\psi dV}_{QT}, \tag{4.5}$$

where TT, $F_k^C T$, $F_k^D T$ and QT denote the transient term, convective flux through the control volume, diffusive flux through the control volume and eventually the source term of the conservative variable, ψ correspondingly and k denotes the surfaces constituting the correspondent cell. To get algebraic equation from the above stated mathematical relation, the integral terms should be approximated.

4.1.2 Approximation of the integral terms

Having equation 4.5 in the current form, one can approximate the different terms and convert it to algebraic equation.

TRANSIENT TERM

The transient term can be approximated by replacing the value of the product of the integral variable in the cell center, which is the mean value of the cell and the volume of the correspondent cell. Using this yields

$$TT = \int_V \frac{\partial}{\partial t}(\rho\psi)dV \approx \left(\frac{\partial}{\partial t}\rho\psi\right)_P \delta V, \tag{4.6}$$

where the δV represents the volume of the area to be integrated.

THE SOURCE TERM

Source term Q can also simply be approximated following the same rule like transient term. Thus,

$$QT = \int_V \dot{\omega}_\psi dV \approx \left(\dot{\omega}_\psi\right)_P \delta V. \tag{4.7}$$

THE SURFACE INTEGRALS

Expanding the surface integral terms of the equation 4.5, also needs using the midpoint rule (MPR). Here the midpoint is defined as the value of the integrand at the center of control volume's surface. As an example of a general case consider ψ as integrand. The surface integration of this integrand is the sum of the integrals on each surface of the control volume each of which can be approximated as

$$\psi_k = \int_{S_k} \psi dS \approx \overline{\psi_k}\delta S_k \tag{4.8}$$

where k can be each of the surfaces forming the control volume. In the case of the hexahedral meshing, k can be the west, east, north, south, top and bottom surface. Following this example for the diffusive term on the east surface yields

$$F_e^D T = \int_{S_e} \left(\Gamma_\psi \frac{\partial \psi}{\partial x_j}\right) n_j dS \approx \left(\Gamma_\psi \frac{\partial \psi}{\partial x_j}\right)_e n_j \delta S_e. \tag{4.9}$$

The same can be done for the convective flux term on the east surface of the cell

$$F_e^C T = \int_{S_e} \rho u_j \psi n_j dS_e \approx \left(\rho u_j \psi n_j\right)_e \delta S_e. \tag{4.10}$$

Substituting the last four equations for the correspondent terms in the equation 4.5 gives

$$\left(\frac{\partial}{\partial t}\rho\psi\right)_P \delta V + \sum_k \left(\rho u_j \psi n_j\right)_k \delta S_k + \sum_k \left(\Gamma_\psi \frac{\partial \psi}{\partial x_j}\right)_k n_j \delta S_k + \left(\dot{\omega}_\psi\right)_P \delta V. \tag{4.11}$$

4.2 Coordinate transformation

Since we have non-orthogonal grid system, one can consider a local coordinate system in each cell center and on each cell face and then transform the derivatives from this system to a global coordinate system. Consider a global cartesian coordinating system denoted with (x_1, x_2, x_3) and a local coordinating system represented with $(\zeta_1, \zeta_2, \zeta_3)$ defined for each cell. The unit vectors on each coordinate are defined connecting the central point of each cell face to the central point of the same control volume. As we know from the mathematics, to transform the derivatives with respect to the local coordinating system to a global system, one needs to perform the following operation

$$\frac{\partial \psi}{\partial x_j} = \frac{\beta_{ji}}{J} \frac{\partial \psi}{\partial \zeta_i}, \tag{4.12}$$

where β_{ji} are the elements of the transpose adjoint matrix of the inverse transformation (global to local) given by

$$\beta_{ji} = \begin{bmatrix} \frac{\partial x_2}{\partial \zeta_2}\frac{\partial x_3}{\partial \zeta_3} - \frac{\partial x_2}{\zeta_3}\frac{\partial x_3}{\partial \zeta_2} & \frac{\partial x_1}{\partial \zeta_3}\frac{\partial x_3}{\partial \zeta_2} - \frac{\partial x_1}{\partial \zeta_2}\frac{\partial x_3}{\partial \zeta_3} & \frac{\partial x_1}{\partial \zeta_2}\frac{\partial x_2}{\partial \zeta_3} - \frac{\partial x_1}{\partial \zeta_3}\frac{\partial x_2}{\partial \zeta_2} \\ \frac{\partial x_2}{\partial \zeta_3}\frac{\partial x_3}{\partial \zeta_1} - \frac{\partial x_2}{\partial \zeta_1}\frac{\partial x_3}{\partial \zeta_3} & \frac{\partial x_1}{\partial \zeta_1}\frac{\partial x_3}{\partial \zeta_3} - \frac{\partial x_1}{\partial \zeta_3}\frac{\partial x_3}{\partial \zeta_1} & \frac{\partial x_1}{\partial \zeta_3}\frac{\partial x_2}{\partial \zeta_1} - \frac{\partial x_1}{\partial \zeta_1}\frac{\partial x_2}{\partial \zeta_3} \\ \frac{\partial x_2}{\partial \zeta_1}\frac{\partial x_3}{\partial \zeta_2} - \frac{\partial x_2}{\partial \zeta_2}\frac{\partial x_3}{\partial \zeta_1} & \frac{\partial x_1}{\partial \zeta_2}\frac{\partial x_3}{\partial \zeta_1} - \frac{\partial x_1}{\partial \zeta_1}\frac{\partial x_3}{\partial \zeta_2} & \frac{\partial x_1}{\partial \zeta_1}\frac{\partial x_2}{\partial_{\zeta_2}} - \frac{\partial x_1}{\partial \zeta_2}\frac{\partial x_1}{\partial \zeta_2} \end{bmatrix}, \tag{4.13}$$

and J represents for Jacobian of the matrix $\mathbf{A}$ given by

$$J = det\mathbf{A} \tag{4.14}$$

where $\mathbf{A}$ can be expanded as follows

$$\mathbf{A} = \begin{bmatrix} \frac{\partial x_1}{\partial \zeta_1} & \frac{\partial x_1}{\partial \zeta_2} & \frac{\partial x_1}{\partial \zeta_3} \\ \frac{\partial x_2}{\partial \zeta_1} & \frac{\partial x_2}{\partial \zeta_2} & \frac{\partial x_2}{\partial \zeta_3} \\ \frac{\partial x_3}{\partial \zeta_1} & \frac{\partial x_3}{\partial \zeta_2} & \frac{\partial x_3}{\partial \zeta_3} \end{bmatrix}. \tag{4.15}$$

Having β_{ji} and $det\mathbf{A}$ one can rewrite the transport equation 4.5 using local coordinating system as

$$\int_V \frac{\partial}{\partial t}(\rho\psi)dV + \int_S \rho u_j \psi n_j dS = \int_S \left(\frac{\Gamma_\psi}{J}\frac{\partial \psi}{\partial \zeta_j}\beta_{ji}\right) n_j dS + \int_V \dot{\omega}_\psi dV. \tag{4.16}$$

. Applying the approximation used in equation 4.11 yields

$$\left(\frac{\partial}{\partial t}\rho\psi\right)_P \delta V + \sum_k \left(\rho u_j \psi n_j\right)_k \delta S_k + \sum_k \left(\frac{\Gamma_\psi}{J}\frac{\partial \psi}{\partial \zeta_j}\beta_{ji}\right)_k n_j \delta S_k + \left(\dot{\omega}_\psi\right)_P \delta V. \tag{4.17}$$

For more information about coordinate transformation see [71], [72].

4.3 Approximation for the value at CV-Face

4.3.1 Second order interpolation

To approximate the convective and diffusive terms requires the knowledge of the value of variable and it's gradient at the control volume's surface center. The easiest way to do this will be distance weighting interpolation between the value of the CV-center and that of the neighbor cell assuming the velocity field, Γ and density are known everywhere in the domain. Linear interpolation is second order accurate, if the cell surface angles are right angles. In this case, to calculate the value at e.g. the eastern surface of the control volume we have

$$\psi_e = \psi_E \gamma_e + \psi_P (1 - \gamma_e) \tag{4.18}$$

where γ_e is defined as

$$\gamma_e = \frac{x_e - x_P}{x_E - x_P} \tag{4.19}$$

If the angles are not 90°, which is very common in more complicated geometry, it won't deliver second order of accuracy any more. To interpolate in this situation and keep the accuracy the same, Lehnhäuser and Schäfer [77] suggested a new interpolation method. In their method to interpolate between the cell center P and correspondent neighbor center E, additional neighbor nodes N, S, T, B also participate in the interpolation. The method is based on 6 points and as it can be seen is a three dimensional interpolating. Performing this for the eastern surface results in

$$\psi_e = \gamma_E \psi_E + (1 - \gamma_E)\psi_P + \gamma_{NS}(\psi_N - \psi_S) + \gamma_{TB}(\psi_T - \psi_B), \tag{4.20}$$

where γ_E, γ_{NS} and γ_{TB} are the interpolation factors calculated as

$$\gamma_E = \frac{x_{i,P} - x_{i,e}}{\mathfrak{J}_e} \phi_e^{1i}, \tag{4.21}$$

$$\gamma_{NS} = \frac{x_{i,P} - x_{i,e}}{\mathfrak{J}_e} \phi_e^{2i}, \tag{4.22}$$

$$\gamma_{TB} = \frac{x_{i,P} - x_{i,e}}{\mathfrak{J}_e} \phi_e^{3i}. \tag{4.23}$$

ϕ_e^{1i}, ϕ_e^{2i}, ϕ_e^{3i}, and $\mathfrak{J}_e$ are calculated using

$$\phi_e^{1i} = \epsilon_{ikl} \big[\big(x_{k,N} - x_{k,S}\big) \big(x_{l,T} - x_{l,B}\big) \big] \tag{4.24}$$

$$\phi_e^{2i} = \epsilon_{ikl} \big[\big(x_{k,T} - x_{k,B}\big) \big(x_{l,E} - x_{l,P}\big) \big] \tag{4.25}$$

$$\phi_e^{3i} = \epsilon_{ikl} \big[\big(x_{k,E} - x_{k,P}\big) \big(x_{l,N} - x_{l,S}\big) \big] \tag{4.26}$$

$$\mathfrak{J}_e = \big(x_{i,E} - x_{i,P}\big) \phi_e^{1i}. \tag{4.27}$$

Using this method for the right angles led to the same results of normal linear interpolation. For more information see [77].

4.3.2 TVD interpolation

Albeit the normal linear interpolation(CDS) for convective fluxes is second order accurate, it potentially could cause instabilities like oscillations. Approximating the value at the CV-surface by the value of the node upstream of it, which is called *upwind interpolation*, is another way to approximate. Although it is more stable and never causes oscillation, it is famous for being numerically dissipative. There are other ways to interpolate fluxes at the cell faces having higher order of accuracy for example taking one more upstream side point to set parabola to get third order of accuracy, QUICK or using even more point to get forth order accuracy.

Another way to have the advantage of these methods is to combine lower order interpolation methods with the higher order methods to have a damping function, same stability and simultaneously more accurate than upwind interpolation. The *TVD-limiter* (Total variation diminishing) suggested by Zhou et al. [135] is based on this idea and implemented in our in-house code Fastest which will be briefly explained here. To determine ψ_e, the value of the variable ψ on the eastern face of the control volume using TVD-limiter yields:

$$\psi_e = \psi_U + \frac{|x_{i,e} - x_{i,U}|}{|x_{i,D} - x_{i,U}|} B(r)(\psi_U - \psi_{UU})\,, \tag{4.28}$$

where D, U and UU denote the computation nodes downstream , first upstream and second upstream of the correspondent surface respectively. For example, if the flow direction is from the western to the eastern side of the cell center, U is the P, UU represents the W, which is in this scenario, the second upstream and D, denotes the eastern cell center and E, denotes downstream of the eastern cell surface, e, as shown in the figure 4.2. $B(r)$ is the flux limiter function and can be determined as

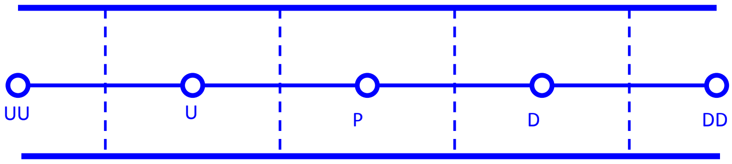

Figure 4.2: Labeling of the neighbor cells.

$$B(r) = \begin{cases} \dfrac{r(3r+1)}{(r+1)^2} & : r > 0 \\ 0 & : r \leqslant 0. \end{cases} \tag{4.29}$$

$B(r)$ is not linear and is a function of solution difference ratio, r,

$$r = \frac{|x_{i,U} - x_{i,UU}|}{|x_{i,D} - x_{i,U}|} \frac{\psi_D - \psi_U}{\psi_U - \psi_{UU}}\,, \tag{4.30}$$

where r is the ratio of the gradients of ψ between upstream and downstream side. Approximating the value at the cell surfaces using this TVD interpolation method has the advantages that more interpolation options are available with the implementation of one formulation. It shows low numerical diffusivity and bounded results without oscillation. Substituting $B(r)$ with different values yields different schemes, of which the following notable cases can be mentioned,

$$
\begin{aligned}
&B(r) = 0 \quad \text{or} \quad r = 0 && \Rightarrow && \text{Upwind interpolation} && (4.31)\\
&B(r) = r && \Rightarrow && \text{CDS interpolation (uniform mesh)} && (4.32)\\
&B(r) = \frac{(1.5r + 0.5)}{2} && \Rightarrow && \text{Quadratic upwind (QUICK)} && (4.33)
\end{aligned}
$$

4.3.3 Approximation of spatial gradient

4.3.3.1 Spatial gradient at the CV-face

The value of the gradients at the control volume's face centers coming in the diffusive term of the equation 4.17 are treated in the `FASTEST` using the second order approximation suggested by Lenhäuser [78]. Performing the coordinate transformation operator for $\frac{\partial \psi}{x_i})_e$ delivers

$$
\left(\frac{\partial \psi}{x_j}\right)_e = \frac{\phi_e^{ij}}{\mathfrak{J}_e}\psi_e^i \qquad \mathit{having} \quad i, j = 1, 2, 3 \tag{4.34}
$$

where

$$
\begin{aligned}
\psi_e^1 &= (\psi_E - \psi_P),\\
\psi_e^2 &= (\psi_N - \psi_S + \psi_{NE} - \psi_{SE}),\\
\psi_e^3 &= (\psi_T - \psi_B + \psi_{TE} - \psi_{SE}),\\
\phi_e^{1j} &= \epsilon_{jkl}[(x_{k,N} - x_{k,S} + x_{k,NE} - x_{k,SE})][(x_{l,T} - x_{l,B} + x_{l,TE} - x_{l,BE})],\\
\phi_e^{2j} &= \epsilon_{jkl}[(x_{k,T} - x_{k,B} + x_{k,TE} - x_{k,BE})[(x_{l,E} - x_{l,P})],\\
\phi_e^{3j} &= \epsilon_{jkl}[(x_{k,E} - x_{k,P})][(x_{l,N} - x_{l,S} + x_{l,NE} - x_{l,SE})],\\
\mathfrak{J}_e &= (x_{j,E} - x_{j,P})\phi_e^{1j}
\end{aligned}
\tag{4.35}
$$

4.3.3.2 Spatial gradient at the CV-center

With minor differences, the same procedure is performed to calculate the spatial gradient at the control volume center considering the coordinate transformation. This time instead of using the neighbor cell centers, the center of the correspondent control volume surfaces, e, w, n, s, t, b are designated to perform similar computation. this yields

$$
\begin{aligned}
\psi_P^1 &= (\psi_e - \psi_w),\\
\psi_P^2 &= (\psi_n - \psi_s),\\
\psi_P^3 &= (\psi_t - \psi_b),\\
\phi_P^{1j} &= \epsilon_{jkl}[(x_{k,n} - x_{k,s})][(x_{l,t} - x_{l,b})],\\
\phi_P^{2j} &= \epsilon_{jkl}[(x_{k,t} - x_{k,b})[(x_{l,e} - x_{l,w})],\\
\phi_P^{3j} &= \epsilon_{jkl}[(x_{k,e} - x_{k,w})][(x_{l,n} - x_{l,s})],\\
\mathfrak{J}_P &= (x_{j,e} - x_{j,P})\phi_P^{1j},
\end{aligned}
\tag{4.36}
$$

4.4 Temporal discretization

Rewriting the equation 4.17, in a way that the accumulation term is on the left side and the other terms are moved to the right hand side, delivers:

$$\left(\frac{\partial}{\partial t}\rho\psi\right)_P \delta V = \sum_k \left(\frac{\Gamma_\psi}{J}\frac{\partial\psi}{\partial\zeta_j}\beta_{ji}\right)_k n_j\delta S_k - \sum_k \left(\rho u_j\psi n_j\right)_k \delta S_k + \left(\dot{\omega}_\psi\right)_P \delta V. \qquad (4.37)$$

All of the terms in this equation are dicretized following the previous sections. In this section the way the temporal derivative is treated in the `FASTEST` will be explained. This equation can be considered as

$$\left(\frac{\partial\psi}{\partial t}\right)_P = F(\psi, t) \qquad (4.38)$$

If the simulation has been performed until the nth time step and value ψ at the $(n+1)th$ time step is asked, this equation can be approximated as either

$$\frac{\psi^{n+1} - \psi^n}{\Delta t} = F(\psi, t)^*, \qquad (4.39)$$

where ψ^n and ψ^{n+1} are the values of ψ at the time t^n and t^{n+1} respectively. t^n and t^{n+1} are related to the total time, t as

$$t^{n+1} = t^n + \Delta t \quad with \quad t^n = n.\Delta t \qquad (4.40)$$

There are several options considering treatment of $F(\psi, t)^*$. The first option is the fully implicit Euler method which is first order of accuracy in time. For this method, $F(\psi, t)^*$ is considered to be at time t^{n+1}

$$\frac{\psi^{n+1} - \psi^n}{\Delta t} = F(\psi, t)^{n+1}. \qquad (4.41)$$

This means that at each new time step an equation system for each transport variable has to be solved. As it is said in the previous chapters, the transport variables in a reacting system has to be computed coupled. Considering this and the data exchange needed to solve the coupled equation system in using implicit method iteratively, it can be said although implicit method has a broad stability zone performing von Neumann stability analysis [52], [2], [22], it is considerably more expensive than some other methods. Another option is to take the known value of $F(\psi, t)^*$ at current time step, n so that

$$\frac{\psi^{n+1} - \psi^n}{\Delta t} = F(\psi, t)^n . \qquad (4.42)$$

Rewriting this equation and bringing the known variables to the right hand side gives

$$\psi^{n+1} = \psi^n + \Delta t.F(\psi, t)^n . \qquad (4.43)$$

This is the Euler explicit time discretization for which it is not needed any more to solve an equation system. Albeit it shows instability behavior if setting bigger time step, it is computationally appreciably cheaper comparing to Euler implicit method. Since during the large eddy simulations performing for reacting system, Δ is set to be fairly small, Euler explicit method is taken to discretize the temporal derivative. To prevent expensive computational cost of Euler implicit method and have the advantages of Euler explicit method and also to get higher order of accuracy in time, a three-stage explicit Runge-Kutta scheme has been implemented in `FASTEST` which will be described here briefly. In this scheme like other Runge-Kutta schemes, at each time step, three stages are defined on which the intermediate variables $\psi^{(i,1)}$ and $\psi^{(i,2)}$ are calculated as follows:

$$\begin{aligned}\psi^{(i,1)} =& \psi^{n} + \alpha 1 \Delta t F(\psi, t)^{n}\\ \psi^{(i,2)} =& \psi^{n} + \alpha 2 \Delta t F(\psi, t)^{(i,1)}\\ \psi^{(n+1)} =& \psi^{n} + \alpha 3 \Delta t F(\psi, t)^{(i,2)}\end{aligned} \tag{4.44}$$

where $\alpha 1$, $\alpha 2$ and $\alpha 3$ are the Runge-Kutta stage coefficients and are set to 1/3, 1/2 and 1 accordingly and $(i,1)$ and $(i,2)$ denote the first and second Runge-Kutta intermediate stage. Having temporal discretization using this scheme, has the advantage that only the two arrays containing ψ^{n} and one of the intermediates are saved at each time step. The intermediate variables $\psi^{(i,1)}$, $\psi^{(i,2)}$ are saved and overwritten by each other and eventually by $\psi^{(n+1)}$. Three stage explicit Runge-Kutta scheme is a loq storage method of time discretization which has third order of accuracy in time and is more stable than the common Euler explicit method. For more information please refer to [74], [13].

4.5 Pressure correction

The momentum equation mentioned in basic equations delivers the three velocity components,

$$\frac{\partial}{\partial t}(\rho u_i) + \frac{\partial}{\partial x_j}(\rho u_i u_j) = \frac{\partial}{\partial x_j}\left(\mu\left(\frac{\partial u_i}{\partial x_j} + \frac{\partial u_j}{\partial x_i}\right) - \frac{2}{3}\mu\frac{\partial u_k}{\partial x_k}\delta_{ij}\right) - \frac{\partial p}{\partial x_i} + \rho g_i. \tag{4.45}$$

If the relative pressure is known and the low mach number assumption is applied, the flow can be treated like an incompressible flow and the equation system can be iteratively computed using the discretisation schemes and solution methods explained in the previous section. But with the velocity components gotten here, the continuity equation will not be satisfied as long as the relative pressure is not exactly known. To get an appropriate pressure at current time step, so that the continuity equation is satisfied, is a big challenge in CFD. One problem is that the pressure does not own an specific equation for itself! It is also decoupled from density, if the low mach number assumption is applied or in other words, if the flow assumed to be incompressible. One way is to combine momentum and continuity equation and build an equation for pressure. This is called pressure-velocity coupling for which a lot of methods have been developed. Most of these methods have similar approaches that they combine the discretized continuity equation with the momentum equation and construct a discretized Poisson equation for pressure or the pressure correction. In FASTEST, the fractional step projection method suggested by Chorin(1968) has been implemented.

Applying the dicretization schemes introduced in previous sections of current chapter for the momentum equation gives,

$$\begin{aligned}(\rho u_j)^{(i,m*)} &= (\rho u_j)^n + \alpha_m \Delta t F^{(i,m-1)} \\ &= (\rho u_j)^n + \alpha_m \Delta t \left(G^{(i,m-1)} - \frac{\partial p^{(i,m-1)}}{\partial x_j} \right)\end{aligned} \tag{4.46}$$

herein m represents mth Runge-Kutta stage and G denotes the sum of convective and diffusive term and is equal to the subtraction of pressure term from F. As it is mentioned above, using ρu_j calculated in this Runge-Kutta step does not satisfy the conservation equation for mass. Adding a momentum correction $(\rho u_j)'$ to overcome this shortcoming yields

$$(\rho u_j)^{(i,m)} = (\rho u_j)^{(i,m*)} + (\rho u_j)' \tag{4.47}$$

The corrected momentum will satisfy the continuity equation if the pressure is also corrected as follows

$$p^{(i,m)} = p^{(i,m-1)} + p'. \tag{4.48}$$

Rewriting the momentum equation for mth intermediate stage and inserting the equation 4.48 gives

$$(\rho u_j)^{(i,m)} = (\rho u_j)^n + \alpha_m \Delta t \left(G^{(i,m-1)} - \frac{\partial p^{(i,m-1)}}{x_j} - \frac{\partial p'}{\partial x_j} \right) \tag{4.49}$$

To find the relation between the corrected pressure, p' and the corrected momentum, $\rho u_j'$, the equation 4.46 is subtracted from the momentum 4.49 using the equation 4.47 yields

$$(\rho u_j)' = -\alpha_m \Delta t \frac{\partial p'}{\partial x_j}. \tag{4.50}$$

Again the conservation equation for mass can be reconstructed using the formula 4.47 so that

$$\frac{\partial \rho}{\partial t} + \frac{\partial}{\partial x_j}(\rho u_j)^{(i,m*)} + \frac{\partial}{\partial x_j}(\rho u_j)' = 0. \tag{4.51}$$

After substituting the last term of this equation with the right hand side of the equation 4.50 and some mathematical simplifications we have

$$\frac{\partial}{\partial x_j}\left(\frac{\partial p'}{\partial x_j}\right) = \frac{1}{\alpha_m \Delta t}\left(\frac{\partial \rho}{\partial_{x_j}} + \frac{\partial}{\partial x_j}(\rho u_j)^{(i,m*)}\right). \tag{4.52}$$

Note that $\frac{\partial}{\partial x_j}\left(\frac{\partial p'}{\partial x_j}\right)$ is of the form Laplace operator in the Cartesian coordinates $(\nabla.\nabla p')$. Laplacian operator is the product of the divergence$(\nabla.)$ and the gradient $(\nabla p')$ (divergence comes from continuity equation and gradient from momentum). This equation can be discretized at the cell surfaces similar to those that have been outlined in previous subsections. The discretized equation has the form

$$\sum_k \left(\frac{\partial p'}{\partial x_j} n_k\right) = \frac{\epsilon_{\dot{m}}}{\alpha_m \Delta t} \tag{4.53}$$

where

$$\epsilon_{\dot{m}} = \left.\frac{\partial \rho}{\partial t}\right|_P \delta V + \sum_k \left((u_j)^{(i,m*)} n_k \big|_k \right). \tag{4.54}$$

Here $\epsilon_{\dot{m}}$ represents the amount of the mass needed to balance the continuity equation in the correspondent control volume. Performing this procedure for all of the control volumes of the domain yields an equation system of the form

$$\mathbf{A}\mathbf{p}' = \mathbf{b}. \tag{4.55}$$

This linear algebraic equation system can be solved using an ILU matrix decomposition method (incomplete lower and upper triangular matrix decomposition).ILU matrix decomposition is performed in `FASTEST` using SIP-Solver suggested by Stone [116] which has an effective algorithm specially to take advantage of tridiagonal matrices. For more information see [20],[19], [109] and Fastest-3D user manual.

4.6 Boundary conditions and initialization

Until now we have reached a discretized form of an algebraic equation system gotten from coupled differential equation system derived for the reacting flows. Like all other differential equations, for these equations, initial and boundary values need to known. Considering the spatial discretization schemes outlined in the previous subsections and since there are no neighbor cells at the boundaries, the values of the variables at boundaries have to be known during the whole simulation. There are generally three types of boundary conditions implemented and used in FASTEST-3D, known as *inlet*, *outlet* and *solid wall* boundary conditions. In this section, first it will be briefly explained how the initialization is performed to simulate reacting flows with multi-component chemistry, then the boundary conditions implemented in FASTEST and also the modification done due to multi-component chemistry will be described.

4.6.1 Initialization

Since the simulations in this work were performed with detailed chemistry, the initialization, specially for mass fractions and temperature is extremely decisive and needs special care.

MASS FRACTIONS

The mass fractions, Y_k are prescribed at each point of the domain. Their values are not allowed to disturb the conservation of mass so that at each cell we should have,

$$\sum_{k=1}^{N} Y_k = 1. \tag{4.56}$$

If this is not the case, the continuity equation will not be anymore satisfied at the beginning of the simulation and one will have a rough start to overcome this self made wrong initialization. In worst cases it can also cause divergence exactly after simulation is started. It should also be mentioned that the initialized mass fractions in the neighborhood of the inlet are not allowed to have sudden gradients comparing to inlet.

TEMPERATURE PROFILE

The simulations performed for reacting flows using multi-component chemical mechanisms are extremely sensitive to temperature initialization. The reason is that the temperature is sent to chemical solver and the chemical solver senses even minimum nonphysical temperature jump, variation or fluctuation, as if there is a source term for heat at that area. Special care should be also taken in the vicinity of the walls and inlets. Any abrupt temperature difference between the value initialized for the field and those set for the walls or inlet, causes consequently dramatic density gradients which can behave as a divergence threat for the simulation or take time to be smoothed. It is recommended to set the temperature in the first cells of the domain in the vicinity of the inlet, equal to the inlet temperature. The smooth change of the temperature prevents the abrupt change in the density which is one of the reasons of the velocity fluctuation at the start of the simulation.

4.6.2 Inlet boundary condition

The Dirichlet boundary conditioned has been implemented and used for all of the variables needed to be known at inlet. This boundary condition sets a constant value condition as

$$\psi = cte \tag{4.57}$$

Again here special care has to be taken for mass fractions, Y_k. For each species, a correspondent mass fraction is defined. The sum of the mass fractions of the species at inlet are not allowed to overshoot the unity.

4.6.3 Outlet boundary condition

On the contrary to inlet boundary condition for which the data is known and imposed to have a constant value, there is no information in advance at the outlet.

NEUMANN CONDITION

The most common way to set a value at outlet is to use the Neuman boundary condition. In this approach the value of the outlet cells normal to outlet surface is set to be equal to the penult row neighbor cells. This means a zero gradient boundary condition is applied as

$$\frac{\partial \psi}{\partial x_j} n_j = 0. \tag{4.58}$$

This condition is also easy to implement and widely used in CFD codes and is also applied in FASTEST for mass fractions, temperature and other scalars.

CONVECTIVE BOUNDARY CONDITION

Using the zero gradient outlet boundary condition for velocity could cause instabilities in transient flow situations. Another way to give a value for outflow velocity avoiding this shortcoming is the outflow convective boundary condition suggested by Richter et al. [106]. Outflow convective boundary condition is defined as follows

$$\frac{\partial u_n}{\partial t} + U_c \frac{\partial u_n}{\partial n} = 0. \tag{4.59}$$

herein n denote the vector outward, normal to the boundary and U_c represents convective outflow velocity which is equal to averaged convective velocity at outlet surface. Using this method helps to prevent nonphysical pressure fluctuations at outlet which are the dominant reason for the instabilities mentioned above.

Applying one of the last two equations is not enough to satisfy the continuity equation. To conserve the mass globally, there are still some steps to be performed at outlet. Assume $\dot{m}_{in}$ and $\dot{m}_{out}$ are the mass fluxes at inlet and outlet respectively. The difference of these two fluxes must be zero to satisfy the mass conservation

$$\dot{m}_{in} - \dot{m}_{out} = \int_V \frac{\partial \rho}{\partial t} dV = 0, \tag{4.60}$$

where V is the volume of the whole domain. This means that the integration of the time derivative of the density over the whole domain should be equal to zero. If this is not the case, the velocity at outlet has to be scaled as follows

$$u_{out} = \frac{\dot{m}_{in} - \displaystyle\int_V \frac{\partial \rho}{\partial t} dV}{\dot{m}^*_{out}} \tag{4.61}$$

where $\dot{m}^*_{out}$ is calculated using the already existing velocity at outlet. This correction makes the relation 4.60 true and conserves the mass globally.

4.6.4 Symmetry/Solid wall

For symmetry boundaries, a zero gradient condition is applied for the wall normal component and scalars like temperature and mass fractions. Considering this for the temperature provides an adiabatic wall, with zero heat flux through the wall. For velocity component normal to the wall, a symmetry boundary condition provides zero mass flux/zero wall normal component across the wall. The mass fractions at the solid walls are treated similar to symmetry walls applying the Neumann boundary condition. At solid walls, a fixed constant temperature is set which means heat can flux across the wall. No slip boundary is applied at solid walls for velocity components. This means the velocity component tangential to the wall is equal to the velocity of the wall. There is an option in FASTEST which provides separate treatment of the boundary conditions for temperature and velocity. This option makes it possible to have e.g. adiabatic solid wall or setting a symmetry boundary condition for velocity while heat can flux through the wall.

Chapter 5

Verification

Generally, one can say that numerical simulation of a fluid dynamic system consists of first, describing the physical problem using mathematical equations and then using numerical methods to solve these equations. This system of equations is a combination of algebraic and differential equations, written in a numerically solvable form, the discretized form. Next, one has to find appropriate temporal and spatial discretization methods for which the set of discretized equations is to be solved. This is implemented in a program generically called *Navier–Stokes solver*.

This multistep process is prone to various errors. There are two kinds, however, that are more serious, namely, wrong choice of mathematical model, and flawed implementation.

To make sure about accuracy of the mathematical model and the implementation one has to go through *verification*. There are different methods of verification proposed in the literature [107], [108], [5], [91]. One obvious way is to compare the results of a specific setting with preexisting solution. Since Navier–Stokes equations are not analytically solvable in most cases, this method is applicable to simple geometries where analytical solutions to Navier–Stokes equations are achievable, for instance, the Blasius solution of laminar boundary layer for a flow over a flat plate. For more complicated configurations, it is suggested to begin the verification process with a very simple configuration for which the physical behavior can be easily predicted, like one- or two-dimensional simulations. A more sophisticated strategy is to compare the results with another model whose accuracy is already confirmed. This comes basically down to judging the results based on quantitative comparisons to another code which could use different spatial or temporal discretization to simulate the same configuration.

In this chapter, first, the source terms obtained from a chemical solver coupled to the FASTEST are compared to the source terms which are calculated by SENKIN. In the next subsections, the behavior of the model will be tested for pure convection. Then the results of a 1-dimensional simulation of a lean to reach combustion of the methane-air mixture with $Le = 1$, and then mixture-averaged are compared to those computed by Chem1D [28]. Next, two simulations of methane-air combustion performed in lean and rich burn conditions will be quantitatively compared to a flamelet calculated by Chem1D. At the end, a two-dimensional simulation for a burner-stabilized laminar premixed flame is performed in multiple dimensions to verify the implementations based on comparisons to the results published by van Oijen [120].

5.1 1D Verification

5.1.1 Verification of the source terms(0-D simulations)

The first step in implementation of multi-component combustion is to calculate the source terms of the species i.e. their reaction rates. Due to the typically stiff of system of equation established to calculate the reaction rates, one has to make use of solvers particularly developed for stiff systems. In this work the solver DASSL is used which is written in FORTRAN 77 for ordinary differential equations and is made available on public domain by Petzold [99, 100, 12]. A modified and rebuilt fork of DASSL is available under the name DASAC [69, 70] for solving partial differential equations in SENKIN [82, 81], a sub-program of CHEMKIN [66] whose purpose is to simulate reacting homogeneous gas mixtures using multi-component chemical mechanisms. SENKIN also uses "chemkin.f" to build the mechanism in a useful format to compatible with the solver.

5.1.1.1 Perfectly stirred reactor model(PSR)

The time evolution of a homogeneous reacting gas mixture in a closed system is governed by

$$\rho \frac{dY_k}{dt} = \dot{\omega}_k \,, \tag{5.1}$$

$$\rho c_{pk} \frac{dT}{dt} = - \sum_{k=1}^{N} \dot{\omega}_k h_k , \tag{5.2}$$

where N is the number of species. These two equations are solved using SENKIN. Note that these equations are the same of mass and energy transport equations given in chapter 2, but simplified for a mixture with zero velocity components. This can denote a zero-dimensional combustion system because no convection and no spatial derivative is present, which is exactly what is we need to simulate a perfectly stirred reactor [34].

Two simulations are carried out similar to those by Espada (2010) [34] for comparison in order to show the relative improvements in implementation. The first one has to do with perfectly stirred reactor of the hydrogen-oxygen mixture and the second one with the simulation of PSR with methane-air mixture.

The boundary conditions and settings of simulations are relatively simple. The ignition temperature is set to $1400\,[K]$ and the default hydrogen-air mechanism of CHEMKIN is chosen. The total integration time is $10^{-4}\,[sec]$, and mass fractions are set to $Y_{N2} = 0.745$, $Y_{O2} = 0.226$, and $Y_{H2} = 0.028$. The mixture is assumed to burn with constant pressure. Finally, the coefficients corresponding to mass fractions of hydrogen-air global reaction have to be given in compliance to SENKIN input format. The results can be seen in figures 5.1a and 5.1b . In figure 5.1a the temperature profile is demonstrated which starts at $1400\,[K]$ and goes up to $2500\,[K]$. In figure 5.1b the mass fractions of major species and intermediate profiles are shown.

The perfectly stirred reactor is simulated a second time for a methane-air mixture. The ignition temperature is set to $1800\,[K]$ and the total time is $5 \times 10^{-4}\,[sec]$. The mass

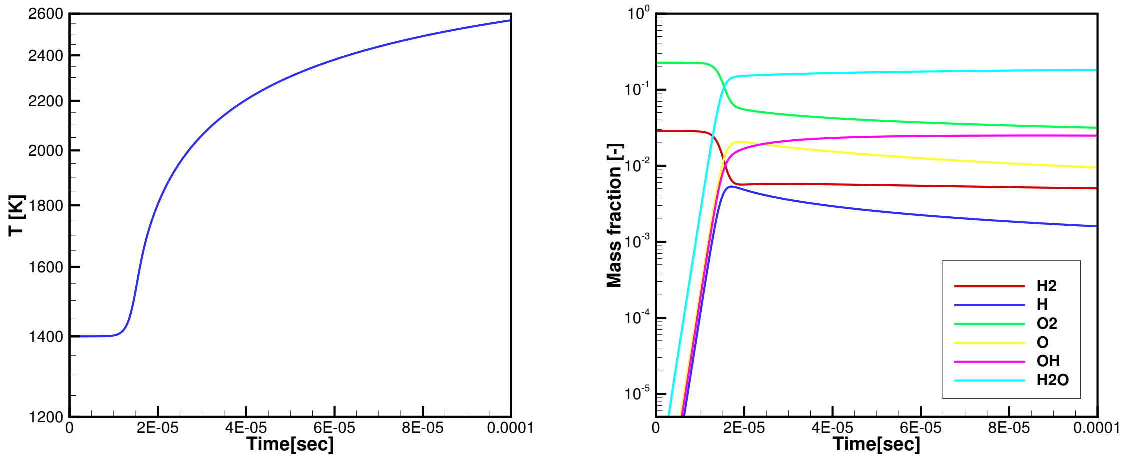

(a) Temperature $[K]$

(b) Mass fractions $[-]$

Figure 5.1: The profiles of temperature and mass fraction of $H2, H2O, OH, O2, H$ and O in the simulation of perfectly stirred reactor calculated by SENKIN for hydrogen-air mixture.

fractions are set to $Y_{N2} = 0.725$, $Y_{O2} = 0.22$ and for methane, $Y_{CH4} = 0.055$. The methane-air chemical mechanism developed by Smooke et al. [88] is chosen which includes 16 species and 25 reactions. The remaining settings are left unchanged. The results of the PSR for methane-air mixture are shown in figures 5.2a and 5.2b.

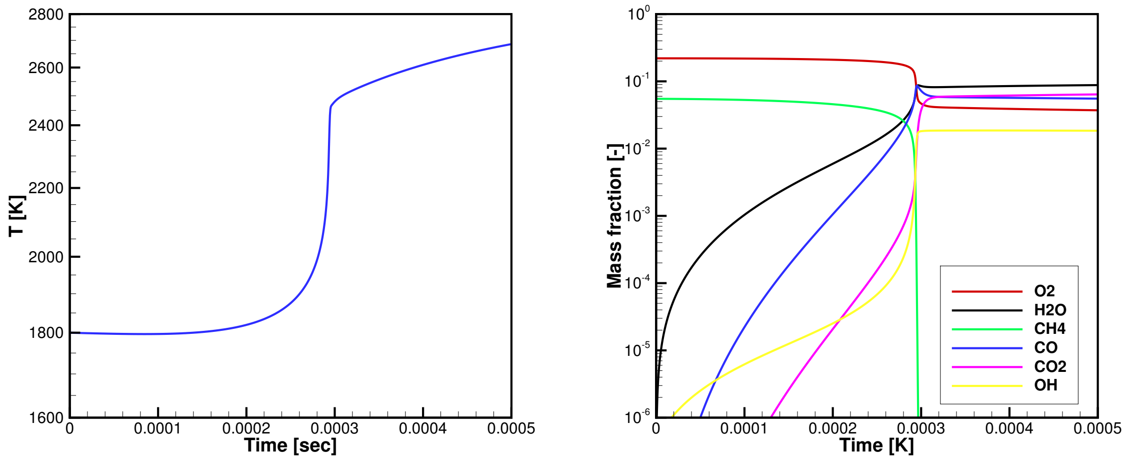

(a) Temperature $[K]$

(b) Mass fractions $[-]$

Figure 5.2: The profiles of temperature and mass fraction of $H2O, OH, CH4, O2, CO$ and CO_2 in the simulation of perfectly stirred reactor calculated by SENKIN for methane-air mixture.

5.1.1.2 Plug flow reactor (PFR)

For an axial steady state flow with constant density, which is perfectly mixed in radial direction and has no mixing in axial direction, the mass and energy transport equations of species are rewritten as

$$\rho u \frac{dY_k}{dx} = \dot{\omega}_k \,, \tag{5.3}$$

$$\rho u c_p \frac{dT}{dx} = -\sum_{k=1}^{N} \dot{\omega}_k h_k \,. \tag{5.4}$$

For a one-dimensional simulation, if the velocity is set to $1\,[m/s]$ and the length of the domain is assumed to be equal to the total time of the perfectly stirred reactor (time-to-length transformed), equation (5.1) will look like (5.3) and the equation (5.2) has the exact structure of the forth equation. Therefore, we have a time-to-length transformation.

This transformation provides the opportunity to compare the results of the PSR calculated by `SENKIN` with simulations performed by `FASTEST`. With this procedure, the source terms of the transport equations calculated by `DASAC` can be verified.

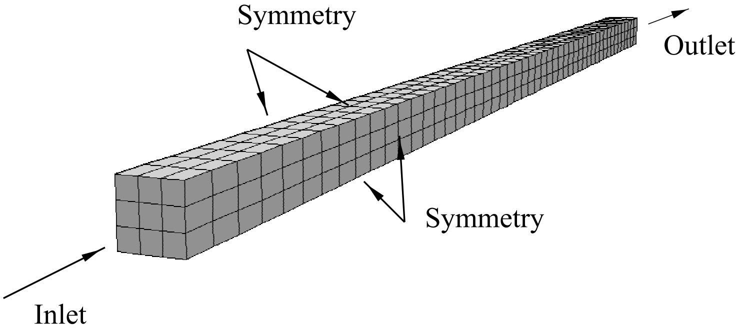

Figure 5.3: Sketch of the one-dimensional geometry used for `FASTEST` simulations [34].

Figure 5.3 shows the domain on which the plug flow reactor is simulated. It consists of 500 cells in axial direction and one cell in radial direction. As stated before, `FASTEST` adds a row of dummy cells around the domain to make the interpolation possible. The boundary conditions are inlet, convective outflow, and symmetric in radial direction. This type of geometry will be used for all of the one-dimensional simulations in this work. Therefore, the mesh considered here has $500 \times 3 \times 3$ cells. For the hydrogen-air simulation and methane-air simulations, the same chemical mechanisms as PSR are chosen. The length of the domain is scaled to $10^{-4}\,[m]$ and $5 \times 10^{-4}\,[m]$ for the H_2-air and CH_4-air reactions respectively. The iteration time step is set to $10^{-8}\,[sec]$.

Figures 5.4a and 5.4b demonstrate the results of plug flow reactor calculated by `FASTEST` compared to those of perfectly stirred reactor computed by `SENKIN`. In the first one, the temperature profiles of H_2-Air simulations are compared with each other. Both temperature profiles are completely congruent. They both begin at $1400\,[K]$ and end at around $2570\,[K]$. In 5.4b the mass fractions of O_2, H_2, H_2O, H, O and OH of PSR and PFR are shown. As it can be seen, PFR simulation yields identical mass fraction profiles and the results seems to be accurate and promising.

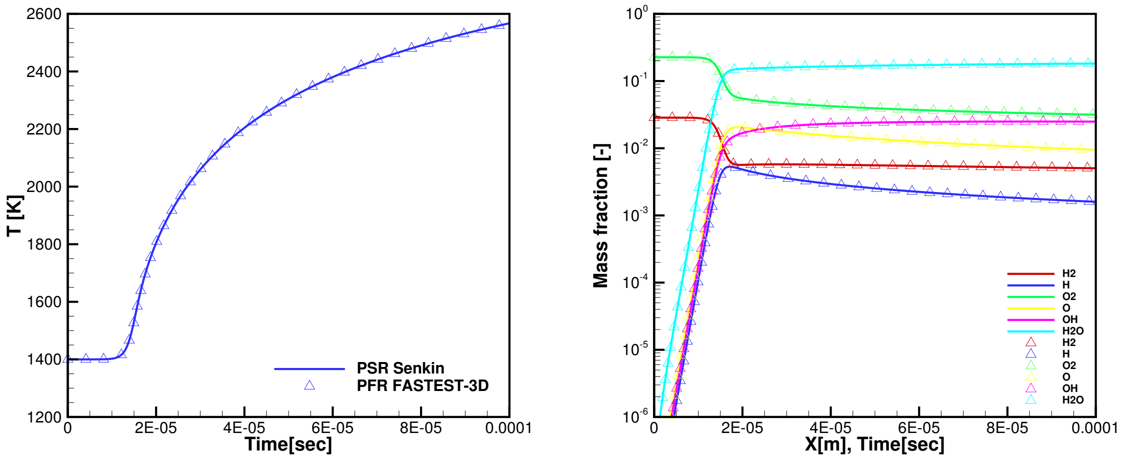

(a) Temperature $[K]$

(b) Mass fraction $[-]$

Figure 5.4: The profiles of temperature and mass fractions of plug flow reactor calculated by FASTEST for hydrogen-air mixture compared to results of the PSR computed by SENKIN. Solid lines present the results obtained from SENKIN, triangles present FASTEST.

In the next figures, the results performed for methane-air mixture are presented. In figure 5.5a the temperature profiles of both simulations are demonstrated. Here again both profiles are almost identical and no discrepancy can be seen. They both begin at 1800 $[K]$ and end up in 2700 $[K]$.

In figure 5.5b the plots of some major species and intermediates are illustrated. There is no discrepancy between the two simulations and even radicals like CO exhibit very good accuracy. At this stage it can be said that the process of incorporating the source term has been accomplished very well and the results are verified.

5.1.2 Verification of the convective term

For verifying the convective term no special configuration is considered. As long as accumulation term, diffusive term and the source term are absent, the initialized profiles move with constant convection velocity. So it is safe to say that this term is also verified. Therefore the first step is to eliminate the influence of other terms. To do so, the source term calculated by DASAC is set to zero. The thermal diffusion coefficient and also molecular diffusion coefficients are also set to zero. The simulation is initialized so that the mass fraction profiles of a stoichiometric methane-air mixture are smoothly combined with air using a hyperbolic tangent function.

Figure 5.6 shows how this step is performed. Since there is practically no chemical reaction involved in this step, only the convective terms have to be verified, and therefore a relatively large time step can be chosen; here $\Delta t = 10^{-6}\,[sec]$, as long as the CFL-number remains within stability limits. Similar to the previous example, a one-dimensional domain, with 512 cells in X-direction and 1 cells in the two other directions, was chosen. The temperature is set to constant and equal to 300 $[K]$, so that the mixture cannot react. The results of verification of the convective term are shown in figure 5.7. This figure presents the

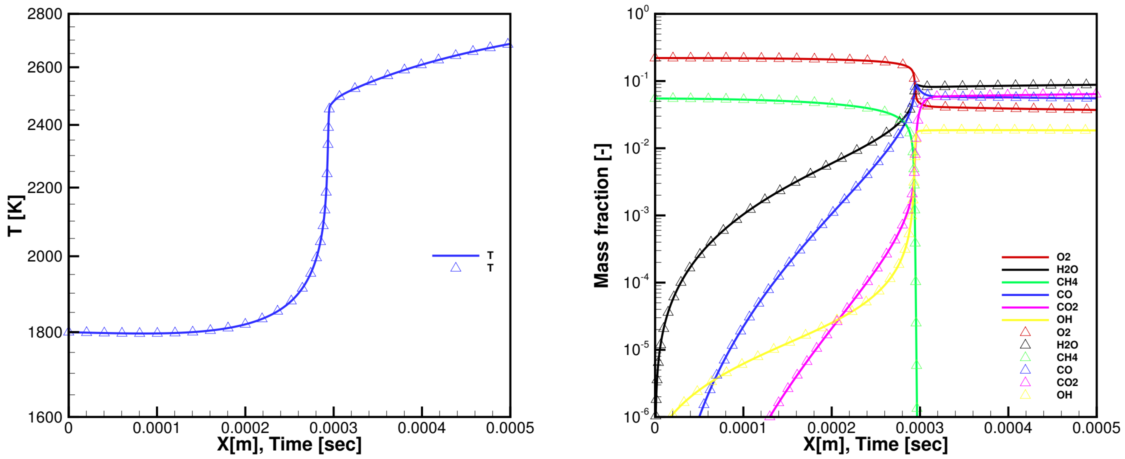

(a) Temperature $[K]$ (b) Mass fraction $[-]$

Figure 5.5: The profiles of temperature and mass fraction of plug flow reactor calculated by FASTEST for methane-air mixture compared to PSR computed with SENKIN. Solid lines present the results obtained from SENKIN, triangles present FASTEST.

convection profile of methane for a constant convective velocity in the absence of diffusion and reaction. Considering the profile of methane, for the convective term to be verified, the initialized profile has to march spatially equal, for equal temporal intervals within the domain. The results are plotted at $0, 5, 10, 15$ and $20\,[ms]$. Based on these results one can clearly state that the convective term is verified.

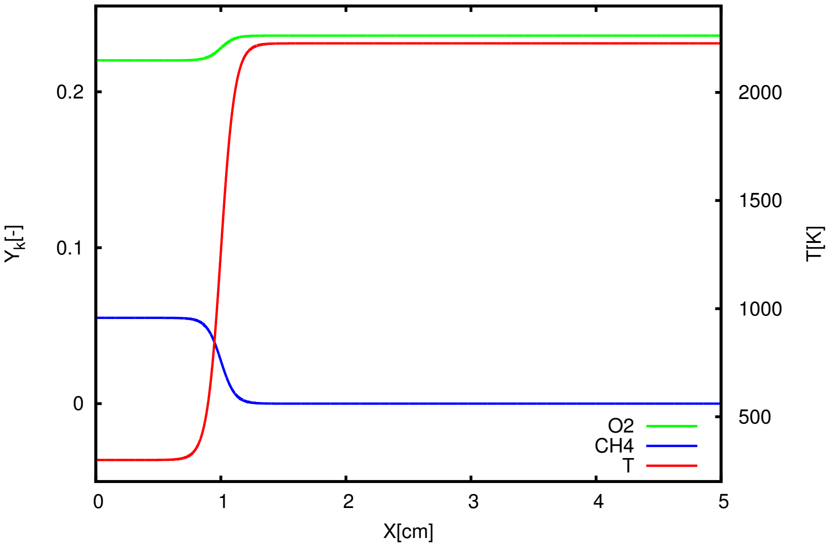

Figure 5.6: Initialization of the mass fractions and temperature profiles. The length coordinate is given in [cm].

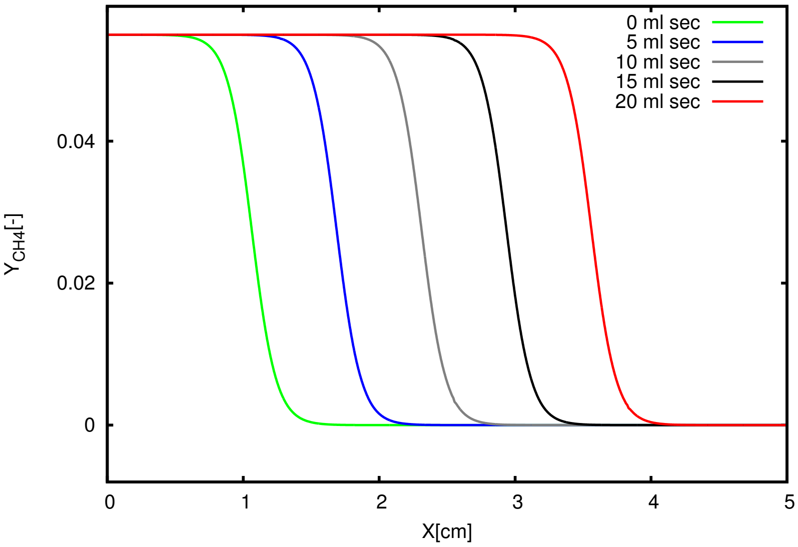

Figure 5.7: Convection of the mass fraction of methane for a constant velocity in the absence of diffusion at $0, 5, 10, 15$ and 20 ml[sec]. The length coordinate is given in [cm].

5.1.3 Verification of the diffusive term

As explained in chapter 2, depending on how the transport coefficients are defined, the simulation can be performed either under $Le = 1$ or under mixture-averaged settings.

LEWIS NUMBER EQUALS ONE

In this case the transport coefficients are temperature dependent only.

$$\rho D_{th} = 2.58 \times 10^{-5} \times \left(\frac{T}{298K}\right)^{0.69} \quad kgm^{-1}s^{-1}\,. \tag{5.5}$$

In this formulation, equal coefficients are assumed for all species. Therefore there is no special factor to be tracked to distinguish the correctness of the coefficients. But since the laminar burning velocity is approximately related to molecular diffusion through

$$s_l \approx \sqrt{D\omega}\,, \tag{5.6}$$

these coefficients will show their influence on the simulation during the verification of s_l.

MIXTURE-AVERAGED

In mixture-averaged formulation, which was explained extensively in the second chapter, the diffusion coefficient D_k of the species k is not only dependent on temperature but also on the molar mass of corresponding species k. This provides a quick, basic verification test case. Since in each cell it is assumed that the temperature is equal to average temperature of the cell, the coefficients can be checked to show their dependency on species mass fractions. This can be confirmed, if the smaller –lower mass– species like H-atoms or H_2 molecules have bigger diffusion coefficients – higher diffusion velocity – and for bigger species like CO_2 and H_2O_2 smaller diffusion coefficients are calculated.

To control this term, again the same 1-D mesh is used and the time step and inlet velocity are retained. Since this is a rough verification, the simulation does not need to be performed for a long time. Only one time step is enough to plot the diffusion coefficients. The results can be seen in figure 5.8. The diffusion coefficients of H-atoms and H_2 as examples of small species and those of CO_2 and H_2O_2 as cases of big species are plotted in this figure. It can be seen that the first stage of the verification is successful. They show their impact on the flame shape and on the calculation of burning velocity later.

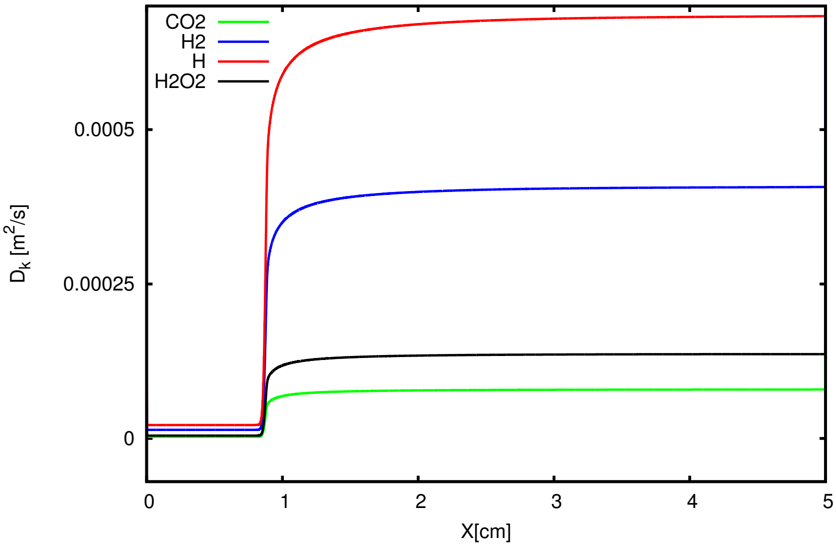

Figure 5.8: The profiles of the diffusion coefficients of H_2, H, CO_2, H_2O_2, The length coordinate is given in $[cm]$.

5.1.4 Verification of the burning velocity, adiabatic temperature and transport coefficients, $Le = 1$

Once all the implemented functions have been tested, the code can be verified through comparison to a second code. To do this, we use `Chem1D` which provides comparable flamelets. Both simulations are performed for a stoichiometric methane-air mixture. The inlet temperature is set to $T_{in} = 300\,[K]$. Convective outflow boundary condition is set and mass fractions are initialized to develop smoothly from stoichiometric mixture to pure air is represented by hyperbolic tangent function. The same is done for the temperature profile which smoothly increases from ambient temperature to the stoichiometric methane-air adiabatic flame temperature. This can be done using `Chem1D` flamelets which can be calculated in advance.

Another important task here is the laminar burning velocity. If all of the terms are implemented correctly, the flame has to propagate with a correct burning velocity, which can be calculated using one of the three formulas provided in the third chapter. Fortunately, `Chem1D` provides also an exact computation of the burning velocity and adiabatic flame temperature. Chem1D is equipped with adaptive mesh method. This means for higher gradients, the cell sizes become gradually smaller. So if for any size of the mesh the FASTEST simulation provides promising results, one can say that the influence of the mesh refinement does not need any more to be checked.

On a fifty millimeter long one-dimensional domain the simulation is carried out. The domain is divided into 512 cells in flow direction which yields approximately one hundred micro meter for each cell. To check the exactitude of the burning velocity, the inlet velocity is set equal to the laminar burning velocity calculated by Chem1D, which is $s_l = 0.29031218\,[m/s]$.

If the flame is simulated correctly, non of the flame profiles – including mass fractions, temperature, source terms, and so on – are allowed to propagate toward outlet or against the inlet. This means a stationary flamelet is simulated. Chem1D predicts the adiabatic flame temperature for this mixture to be $T_{ad} = 2227\,[K]$. Results can be seen in figure 5.9 and 5.10.

The first parameter, which can be immediately checked, is the burning velocity. Since the inlet velocity is chosen equal to the laminar burning velocity of the mixture, the stability of the flamelet is the first confirmation for exactness of the burning velocity.

The next step is to control the value of the computed adiabatic temperature of the given mixture. The temperature profile is demonstrated in figure 5.9a. Clearly the profiles of the temperature calculated by Chem1D and FASTEST are identical and the code has performed well. The exact adiabatic temperature is achieved and the curvature of the temperature profiles, which is a sign of correct thermal diffusion coefficient, is also identical to the one computed by Chem1D. Having these, one can say that the calculation of the temperature is correctly accomplished and is verified.

The first major species whose profile is not shown here is nitrogen. It is assumed that nitrogen is an inert gas as it does not participate in the reaction actively. It has to have a constant value from the inlet to outlet and during the reaction.

The next parameter to be verified is the value of the main species/products at equilibrium state – here short before outlet – the sum of which has to be equal to unity. They are not allowed to differentiate from those values calculated by Chem1D and must attain the same results as Chem1D. Here, the complete profile from the inlet within the flame brush and at the outlet, which is in equilibrium, will be investigated.

Figures 5.9b, 5.9c and 5.9d illustrate the profile of mass fractions of $\mathrm{CO_2}, \mathrm{CO}$ and $\mathrm{H_2O}$ correspondingly. They are all identical to the profiles calculated by Chem1D. They get the same share of the mass fraction and coincide with profiles obtained from Chem1D.

Next group of species are those which have bigger share of mass fraction at equilibrium state compared to other intermediates. They are OH, O and $\mathrm{H_2}$. Their profiles are shown in figures 5.9e, 5.9f and 5.10a respectively. Generally, in a combustion simulation it is more difficult to predict the exact values of the intermediates which have a shorter existence time. Here, the simulation yields precise values for the above mentioned radicals in all three parts of the domain. Even the peak of profiles, which represent the maximum amount of the radical during the reaction, is anticipated accurately.

Last group of species to be investigated are the short-existing intermediates like HCO and $\mathrm{HO_2}$. They are shown in figures 5.10b–5.10f. Precise computation of these types of short-existing radicals is very difficult and a lot of factors like mesh size and precision of calculated transport coefficients should be taken into account to acquire appropriate results.

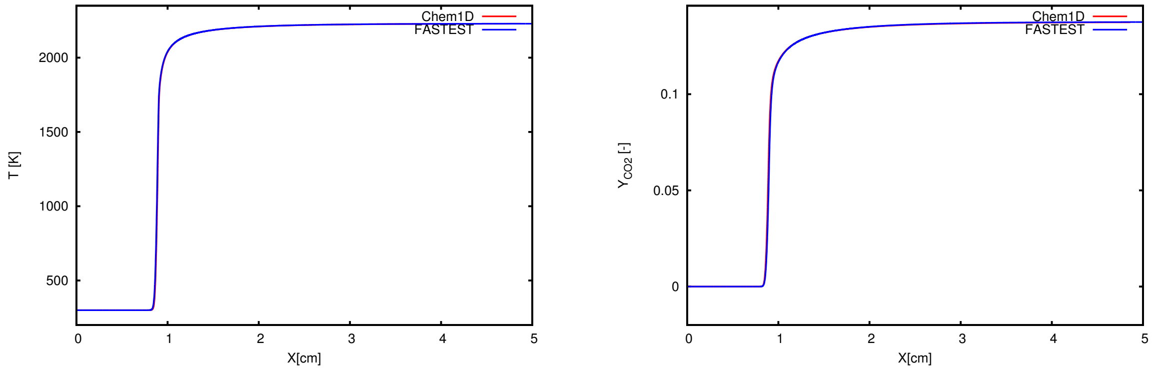

(a) Temperature $[K]$ (b) CO2 $[-]$

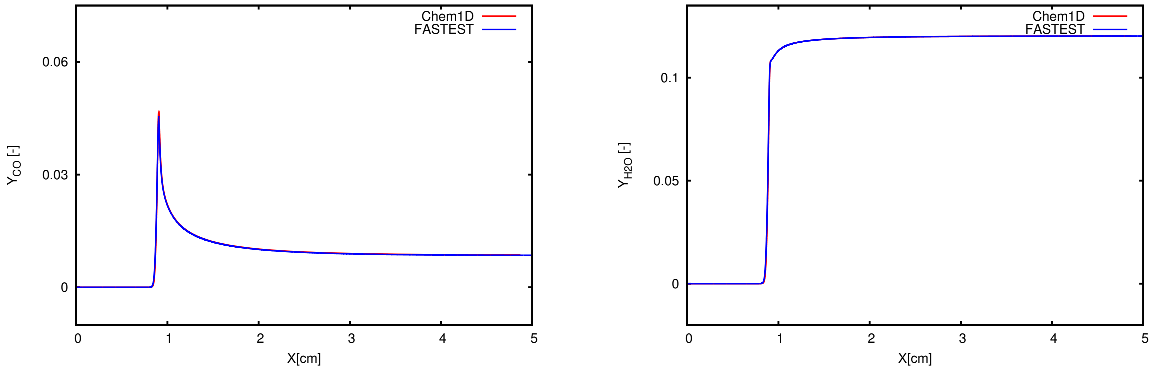

(c) CO $[-]$ (d) H2O $[-]$

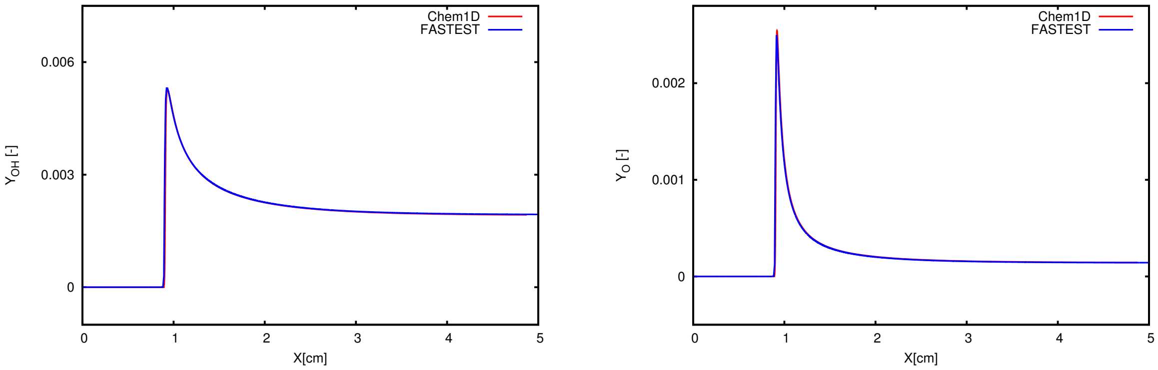

(e) OH $[-]$ (f) O $[-]$

Figure 5.9: Profiles of the temperature and mass fraction in a one-dimensional simulation of stoichiometric methane-air mixture with the transport coefficients calculated with LE=1 formulation. The length coordinate is given in [cm].

It is clear that although the maximum values of CH_3, H and HO_2 are too small, the simulation yields promising values compared to those simulated by Chem1D. They congruently overlay the curves generated by verification code and have the same maximum value.

Contrary to CH_3, H and HO_2, there are problems with computation of HCO and H_2O_2 mass fractions. Their profiles do not have the same value as the results obtained from Chem1D. This can have various causes of error, e.g. the mesh size.

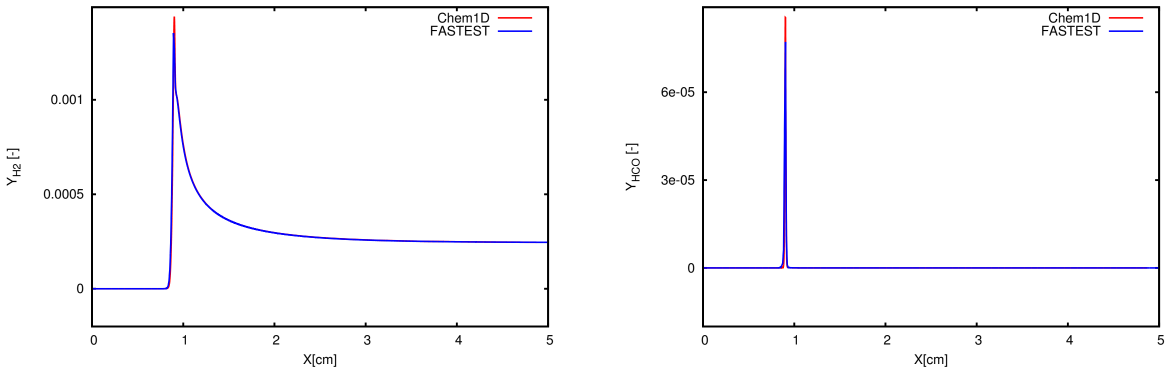

(a) H2 [−]

(b) HCO [−]

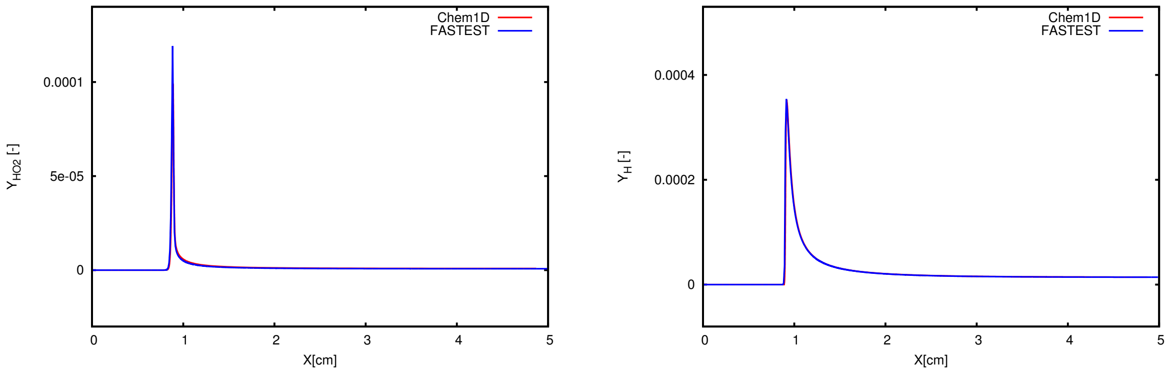

(c) HO2 [−]

(d) H [−]

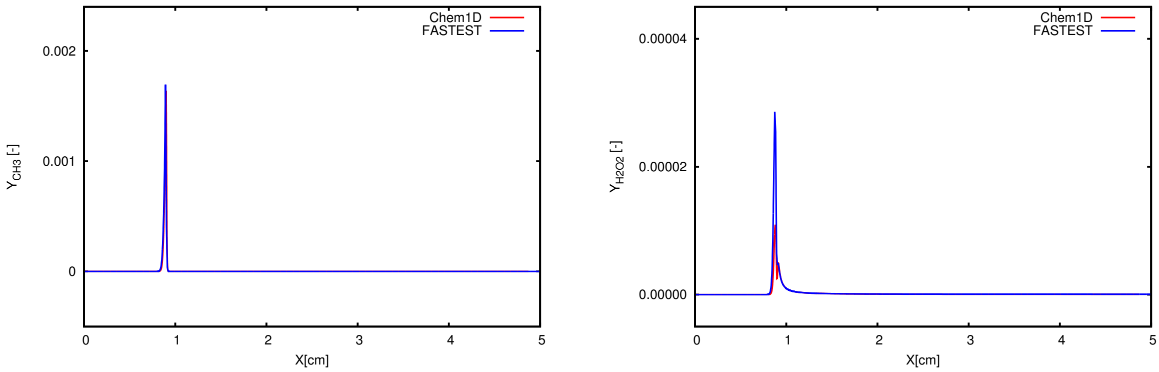

(e) CH3 [−]

(f) H2O2 [−]

Figure 5.10: Profiles of the mass fraction in a one-dimensional simulation of stoichiometric methane-air mixture with the transport coefficients calculated with LE=1 formulation. The length coordinate is given in [cm].

To investigate mesh-dependency, two other simulations with 1024 and 2048 cells in flow direction were performed. Note that they have half and one-quarter the cell sizes of the current geometry. The results are shown in figure 5.11b and 5.11a. They show improvement as the mesh is refined, and do not deviate dramatically from those anticipated by `Chem1D`.

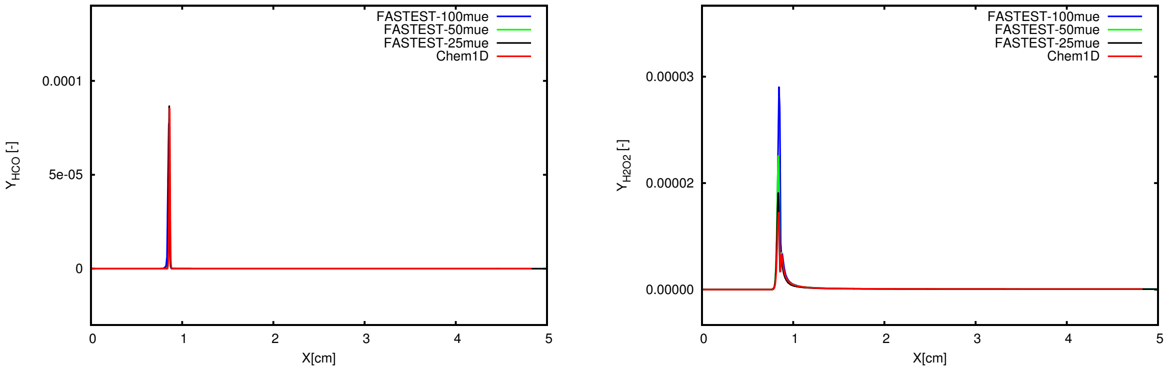

(a) HCO[−]

(b) H2O2[−]

Figure 5.11: The influence of the mesh refinement on the results of short existing intermediates in simulation. The plots represent the mass fractions of HCO and H_2O_2. The length coordinate is given in [cm].

5.1.5 Verification of the burning velocity, adiabatic temperature and transport coefficients, in mixture-averaged formulation

The implementation of mixture-averaged transport coefficients is more complicated and needs more modification of the code compared to the similar case for $Le = 1$ formulation. Beside the requirement to calculate each transport coefficient based on the Hirschfelder approximation, the scalar transport equation which was used to calculate mass fraction has to be changed.

Changing the transport coefficients has direct influence on the computation of laminar burning velocity. While the laminar burning velocity calculated by a stoichiometric methane-air simulation, which is performed using equal diffusion coefficients for all of the species, is approximately equal to $s_l \approx 0.29\,[m/s]$, the mixture-averaged formulation yields $s_l \approx 0.367\,[m/s]$, which is considerably higher. It should also be mentioned that this approximation provides results that do not deviate drastically from the most exact method of calculating transport coefficients, i.e. complex diffusion method, which delivers $s_l \approx 0.371\,[m/s]$.

Here, first the code will be verified for the mixture-averaged formulation, using a stoichiometric methane-air mixture. Then the influence of mixture substances –having lean or rich mixture – on composition will be investigated. At the end of the verification the mesh-sensitivity of the code and its dependence on flow direction will be tested.

5.1.5.1 1-D flamelet for stoichiometric mixture

Once again a $5\,[cm]$ long, one-dimensional geometry, discretized by 512 cells is used. The same method as previous simulation is employed to fix the flame and make a stationary flamelet. Here, the burning velocity is set to $s_l = 0.36749728\,[m/s]$, which is calculated in advance by `Chem1D` for a stationary flamelet and mixture-averaged transport. Since the composition of the mixture is not changed, the adiabatic flame temperature remains the same as the case of unit Lewis number and is equal to $T_{ad} = 2227\,[K]$. The inlet temperature is set to 300 $[K]$.

Calculating the transport coefficients using Hirschfelder approximation makes the simulation a bit more unstable and needs more experience to chose the appropriate time steps. In this simulation as an initial guess the time step is set to 5×10^{-8} $[sec]$.

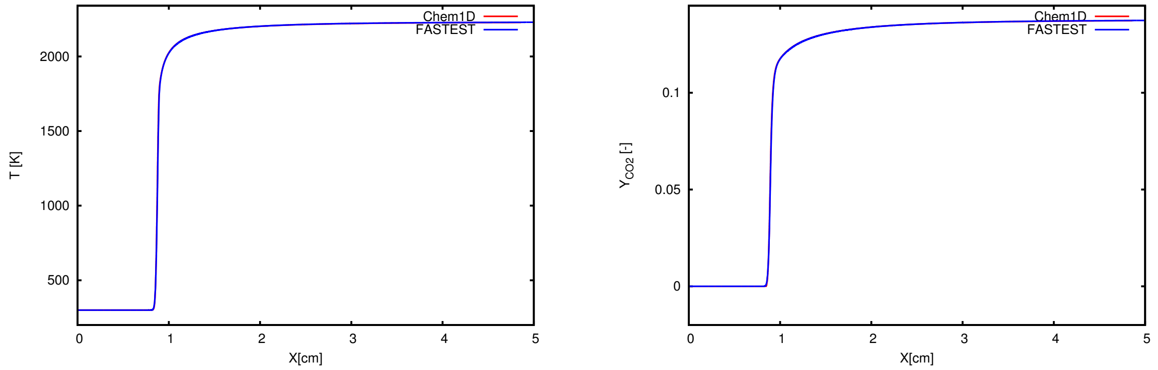

(a) Temperature $[K]$ (b) CO2$[-]$

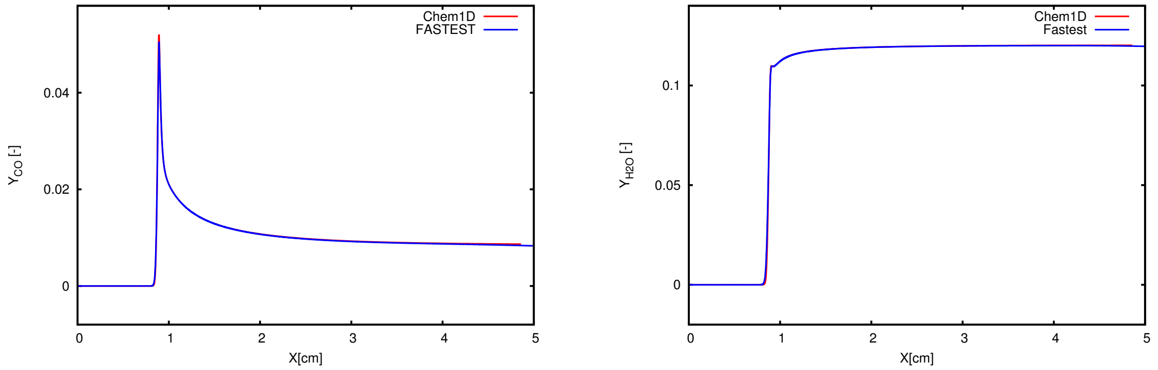

(c) CO$[-]$ (d) H2O$[-]$

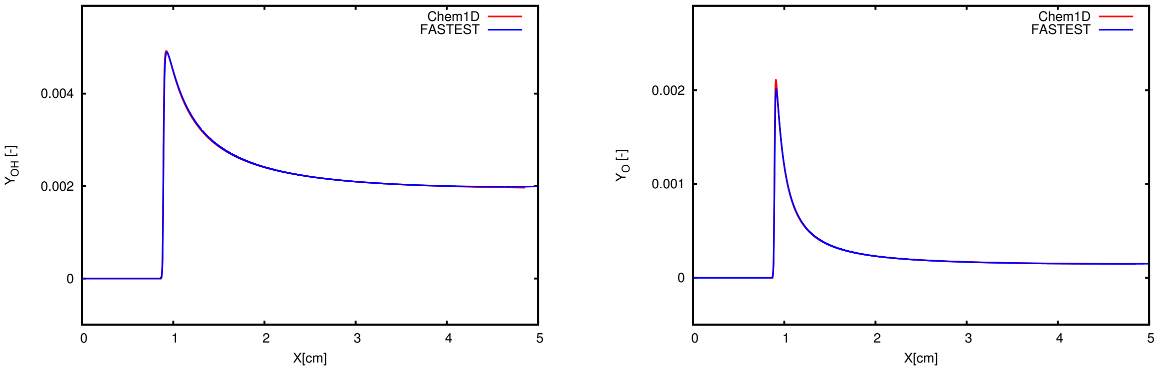

(e) OH$[-]$ (f) O$[-]$

Figure 5.12: Profiles of the temperature and mass fraction in a one-dimensional simulation of stoichiometric methane-air mixture with the transport coefficients calculated with LE=1 formulation-Major species and temperature. The length coordinate is given in [cm]

The results are displayed in figures 5.12 and 5.13. Since the profiles stayed at the position where the flame is initialized, one can say that the laminar burning velocity is computed correctly. The temperature profile is demonstrated in figure 5.12a. One can see that the temperature profile is also predicted correctly and fits to the profile obtained from `Chem1D` across the domain from the inlet to the flame brush and finally to the outlet where it reaches the exact value of the adiabatic flame temperature.

For the sake of simplicity again here the species to be investigated are categorized into three groups of major species, important intermediates, and minor species. The first group of species which will be discussed are the major species CO_2, CO and H_2O. The computed mass fractions of these are shown in figures 5.12b, 5.12c and 5.12d. This group is not too sensitive to the modifications made in calculation of diffusion coefficients. As long as the continuity equations are satisfied in both global and mass fraction forms, they are predicted precisely up to minor discrepancy in the curved line of the flame brush. For this reason, based on the modified transport equation suggested by Hirschfelder and the correct coefficient to calculate the diffusion coefficients, it is expected that the profiles of these three major species are identical to those of `Chem1D`.

Next group of computed mass fractions includes the important radicals like OH, O, H_2, H, CH_3O and CH_3. Their corresponding profiles can be seen in figures 5.12e–5.13d. These species are sensitive to the modification required by mixture-averaged formulation. The correct calculation of their mass fractions has also a big influence on calculating the laminar burning velocity. The profiles calculated by `FASTEST` accurately follow those of `Chem1D`. They fit perfectly in the flame brush and at the outlet where they have to reach the equilibrium state.

The last group of species which has not been discussed yet are the minor species from which HO_2 and HCO are especially interesting. The mass fraction profiles of these two species are illustrated in figures 5.13e and 5.13f. Although the profiles of these species tendentially match the `Chem1D` results, similar to the case of $Le = 1$, there are some discrepancies within the flame brush and at the peaks and the results computed by `FASTEST` do not fit to the curves delivered by `Chem1D`. This deviation may be again due to mesh size which we discuss in next.

5.1.5.2 Influence of the mesh refinement on simulations of mixture-averaged formulation

To investigate the sensitivity to mesh refinement, two other simulations were performed each with cell sizes equal to $50\,[\mu m]$ and $25\,[\mu m]$ respectively. Since the cells are smaller, the time step has to be readjusted and decreased to guarantee convergence. The boundary conditions and the initialization method are the same as the simulation with coarser mesh.

Both simulations converge successfully and fulfill the correct laminar burning velocity. They also yield correct values of mass fractions at the outlet where it is expected to attain equilibrium. The behavior of the flame within the flame brush and the dependency of the maximum value of some minor intermediates on the cell size can still be discussed.

The comparison of the results of these three simulations are demonstrated in figures 5.14a-5.14d. To get a better insight into behavior of the flame within the flame brush in each simulation, the mass fractions are plotted against temperature and not versus length. Four representative species out of 16 species are nominated to be discussed. OH and CH_3 from the important radicals, and HO_2 and HCO from the minor intermediates, which were not computed correctly by the previous simulation. In each figure, the profiles computed

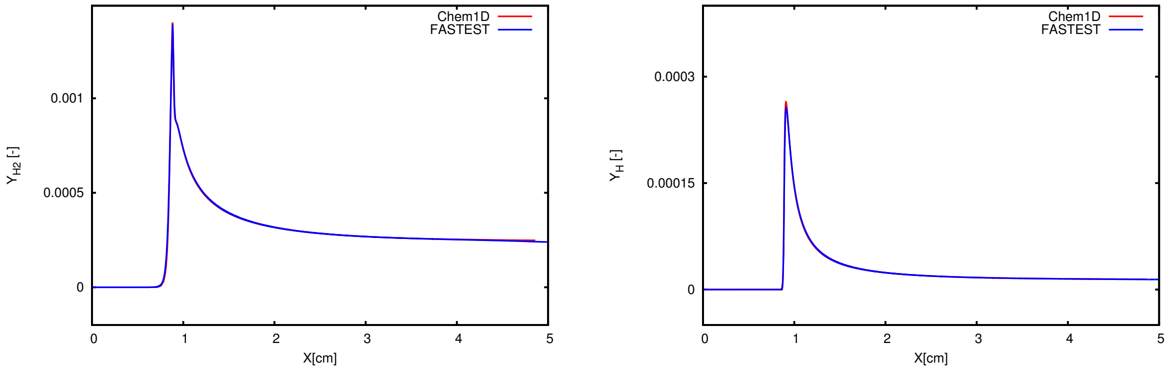

(a) H2 [−] (b) H [−]

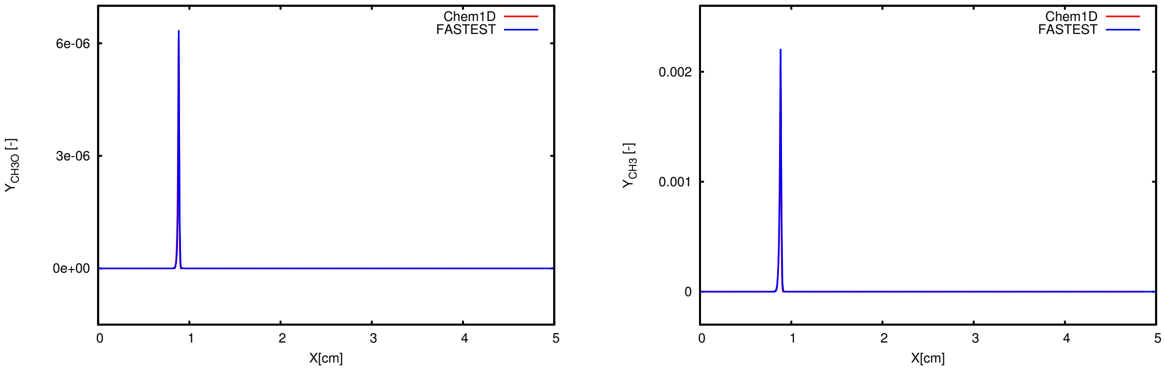

(c) CH3O [−] (d) CH3 [−]

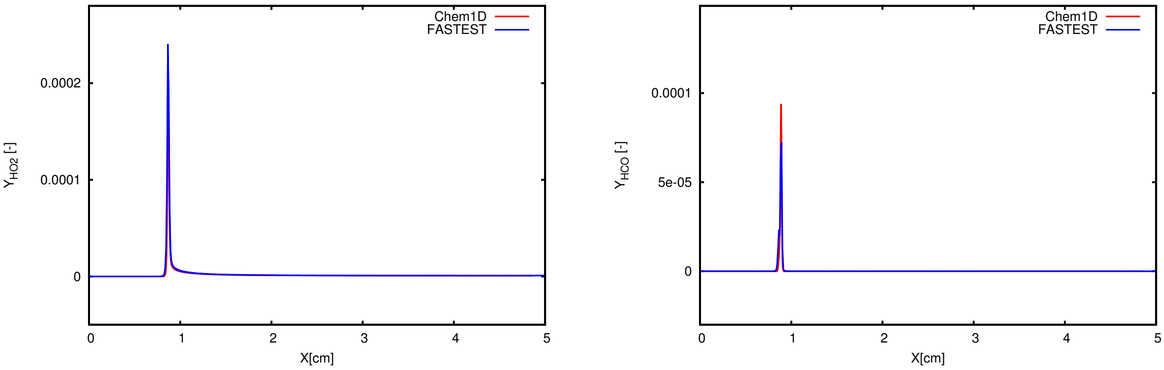

(e) HO2 [−] (f) HCO [−]

Figure 5.13: Profiles of the mass fraction in a one-dimensional simulation of stoichiometric methane-air mixture with the transport coefficients calculated with mixture-averaged formulation-Minor species. The length coordinate is given in [cm]

by Chem1D using mixture-averaged and $Le = 1$ are show as well.

In figure 5.14a the mass fraction profiles of OH are plotted against temperature which provides better understanding of the flame within the flame brush which was not possible in plots over length. As it can be seen, the simulation with the cell size $\Delta x \approx 100\,[\mu m]$ deviates slightly from that of the Chem1D between $T \approx 1500\,[K]$ and $T = 1750\,[K]$. Interestingly, this discrepancy was not present in the plots versus length. As it can be observed, the finer mesh – 50 $[\mu m]$ – gives significantly better profile and the deviation cannot be easily distinguished in the same plot scale. This improvement continues as the mesh is refined to 25 $[\mu m]$, where the profile is identical to the one delivered by `Chem1D` and not even a slight discrepancy can be recognized.

The profile of the simulation with $Le = 1$ is also plotted in figures provide a better understanding of the flame shape using these two formulations to calculate diffusion coefficients. It can be stated that they essentially differ from other four profiles and yield an entirely different flame shape. This behavior can be identified in mass fraction profiles of all other species.

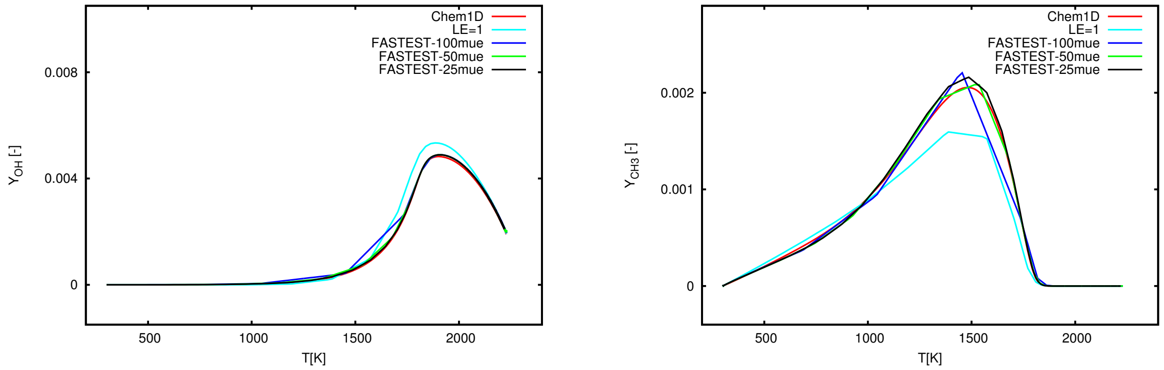

(a) OH [−] (b) CH3 [−]

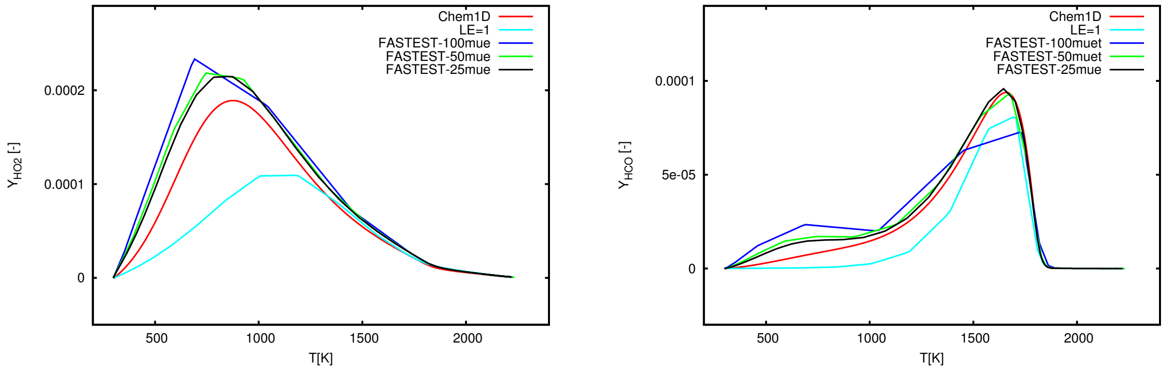

(c) HO2 [−] (d) HCO [−]

Figure 5.14: Comparison of the results performed on meshes with different cell sizes and the results delivered by `Chem1D` for mixture-averaged and Le=1 formulation for transport coefficients. The curves present mass fraction profiles of different groups of species plotted over temperature.The temperature coordinate is given in $[K]$.

Figure 5.14b illustrates the mass fraction profiles of CH_3. CH_3 is an important radical with major influence on the reaction in terms of being the first radical which is produced in the chain start reaction. Needless to say, how different the profile of $Le = 1$ is. Concerning mesh refinement, it is recognized that the profile corresponding to the coarsest mesh size of 100 $[\mu m]$ is not smooth and is angular. This can be a sign that a finer mesh is required. Like the profiles of OH shown in figure 5.14a, CH_3 mass fraction profile using the coarsest mesh, deviates from the results from `Chem1D` especially for temperatures between 1460 $[K]$

and 1750 $[K]$. Similar behavior can be noticed in OH profiles. This behavior improves as the mesh becomes finer. For the mesh size of 50 $[\mu m]$, the profile is still slightly broken especially between $T = 1350\,[K]$ and $T = 1550\,[K]$. Minor discrepancy can be seen, if the mass fraction is plotted versus temperature. The best flame shape is provided by the simulation on the finest mesh. The curve is not broken any more even within the aforementioned temperature intervals, identical to result from Chem1D simulation.

The figure 5.14c provides the best measure for the influence of mesh refinement. It clearly demonstrates, how the mass fraction profiles computed by FASTEST on different mesh sizes get closer to Chem1D results as the mesh is refined. They begin far away from Chem1D profile on the coarsest mesh and are improved gradually with finer mesh. Despite refinement, the profile delivered by simulation on the finest mesh still differs from Chem1D, which may be due to the fact that Chem1D is equipped with mesh adaptivity. This enables Chem1D to refine gradually and continuously and with no limit as gradients grow larger. HO_2 profiles computed by Chem1D show that in the reaction zone, the mesh is downsized to one micrometer which is dramatically finer than the finest mesh in our simulations.

The last species which will be discussed here is HCO, which is another minor species which showed deviation in previous simulation on relatively coarse mesh. The profiles obtained by different meshes can be compared in figure 5.14d. It can be observed that starting from the inlet in the colder zone the mass fraction profile of HCO begins to separate itself from other profiles. This behavior continues through the preheat zone until temperature reaches 1700 $[K]$. This simulation yields again a broken curve which is once more a demand for finer mesh. The other two simulations demonstrate good results from the colder area through the flame and finally at the outlet. All three simulations predict equilibrium accurately, which is expected.

5.1.5.3 Comparing the flame behavior under rich and lean burning conditions

Although the simulations of stoichiometric methane-air mixture resulted in precise mass fractions – especially for reactants, products and major intermediates – the code is not generally verified. To guarantee verification in one-dimensional simulations, the code should be also investigated under lean- and rich burning conditions. In this part the results of simulations performed for lean burning and rich burning methane-air mixtures are illustrated and compared to those obtained by Chem1D. Five representative mass fractions profiles of species are discussed.

LEAN BURNING MIXTURE

In this simulation, a one-dimensional geometry discretized with 4096 cells equal to $\Delta x = 12.5\,[\mu m]$ is used. The inlet temperature is set to 300 $[K]$ and the inlet mass fractions are those of the lean mixture where equivalence ratio is $\phi = 0.8$. To keep the flame in place and make it a stationary flamelet, the inlet velocity is set equal to laminar burning velocity of this mixture, which is provided by Chem1D and is equal to 0.2669 $[m/s]$

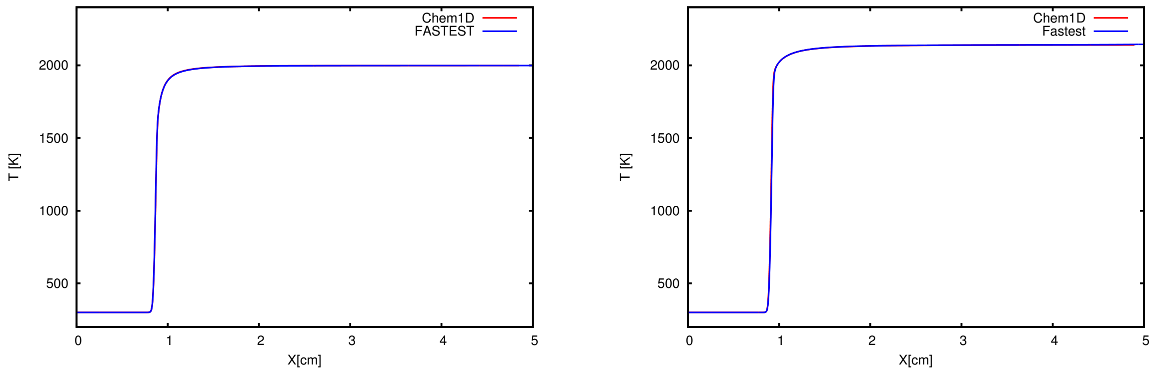

(a) Lean- T[K]

(b) Rich- T[K]

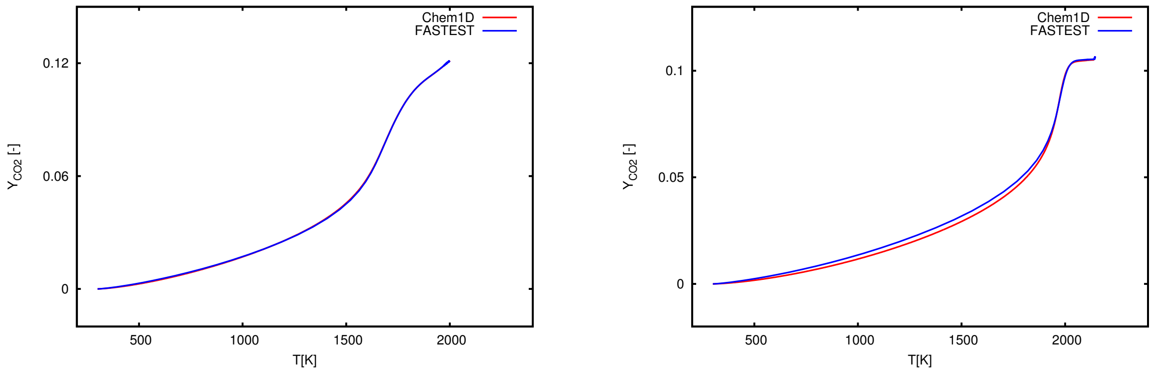

(c) Lean- CO2 $[-]$

(d) Rich- CO2 $[-]$

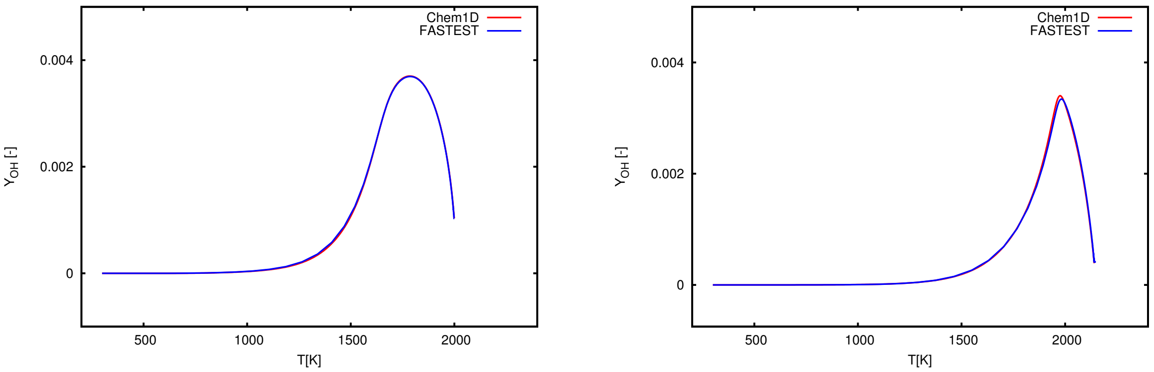

(e) Lean- OH $[-]$

(f) Rich- OH $[-]$

Figure 5.15: Comparison of the lean burning and rich burning methane-air simulation plotted for temperature, CO_2 and OH. The curves present mass fraction profiles of different groups of species plotted over temperature. The temperature coordinate is given in $[K]$.

RICH BURNING MIXTURE

The same geometry and discretization is retained to simulate the rich burning methane-air mixture. This time the equivalence ratio is 20% larger than unity. The burning velocity of the rich mixture is slightly higher than that of the lean mixture and is equal to $s_l = 0.30202582\,[m/s]$.

Both simulations were able to predict the laminar burning velocity precisely and produce a stationary flamelet. The results of these simulations are shown in figures 5.15 and 5.16. On the right side, the profiles of the rich burning combustion are demonstrated and on the left side the mass fractions of the same species are shown.

The temperature profiles are shown in figures 5.15a and 5.15b. Both lean burning and rich burning profiles are identical to those of `Chem1D` where they begin from 300 $[K]$ in pre-

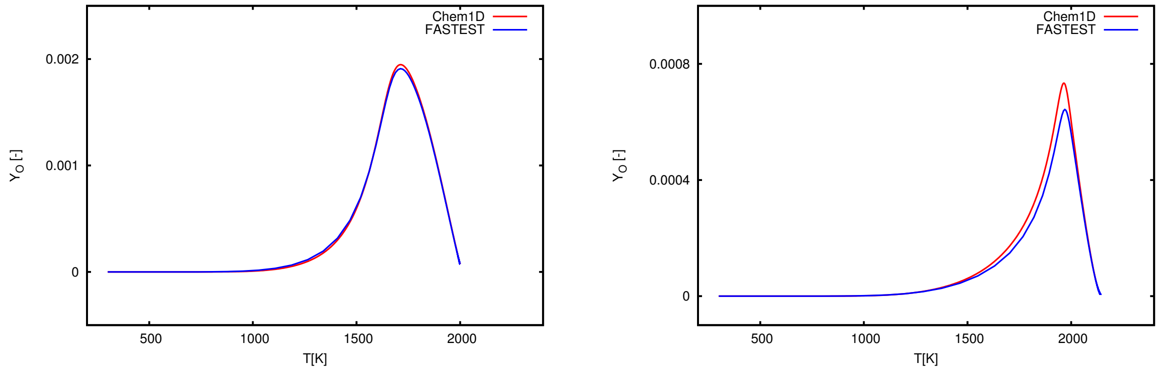

(a) Lean- O $[-]$

(b) Rich- O $[-]$

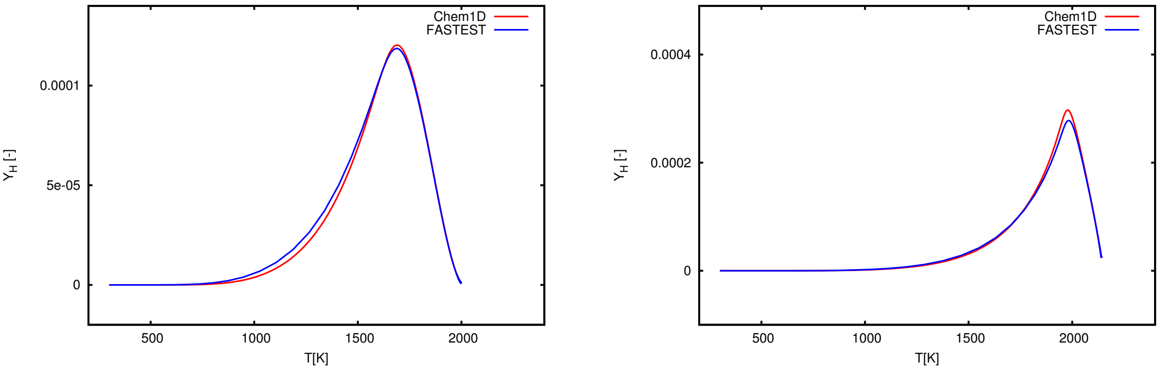

(c) Lean- H $[-]$

(d) Rich- H $[-]$

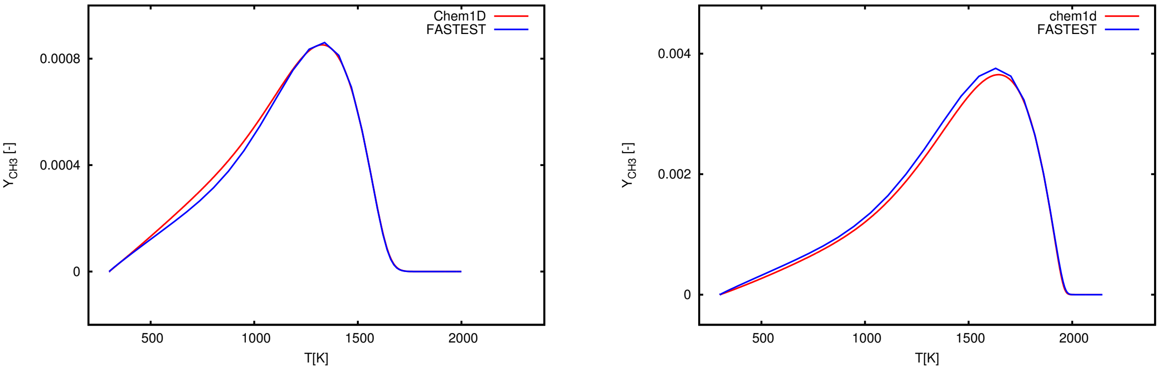

(e) Lean- CH3 $[-]$

(f) Rich- CH3 $[-]$

Figure 5.16: Comparison of the lean burning and rich burning methane-air simulation plotted for H, CH_3 and O. The curves present mass fraction profiles of different groups of species plotted over temperature.The temperature coordinate is given in $[K]$.

heat zone and increase through the flame brush and reach the adiabatic flame temperature equal to $T_{ad} = 2000\,[K]$, for the lean mixture, and $T_{ad} = 2140\,[K]$ if the equivalence ratio is equal $\phi = 1.2$.

In figures 5.15c and 5.15d, the mass fraction of the CO_2 is plotted against temperature. In figure 5.15c, both simulations provide very accurate predictions. From the inlet where mass fraction equals zero all the way to equilibrium state, the curve coincides with the profile produced by `Chem1D`. This proves the correctness of the result concerning the equilibrium state and transport phenomena. On the right side, the profile shows acceptabe accuracy in simulating rich combustion. The curves in preheat zone and the product zone are almost identical to `Chem1D` results, albeit there is negligible discrepancy in the reaction zone. Generally speaking, the reactants and major species like H_2O and CO_2 can be predicted with high accuracy in lean, stoichiometric and rich combustion regimes.

In figure 5.15e, the mass fraction of OH is plotted versus temperature. From the cold inlet zone until the hot production zone, accurate prediction of the mass fraction can be observed. This behavior can be seen in 5.15f, where similar profiles are plotted for rich combustion, except for temperatures between $1950\,[K]$ and $2050\,[K]$ where minor deviation can be seen.

Among major intermediates, O radicals are discussed here. The the lean combustion regime profile on the right side, 5.16a, demonstrates very good agreement with the `Chem1D` results in all three combustion zones. Contrary to lean combustion regime, the resulting O-profile for the rich regime deviates from `Chem1D` curve after the temperature reaches $1600\,[K]$. Despite minor difference, it continues until $T = 2000\,[K]$. The discrepancy is highest where mass fraction reaches its maximum. After this temperature, toward the equilibrium state, both profiles converge to each other.

From smaller and minor species, the H radicals and CH_3 are demonstrated below in figures 5.16c–5.16f. The H radicals have been predicted for rich combustion regime precisely, except at the maximum where temperature is around $2000\,[K]$. For lean combustion, in the reaction zone, it is slightly overestimated until the temperature goes up to $1500\,[K]$. This minor deviation is acceptable considering that H radicals are present everywhere, even at the end of the reaction zone. The last species is CH_3 which is illustrated in figures 5.16e and 5.16f. As indicated for the stoichiometric combustion, the CH_3 radicals are minor species which are relatively sensitive to mesh refinement and difficult to be predicted correctly. Here again, both for rich and lean regimes, some discrepancies can be observed. In both figures the profiles diverge from the curve delivered by `Chem1D` and converge again when temperature reached $1600\,[K]$. Interestingly for the lean regime, this radical is underpredicted whereas in the rich regime it is overpredicted.

5.2 2D Verification

So far we have verified the implemented formulation for transport equations, molecular and thermal diffusion, and all the factors that can influence burning velocity, mass fractions over the whole domain, flame shape, adiabatic flame temperature and so on. Having verified one-dimensional configurations, the code is ready to be verified in multi-dimensions. The whole procedure should be repeated and the results must be the same in all dimensions for the same boundary and initial conditions. In a two-dimensional configuration, for example, alongside the laminar burning velocity and the adiabatic flame temperature, other features of the premixed flame like flame cooling and stretch and curvature (which do not reveal themselves in one-dimension) can be observed and investigated. The test case will be extensively described in the sequel.

5.2.1 2D burner-stabilized laminar premixed flame

For two-dimensional verification the test case simulated by Somers (1994) [112] and later also by van Oijen (2001) is used. The configuration consists of a lean methane-air mixture with an equivalence ratio of $\phi = 0.9$ in a slot burner within a box. In figure 5.17 the computational domain is demonstrated. As it can be seen, all possible boundary conditions which are available in `FASTEST` are used in this configuration. The width of the slot is $6\,[mm]$ and that of the box is $24\,[mm]$.

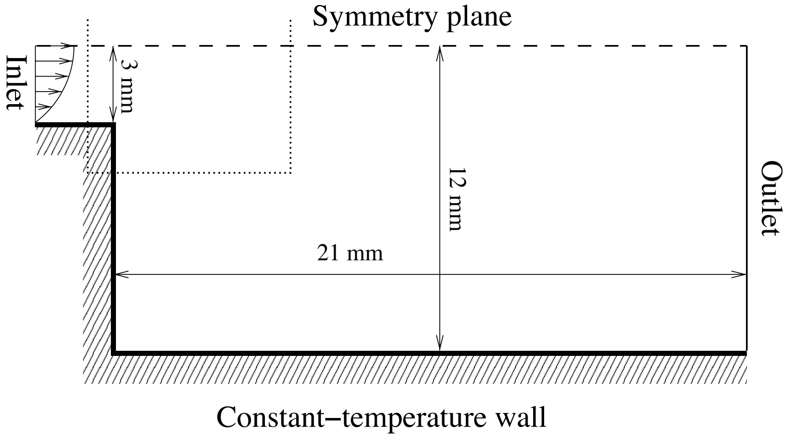

Figure 5.17: Numerical configuration of the two-dimensional slot burner in the box used for multi-dimensional verification

The whole configuration simulated by van Oijen is $24[mm]$ long. The temperature at the walls are assumed constant and equal to $T_w = 300\,[K]$. The inlet velocity is represented by a parabolic profile with the maximum velocity of $V_{max} = 1.0\,[m/s]$. To be able to catch the correct laminar burning velocity, which has direct influence on the flame angle and the correct mass fractions, the cell sizes are set to be $20\,[\mu m]$, using the information obtained by previous one-dimensional simulations. The simulation by Somers has a non-uniform mesh which becomes gradually coarser farther from the flame center (in the positive X direction on the figures at the right).

Another issue about this test case is the calculation of transport coefficients. Contrary to `FASTEST`, which uses the mixture-averaged formulation for transport coefficients, an alternative method is utilized where different Lewis numbers for each species are used to calculate the diffusion coefficients. This can theoretically result in differences in flame shape and also can yield slightly different burning velocity.

The isolines of temperature and the mass fractions of OH and H_2 are demonstrated in figures 5.19a–5.19c, and those of O, H and HO_2 are plotted in figures 5.20a–5.20c. The temperature will be discussed first. The isolines of temperature, as it can be seen in figure 5.19a, are in very good compliance with the results obtained by Somers. The isolines are exactly

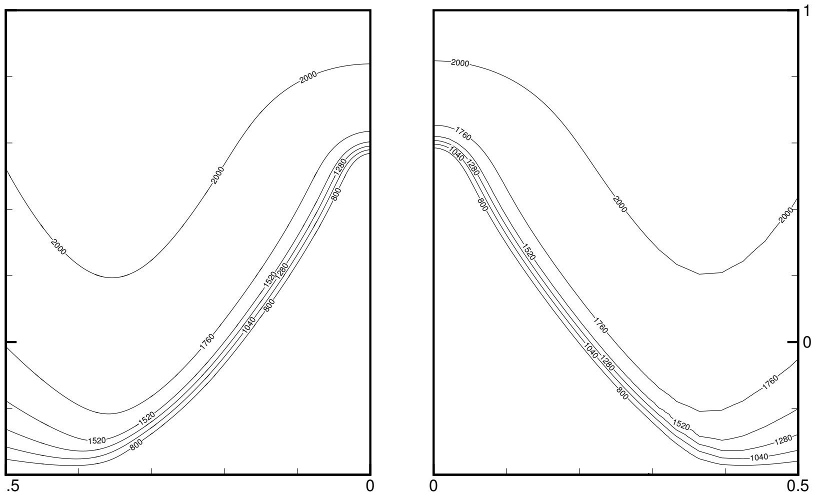

Figure 5.18: Contours of the HCO mass fraction computed by FASTEST, one the left side, verification test case, one the right side.

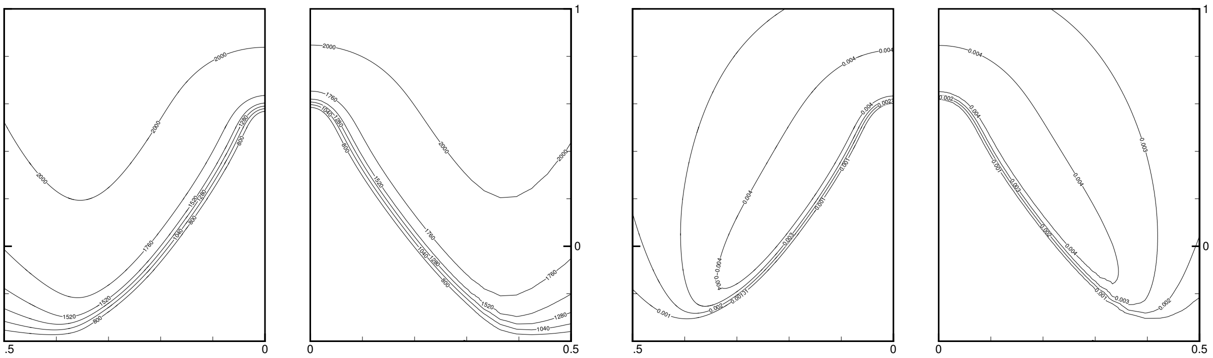

(a) T[K]

(b) OH [−]

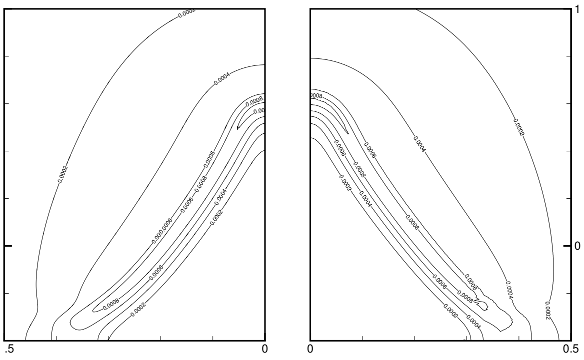

(c) H2 [−]

Figure 5.19: Comparison of the iso-contours of temperature and OH and H2 of 2D-burner stabilized laminar premixed slit-burner resulted from FASTEST(left) and van Oijen(right).The contours are drawn at equal intervals covering the entire range of each variable. The same iso-levels are used for FASTEST-3D and van Oijen diagrams. The space coordinates are given in cm.

symmetric to each other and the contour lines arena one-to-one correspondence. Similar to one-dimensional cases calculation of temperature should not have large discrepancy within the main part of the plot i.e. $X < 0.4\,[cm]$.

Mass fractions of the species are also in perfect agreement with those computed by

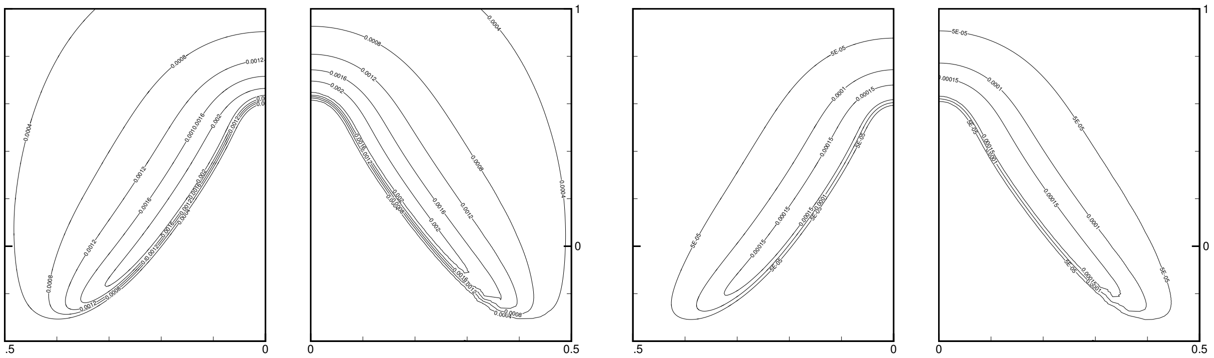

(a) O [–]

(b) H [–]

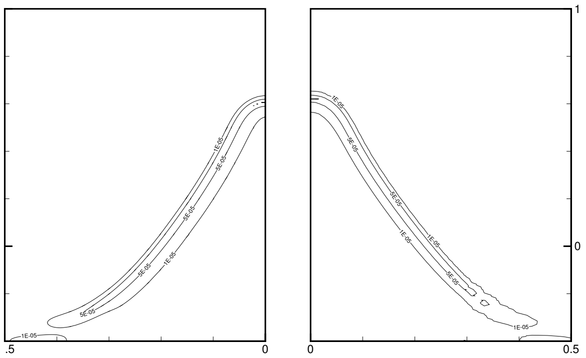

(c) HO2 [–]

Figure 5.20: Comparison of the iso-contours of O and H and HO2 of 2D-burner stabilized laminar premixed slit-burner resulted from FASTEST(left) and van Oijen(right)The contours are drawn at equal intervals covering the entire range of each variable. The same iso-levels are used for FASTEST-3D and van Oijen diagrams. The space coordinates are given in cm.

Somers. The flame tips, where the curvature has influence, are in good agreement in all species even in minor ones like HO_2 . The isolines of mass fractions within the flame cone and in the flame cooling zone are both successfully predicted (see for instance the isoline of H_2). The absolute value of the contours also confirm this verification.

There are two problems to be discussed. First, the flame tips on the right side is slightly higher than the left side – it is less than $0.05\,[mm]$. This could be the consequence of using different methods of calculation for diffusion coefficients which causes a minor difference in flame shapes and also in laminar burning velocity. Second, there are discrepancies in mass fractions and temperature isolines where $X > 0.4\,[cm]$. This is definitely the consequence of using very coarse mesh in that area where nonuniform and gradually increasing cell size was used by Somers (right side). This apparently has delivered broken curves which can be the source of the inaccuracy in that area.

5.3 Conclusion

The verification procedure is summarized in table 5.1. A detailed chemistry solver was coupled to FASTEST-3D to compute multi-component reaction rates of the species in transport equations. The mass and energy transport equations were changed according Hirschfelder approximation for mixture-averaged coefficients. The Hirschfelder approximation for computing diffusion coefficients, thermal conductivity, viscosity and thermal diffusion coefficient was implemented.

To verify these implementations, first the source terms were compared to those calculated by `SENKIN`. This step showed very good agreement between the two codes and confirmed the verification. Then the diffusion and convective terms were checked whether they make sense physically. The next step was verification of the burning velocity, adiabatic temperature and transport coefficients based on $Le = 1$ formulations. This step also showed exactitude of the implementation albeit there were minor deviations in computing the short existing species where the mesh was very coarse ($\Delta x \approx 0.1$).

The previous step was repeated to verify the implementation of mixture-averaged formulation. This step also gave accurate and even nearly perfect results and showed the implementations to be correct. The burning velocity and the flame shape were captured very well although, again here, there were some discrepancies in calculation of the minor species.

To Check other features that influence premixed flames, a two-dimensional case was simulated. This confirmed the correctness of the implementation once again, where other issues like flame cooling (at stabilization point), curvature, prediction of the flame cone and flame length are concerned.

Test Case	Compared with	S_l	Verified	Comment
Reaction rate	`SENKIN`	-	✓	PFR vs PSR, methane-air, Hydrogen-air
Diffusion term	-	-	✓	Mixture average
Convective term	-	-	✓	Testing convection velocity, LE=1, Mix. avg.
1D, LE=1	`Chem1D`	✓	✓	Stoichiometric methane-air, $\Delta X < 100\mu$
1D, Mix. avg.	`Chem1D`	✓	✓	$\Delta X \leqslant 25\mu$
1D, Mix. avg. in X,Y,Z direction	`Chem1D`	✓	✓	$\Delta X \leqslant 25\mu$
Mix. avg. lean, rich	`Chem1D`	✓	✓	$\Delta X \leqslant 20\mu$
2D Slot burner in box	van Oijen(2001)	✓	✓	$\Delta X = 25\mu$

Table 5.1: Summary of verification test cases.

Chapter 6

Stratified flames

6.1 Basic of tabulated detailed chemistry for combustion

At current state of combustion research, the flamelet generated manifold (FGM) is considered to be one of the forefronts in large eddy simulation of combustion devices such as swirl burners, internal combustion engines, furnaces, and so on. This simulation method of reacting flows has been verified and validated in a variety of cases. The basic idea of the method is to generate a look-up table from simulations of one-dimensional laminar premixed flames which are obtained by flamelet generators equipped with multi-component chemistry mechanism and complex transport coefficients.

Related results have been reported by van Oijen and de Goey in 2000 [92] and by van Oijen in 2001 [119] and in 2002 [120]. He verified the mthod in a 2-dimensional case in comparison with a direct numerical simulation utilizing detailed chemistry. The basic idea here is that, corresponding to each point of the simulation domain with the composition $Y_k = Y_k(x)$, there exists a point in the so called composition space. In other words, each point of the physical space has a solution which is a trajectory in the composition space. As an example, the way a manifold is generated and incorporated into CFD is described below.

In this method the *premixed flamelet* is assumed to be a region where *reaction progress variable* Y increases gradually from zero to its equilibrium value far behind the flame. The reaction progress variable is chosen to be

$$Y_{PV} = \sum_{k=1}^{N} b_k Y_k(x)\,, \tag{6.1}$$

which can be any linear combination of the species mass fractions, where b_k is the weighting factor of the species k. This is usually normalized with respect to the equivalent value Y_{eq} which is calculated through

$$Y_{eq} = \sum_{k=1}^{N} b_k Y_{k,eq} \tag{6.2}$$

$$Y_{n,pv} = \frac{Y}{Y_{eq}}\,, \tag{6.3}$$

where $Y_{n,pv}$ is the normalized progress variable and has a value within the interval $[0, 1]$. The solution ψ_i for the one-dimensional flamelet can be mapped uniquely from physical space into reaction progress variable space if Y is chosen properly. Presented in compact mathematical notation is

$$\psi_i \longmapsto \psi(Y)\,. \tag{6.4}$$

This mapping becomes complete after introducing a control variable ξ. As the name suggests, in any flamelet mixture, ξ remains constant for each specific flamelet and is independent of the reaction progress variable. The mapping procedure is carried out to condition the mixture fractions of the unburnt mixture to be kept within flammability limits. For rich or lean regions too far from the stoichiometric condition, which are assumed to exceed flammability, the table will be extended using linear extrapolation. Figure 6.1 demonstrates an example of a flamelet generated manifold in terms of two variables, namely the reaction progress variable and the mixture fraction, calculated for methane-air combustion at a pressure equal to 1 $[bar]$.

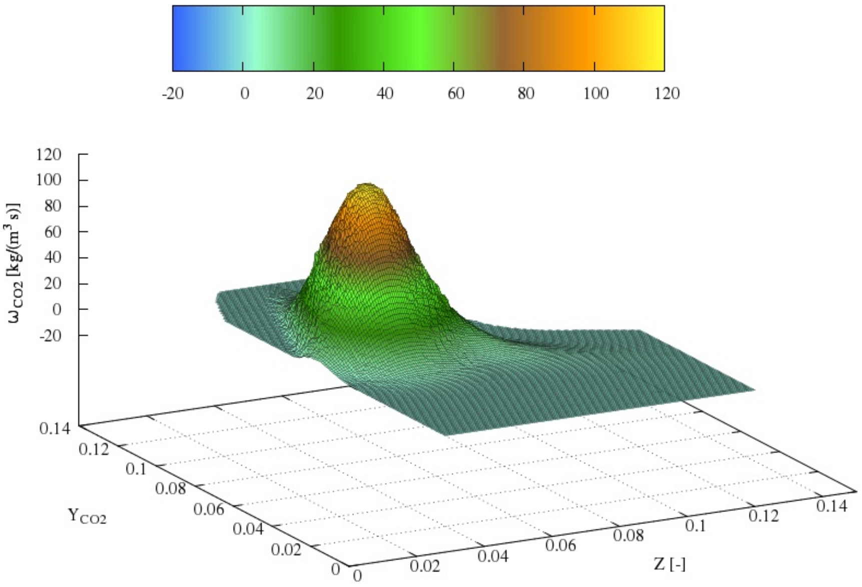

Figure 6.1: Manifold of a methane-air flame defined by two controlling variables showing the source term of carbon dioxide $[kg/m^3s]$ colored with the temperature $[K]$.

In computational fluid dynamics, the flamelet generate manifold is coupled with two additional transport equations, one for the reaction progress variable as

$$\frac{\partial \rho Y}{\partial t} + \frac{\partial}{\partial x_i}(\rho u_i Y) = \frac{\partial}{\partial x_i}\left(\rho D \frac{\partial Y}{\partial x_i}\right) + \dot{\omega}_Y\,, \tag{6.5}$$

where the $\dot{\omega}_Y$ is the source term calculated analogous to Y in equation (6.1)

$$\dot{\omega}_Y = \sum_{k=1}^{N} b_k \dot{\omega}_k\,. \tag{6.6}$$

And the second transport equation in terms of mixture fraction is similar to (6.5). After solving the two transport equations, one can use the manifold as a lookup table and extract the other corresponding variables. Thus, corresponding to each point of the 3-dimensional physical space, there is one point in the flamelet generated manifold, in which other information of a related one-dimensional flamelet, namely the mixture fraction and the reaction progress variable, is stored.

6.2 Stratified flames

The just presented method can reasonably simulate different kinds of diffusion as well as fully premixed flames. The question is, however, what happens if the flame is stratified like that of unconfined premixed flame?

As was explained, this method is based on the assumption that in a multi-dimensional domain, for each specific mixture fraction the required information for simulation can be obtained from a lookup table (FGM) which is generated by assembling numerous one-dimensional flamelets. To check the validity of this assumption, we define a new mixture fraction which does not change along one dimensional flamelets. Since the mass conserved in these simulations, the mixture fraction can be defined roughly based on the sum of atomic mass fractions of carbon and hydrogen. Note that the species convert to each other but does not vanish. Therefore

$$Y_C = \sum_{1}^{N} = \frac{a_{Ck} W_C}{W_k}\,, \tag{6.7}$$

$$Y_H = \sum_{1}^{N} = \frac{a_{Hk} W_K}{W_k}\,, \tag{6.8}$$

$$f = Y_C + Y_H\,. \tag{6.9}$$

Herein Y_C and Y_H are the elemental mass fractions of the atomic carbon and atomic hydrogen, while W_C and W_H are atomic mass of the species C and H. Finally a_{Ck} and a_{Hk} are the number of the carbon and hydrogen atoms in the species k respectively. Based on these formulations, we can define the variable Φ, assuming $f = 0.055$ for a stoichiometric mixture

$$\Phi = \left(\frac{f}{1-f}\right)\left(\frac{1-0.055}{0.055}\right). \tag{6.10}$$

6.2.1 Application in stratified flames

Five different 1-dimensional simulations for different premixed laminar burning mixtures were performed each of which corresponds to a unique value of Φ, ranging from very lean but still flammable to nearly stoichiometric mixture. They are related to Φ equal to 0.5, 0.6, 0.7, 0.75, 0.8, and 0.9.

In the next step, a two-dimensional DNS with multi-component chemistry is performed across a domain spanning $5\,[mm]$ along the Y-axis and $10\,[mm]$ along the X-axis. This domain is designated as the “1st-Domain”. The flow is directed from left to right. At the inlet, Φ is defined with a ramp gradient function which changes linearly from $\Phi = 0.55$ at $Y = -2.5\,[mm]$ to $\Phi = 0.95$ at $Y = 2.5\,[mm]$. Since this gradient causes varying laminar burning velocities, in order to maintain a nearly straight flame around the midpoint of the domain, the inlet flow velocity assumed to be approximately equal to s_l of the mixture at several Y coordinates. This is just an approximation because in such a stratified flame, the burning velocity is not known pointwise in advance. Therefore the laminar burning velocity of the 1-D case has to be calculated before commencing the two-dimensional simulation. It is already known that the mixture fraction increases monotonically with respect to burning velocity [101], and their dependence can be approximated linearly considering $0.5 < \Phi < 0.95$. This is not an erroneous approximation, since the linear velocity gradient at the inlet has barely any decisive influence on the final solution and it only helps to stabilize the flame around the center. One has to make sure that the symmetry boundary condition is set at the upper and the lower boundaries along $Y = \pm 2.5 [mm]$.

The flame is initialized the same way as in the one-dimensional flamelet using hyperbolic tangent. We provide a cold mixture at the inlet with $T = 300\,[K]$ and a hot mixture at the outlet where temperature reaches its peak, viz. the adiabatic flame temperature of stoichiometric methane-air mixture which is equal to $T = 2227\,[K]$. The transport coefficients are calculated using the Le $=$ 1 formulation. With all these ingredients, a premixed stratified laminar burning flame is modeled using a 2-D geometry.

Two further simulations are carried out on two domains with half and quarter the height (i.e. in Y-direction) of the 1st-Domain, respectively. These two geometries are accordingly called the "2nd-Domain" and the "3rd-Domain". To run the simulation on these two domains, everything kept unchanged compared to the 1st-Domain except the inlet mixture fractions. Again here a linear function defines the Φ between the values $\Phi(Y_{min}) = 0.5$ and $\Phi(Y_{max}) = 0.95$. Reducing of the height while keeping Φ unchanged makes the gradient steeper compared to that of the 1st-Domain. Then the 3rd-Domain possesses the steepest gradient and has, therefore, the most stratified flame. The results are illustrated in figure 6.2. The contours in these figures present the development of the mixture fraction, Φ along the flow.

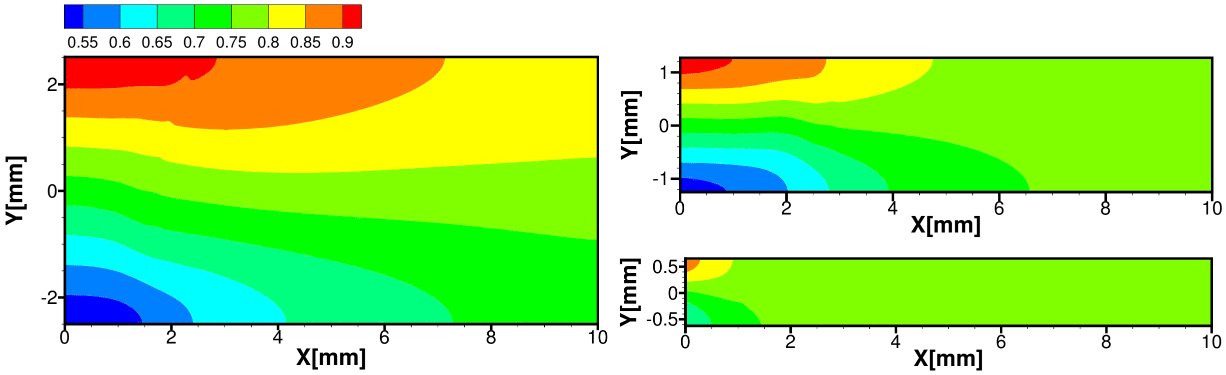

Figure 6.2: Contour plots demonstrate development of mixture fraction $\Phi[-]$ across the flame for **(left)** the 1st-, **(upper-right)** the 2nd-, and **(lower-right)** the 3rd-Domain. Results are obtained from 2D-simulations of the premixed stratified laminar burning flames. The gas mixture flows from left to right.

For instance, one can extract the data along isolines of mixture fractions at $\Phi = 0.75$, and plot the source term of CO_2 versus its mass fraction and then compare it to the same plot for corresponding mixture fraction obtained from one-dimensional simulations. Figure 6.3(a) presents the CO_2 source term plotted versus its mass fraction along the $\Phi = 0.75$ isoline in all three simulations compared to the flamelet corresponding to $\Phi = 0.75$. As can be seen, the three curves almost coincide from inlet, where there is no carbon dioxide, all the way to outlet, where carbon dioxide reaches its maximum i.e. equilibrium. Note that these flames operate under different stratification. Moreover, all the plots obtained from stratified flames overlay the curve obtained from the flamelet corresponding to $\Phi = 0.75$. This reinforces the aforementioned assumptions.

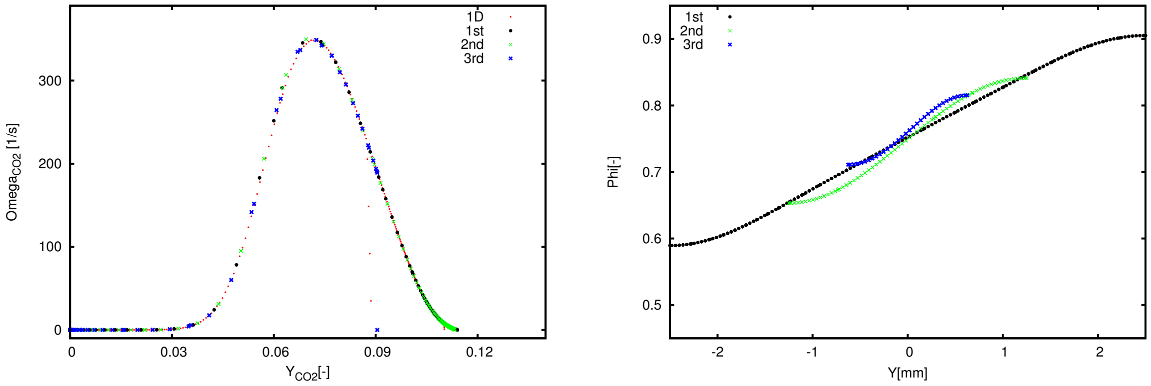

(a)

(b)

Figure 6.3: **(a)** Source term of carbon dioxide $\omega_{\mathrm{CO2}}\,[1/s]$, versus its mass fraction $Y_{CO2}[-]$, plotted for 1-D flamelet with mixture fraction equal to 0.75 over the 2-D domain along the $\Phi = 0.75[-]$ isoline. **(b)** Gradient of mixture fraction $\Phi[-]$ along the flame vertical to the flow direction versus location along $Y\,[mm]$.

To better understand the influence of the stratification steepness, the mixture fraction Φ is extracted along the flame and is plotted versus $Y\,[mm]$ in figure 6.3.b for all three domain sizes. The three curves are not equally straight, since the span of the domains were different. Roughly speaking, however, one can say that in all three domains the slope of the mixture fraction along the flame is close to $[0.1/1\,[mm]]$. The deviation seems grow, as the domain becomes wider.

The behavior of the stratified flame is examined by repeating the simulation under stronger stratification, which is implemented by setting the inlet mixture fraction to have an abrupt jump. The results are shown in the figure 6.4. Three different functions have been used to stratify the flame. The first function was a hyperbolic tangent with a gradual gradient in Y-direction. The next function was also a hyperbolic tangent but this time with a steeper gradient. Finally, the third function was a step function, to represent an abrupt change in Y-direction which stands as the strongest case of stratification. Contrary to the previous simulation, combustion of mixtures was triggered using two hot burnt co-flows positioned at $|Y| > 2.5[mm]$. The velocities of co-flows were set equal to $1\,[m/s]$. The main flow was divided into two segments. In the first segment at $Y < 0$, the mixture fraction was set to $\Phi = 0.5$ at the inlet, and in the second segment $\Phi = 0.95$. The flow runs from left to right with equal velocities for the two mixture fractions, which is lower than the velocity of the co-flows i.e., $u_{in} \approx 0.375$. The development of mass fraction, mixture fraction, and temperature on the domain is demonstrated in figures 6.4.a–c. These figures correspond

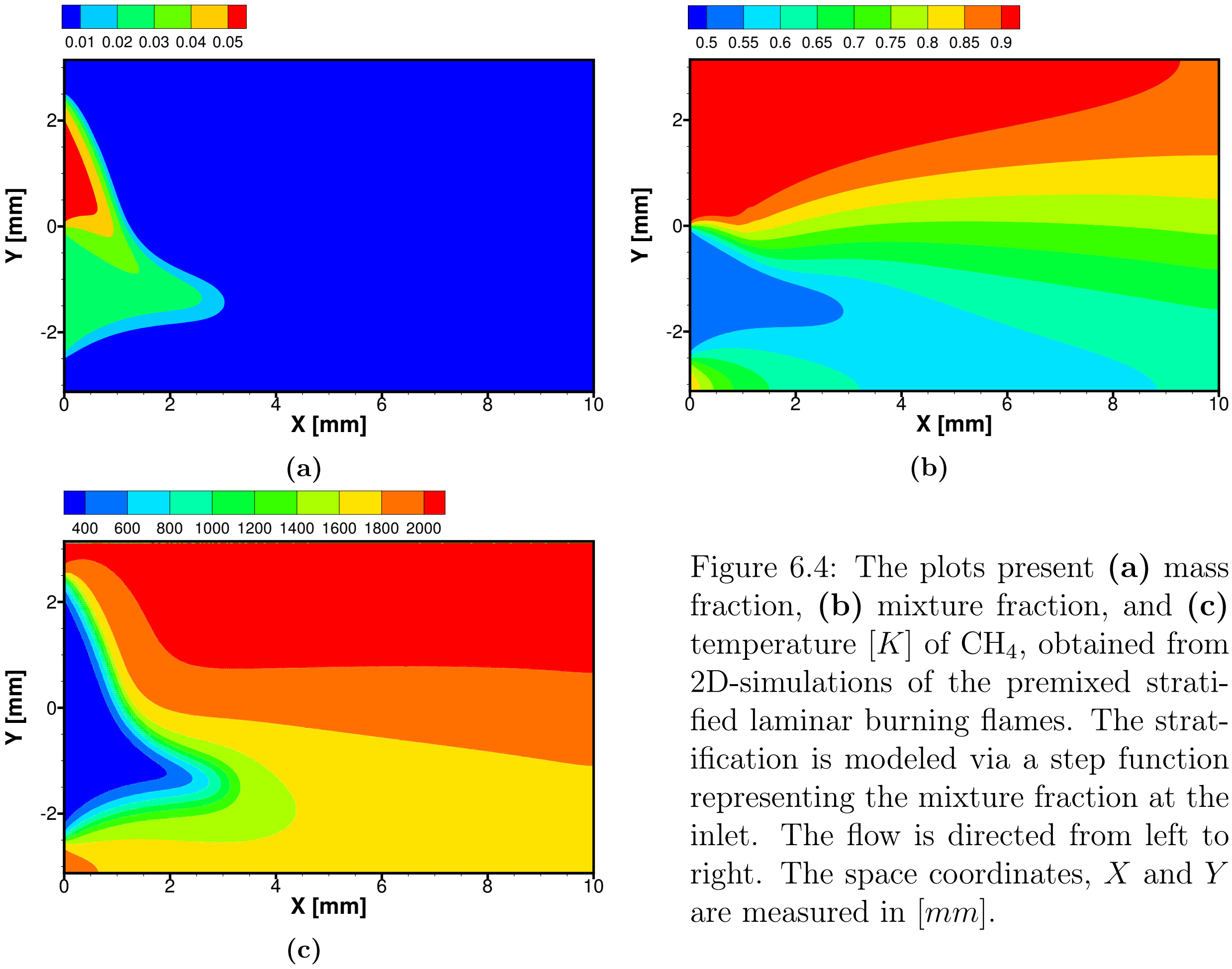

(a)

(b)

(c)

Figure 6.4: The plots present **(a)** mass fraction, **(b)** mixture fraction, and **(c)** temperature $[K]$ of CH_4, obtained from 2D-simulations of the premixed stratified laminar burning flames. The stratification is modeled via a step function representing the mixture fraction at the inlet. The flow is directed from left to right. The space coordinates, X and Y are measured in $[mm]$.

to the strong case of stratification, i.e. step function. Due to similarity of results, the contour plots of the other two simulations are not shown here. It can be observed that the stratification led to an asymmetric contour around the centerline. In fact all other variables, which are not presented here, demonstrate the same asymmetric contour plot.

As explained and illustrated earlier, the data can be extracted along any isoline $\Phi =$ `const`. Figure 6.5 demonstrates the source term of carbon dioxide plotted against mass fraction of CO_2. As can be seen, despite different levels of stratification, the plots of all 2-dimensional simulations are identical, all the way from inlet to outlet. This confirms that the level of stratification does not affect variables, for instance the amount of CO_2 produced, corresponding to a specific mixture fraction. On the right side of the diagram there is a second curve which is due to the co-flows. The co-flows might have the same amount of source term of carbon dioxide, when they mix with the main flow. This need not necessarily be taken into account and is safely ignored. For this, one would need to adjust the mixture fraction of each burnt co-flow to the adjacent main-flow.

The most interesting point about this figure is revealed in comparison to the flamelet. Contrary to the strong stratification with the ramp function, the curves here which are obtained from 2-D simulations along $\Phi = 0.75$, do not coincide with the one coming from one-dimensional simulation. Although they are identical when CO_2 reaches its maximum at the outlet, where the source term becomes zero and mass fraction Y_{CO_2} reaches equilibrium,

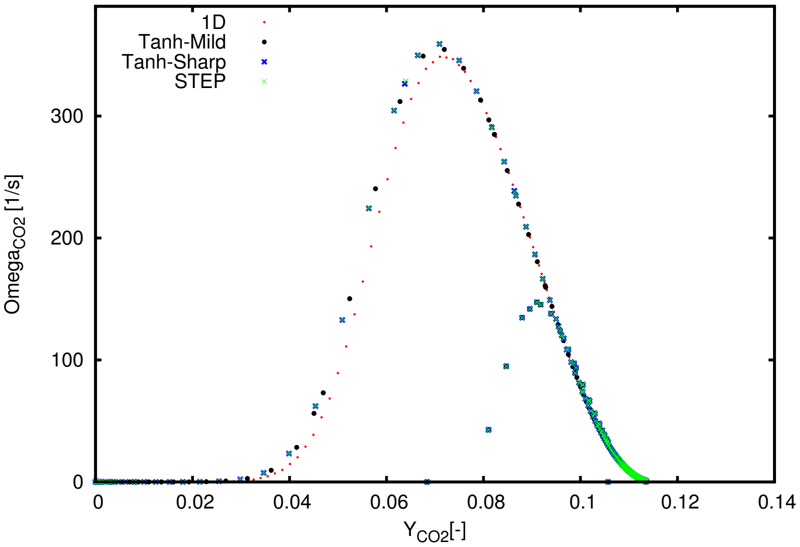

Figure 6.5: Source term of carbon dioxide, $\omega_{CO2}[1/s]$ over $Y_{CO2}[-]$, mass fraction of carbon dioxide plotted for 1-D flamelet with mixture fraction equal to 0.75 and for the 2-D domains having different stratification function along the isoline of $\Phi = 0.75[-]$.

they deviate from each other when the mixture enters the preheat zone and the source term is non-zero. In the preheat zone before the source term reaches its maximum, the flamelet deviates from 2-dimensional results and demonstrates lower value of the source term. This behavior is the same for all other choices of mixture fraction.

Although the deviation is not very large here, this already suggests that using a lookup table obtained from 1-dimensional flames (flamelets) may not be precise enough when it comes to very sharp stratifications. Therefore the behavior of the stratified flames is to be investigated for various cases, from very lean flows close flammability limits to very rich mixtures, and also from laminar to turbulent flows with high turbulence intensity in order to validate the aforementioned assumptions on the methods based on flamelet generated manifolds.

Chapter 7

Flame-Wall Interaction

One of the longstanding research topics in the subject area of combustion is flame-wall interaction. There is now consensus among the workers of the field that combustion pollutants go hand in hand with combustion inefficiency. Although flame and wall do not interact everywhere in the combustion device, their interaction has always a significant influence on the combustion process especially in terms of unwanted byproducts such as unburnt hydrocarbons and NO_x [29].

There is nowadays an accelerating trend toward more compact designs of combustion devices. The inherent effect of smaller geometry of these devices is apparently a larger ratio of surface area to volume of the device. This is synonymous to a higher impact of the walls on combustion processes taking place within the device, or simply put, an even more marked flame-wall interaction. So, the *downsizing* trend makes this topic ever more relevant from an applied fluid dynamics research viewpoint.

There are numerous phenomenon pertaining to flame-wall interaction. These interactions fall under one of two categories, namely thermal interactions or thermochemical interactions. One of the more important questions regarding combustion devices is the heat flux from the flame toward the wall. Since the adiabatic flame temperatures normally exceed the allowable temperatures, restricted by thermal and thermomechanical strength of construction material, there has to be a cooling system responsible for the task of carrying the excess heat across the walls to the surroundings. This heat exchange between wall and flame within thermal boundary layers and its influence on combustion deserves special attention. As we can see, the application very well motivates our research toward a better understanding of flame-wall interactions. This line of research has also potential value to material selection and heat-exchanger design of combustion devices.

Various reports point out that flame-wall interaction strongly relates to a high heat flux to the wall [27, 6, 103]. One can essentially imagine that the flame propagates toward the wall, consumes the unburned fuel-oxidation mixture, reaches the cold wall and during this process exchanges some heat with the wall, cools down in this zone and eventually quenches. It is postulated that radical recombination is responsible for quenching while the flame and the cold wall interact. Flame-wall interactino can take place in either turbulent or laminar flow regimes.

An exact narrative of flame-wall interaction is beyond our grasp at the present time due to sheer complexity of the phenomenon. There are numerous parameters involved and the underlying workings of flame-wall interaction are essentially nonlinear. Just to name a few, one could address the influence of equivalence ratio, the effect of wall temperature, the impact of pressure, and the list would go on. Some but not all of these issues have been researched. Let's have a quick look at some of them.

The net mass fraction rate of produced UHCs are studied in [54, 67, 128], and heat flux to the wall in [103, 93, 114, 35, 24, 25] both numerically and experimentally. Some studies delve into hydrogen flame interaction with the wall [26, 93]. Behavior of flame near the wall for various hydrocarbon fuels has been thoroughly explored by Boust [11] whose simulations use simple chemistry, and Westbrook [128] and Hasse [49] who employ detailed chemistry for methane and higher hydrocarbons.

Dependency of the flame-wall interaction on the inlet temperature has been investigated by Westbrook [128] and Wu [134]. Effect of wall temperature is the subject in the works of Owston [93], Owston and Abraham [94], and Popp [103]. Sotton [114] examaines the impact of pressure on the heat flux toward the wall. This has been researched also later by Owston [93] and others [40, 75, 7, 84, 45, 117, 117]. There are situations where the wall influence the chemistry of reaction which has been studied and theorized. Popp showed that the heat release rate at the wall decreases, if the surface chemistry is present [104]. How equivalence ratio affects near wall combustion and flame-wall interaction, is looked into by Vosen [123], Ezeyoke [37] and other researchers [11, 40, 87, 31].

Quenching of the flame at the wall is of special importance to us. This phenomenon is classified, based on configuration of the combustion device, into head-on quenching and side-wall quenching. These will be explained extensively later on. The head-on configuration has been theoretically studied by Wichman and Bruneaux [129], Boust [11], and numerically by Popp and Baum [103], Westbrook [128], Poinsot [102], Hasse [49], Wu [134], Owston [93] and Abraham [94], Huang [55].

There is still much to be understood about side-wall quenching. A pioneering analytical study was given by von Kármán and Millan [62], and extended later by Makhviladze and Melikov [85]. Lu [80] and Clendening [23] conducted nearly similar experiments on the topic. It has also been numerically modeled by Gruber et al. [46], and by Gruber and Chen [47].

Experimental work on quenching has been performed in abundance, but they have serious limitations. Flame-wall interaction has very short time scales and small characteristic lengths which require high precision measurements, overly sophisticated setups, and costly material. And yet the results are not up to par, because of technical limitations at this time. The flame quenching distance at atmospheric pressure is of the order of $< 100\,[\mu m]$. There are not many reliable methods to capture flame-wall interaction at such small scales.

With the arrival of recent computing technologies, we are now able to run extremely demanding computations such as DNS. This presents a huge opportunity to tackle many open problems that have been beyond our reach for a long time. Flame-wall interaction and the case of quenching is one of such problems.

Our objective is to model side-wall and head-on quenching via direct numerical simulation of methane-air mixture, using detailed chemical kinetics, Smooke multi-component mechanism and mixture-averaged diffusion coefficients. This will help us understand similarities and differences between the head-on and the side-wall quenching systematically.

Based on orientation of the flame relative to the wall, one can think of two types of configurations for flame-wall interaction in laminar or turbulent flows, namely

- the flame front being parallel to the wall, that is also the flame propagating normal to the wall, which is called head-on quenching, and
- the flame front being normal to the wall, i.e. the flow runs parallel to the wall, which is called side-wall quenching.

In this chapter, first the head-on quenching configuration is examined numerically to characterize the flame-wall interaction using multi-component Smooke mechanism and mixture averaged transport coefficients suggested by Hirschfelder[53]. Afterwards, two numerical simulations for side-wall quenching are performed. In this case the flame properties and the heat flux to the wall are investigated and are compared to the 1D head-on quenching. We emphasize that our main objective is to compare the behavior of the flame in side-wall quenching and head-on quenching in as much detail as possible. To this end, the incompressible, 3-dimensional Navier-Stokes equations are solved using `FASTEST-3D`. It is assumed that the wall is chemically inert.

7.1 Head-on Quenching

Head-on quenching can generally be categorized into

- transient configuration, in which the flamelet propagates freely toward the wall and consumes the unburnt mixture, and
- stagnation configuration, which includes a stationary burning flow normal to the wall.

In this work the head-on quenching simulations are performed on the transient configuration. There are several studies on transient case of the flame propagating toward the wall. Since different codes use different multi-component mechanisms to simulate the combustion, and since each mechanism leads to a unique flame structure, the head-on quenching of a stoichiometric methane-air flame has been simulated and will be explained.

7.1.1 Head-on quenching of Stoichiometric methane-air combustion

7.1.1.1 Configuration and computational domain

Interaction of the stoichiometric methane-air flame and the wall in a head-on quenching configuration, is simulated on a one-dimensional domain which is $0.02048[m]$ long, and is discretized using 1024 cells, $20\,[\mu m]$ each. The same simulation is then repeated on a finer mesh to examine the accuracy and mesh dependency of the simulation.

7.1.1.2 Initial and boundary conditions

Since we look at the transient configuration only, the configuration is set up to simulate this sort of head-on quenching. Thus, prior to this simulation, for the same mixture, a simulation has to be done to get a fully developed flamelet as the simulation converges. For initialization, this developed flamelet is placed far from the wall to mitigate the effects of wall's presence. This distance has been suggested in the FWI literature to be at least four flame thicknesses which makes at least 2[mm] for the methane-air mixture, considering $\delta_f \approx 0.5\,[mm]$.

Similar to the simulation of flamelets, the geometry consists of symmetry and outflow boundary conditions. The inlet condition here is switched to solid wall. The solid wall is assumed to be isotherm with the temperature $T_w = 300\,[K]$. This allows the heat flux through the wall. To prevent density fluctuations at the wall, its temperature is set to be equal to the unburnt temperature of the mixture $T_{wall} = T_u$. The species gradient at the wall is also set to zero,

$$\left.\frac{\partial Y_k}{\partial x}\right|_{wall} = 0\,, \qquad k = 1, \ldots, N\,. \tag{7.1}$$

The boundary condition at the outlet is set to Neumann or as explained in chapter 4, the zero gradient condition. Another important parameter at the wall is diffusion velocity. This parameter is set to zero normal to the wall, at its vicinity. Since the wall temperature is low enough ($T_{wall} \leqslant 400\,[K]$), the Soret and Dufour cross diffusion effect can be neglected.

The pressure across the domain is assumed constant and equal to the ambient pressure. Under this setting the simulation is performed with a time step $\Delta t = 0.15 \times 10^{-8}[s]$.

7.1.1.3 Flame structure and flame-wall interaction

After starting the simulation the flame propagates toward the wall, touches the wall, and then quenches. Observing the whole phenomenon, one can recognize that the flame goes through different phases during the simulation, which are explained in the sequel with illustrations.

TRANSIENT PHASE AFTER STARTING SIMULATION

When simulation starts, it takes a while for the flamelet to adjust before it propagates. As can be seen in figure 7.1, this phase of simulation does not follow any particular pattern. Let us begin with the temperature profile in figure 7.1a. The profile does not move notably from $t = 0\,[s]$ until $t = 0.0015\,[s]$. This behavior reoccurs in all other figures. One and a half milliseconds later, the flame starts moving toward the wall. Contrary to a freely propagating flame, this propagation does not have a constant velocity. Considering figures 7.1d–7.1h, the peak of mass fraction of these species, as an identifier of the profile's position, moves very slowly from $t = 0.0015\,[s]$ to $t = 0.003\,[s]$, whereas it propagates much faster from this moment on until $t = 0.0045\,[s]$.

Another problem to consider in the transient phase of simulation is the gradient of the maximum values of mass fraction. While the maximum value decreases monotonically for some species e.g. CH_3 and CH_2O, it increases and then decreases for some others like HO_2. This observation clearly confirms the non-stationarity of this phase.

FREELY PROPAGATING FLAME

The profiles of this zone are presented in figure 7.2. In this zone, the flamelet finds its stationary shape. It keeps its pattern and the maximum values remain constant until the flamelet senses the wall. In this phase mass fraction profiles propagate with the laminar burning velocity of the mixture which is the s_l of the stoichiometric methane-air. In this

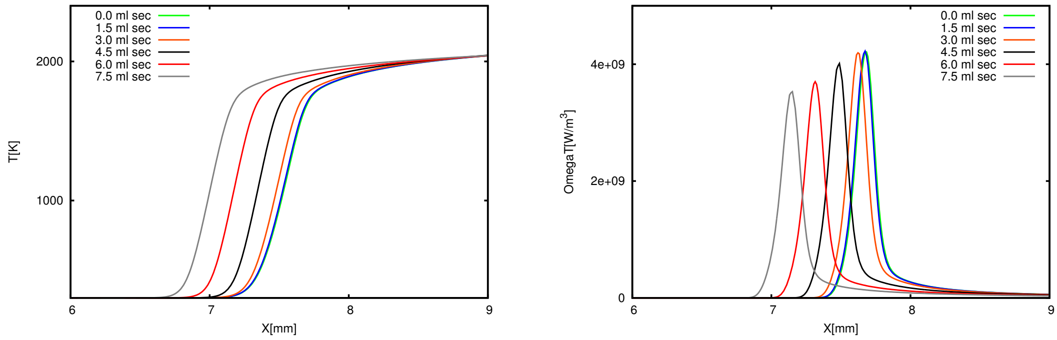

(a) T[K] (b) $\omega_T [W/m^3]$

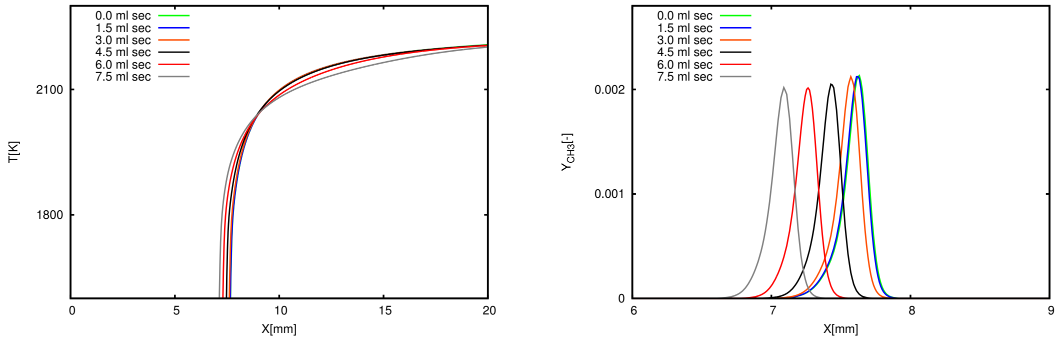

(c) T[K], zoomed (d) CH_3

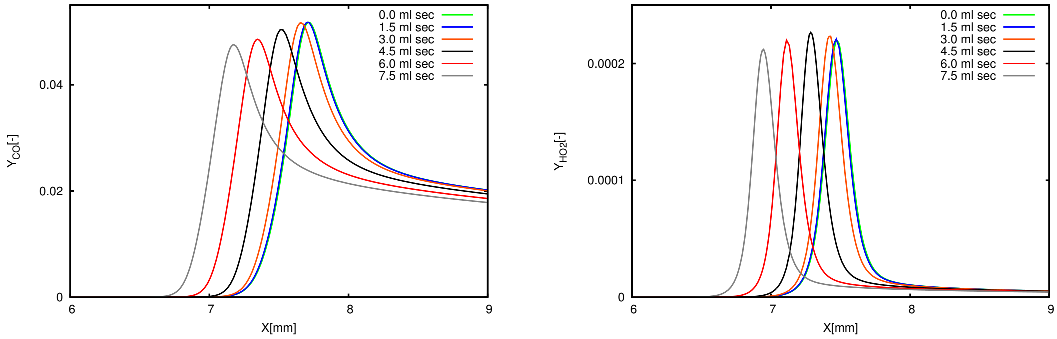

(e) CO (f) HO_2

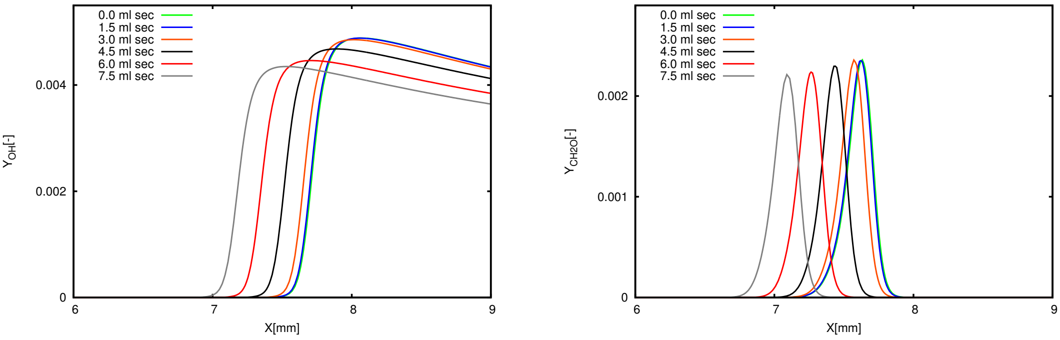

(g) OH (h) CH_2O

Figure 7.1: Plots of heat release rate, temperature, and the mass fraction profiles of CO, CH_3, HO_2, OH, and CH_2O during the transient phase from $t = 0\,[s]$ to $0.0075\,[s]$.

period all flame characteristics remain unchanged and approximately equal to those of the undisturbed stationary laminar flamelet.

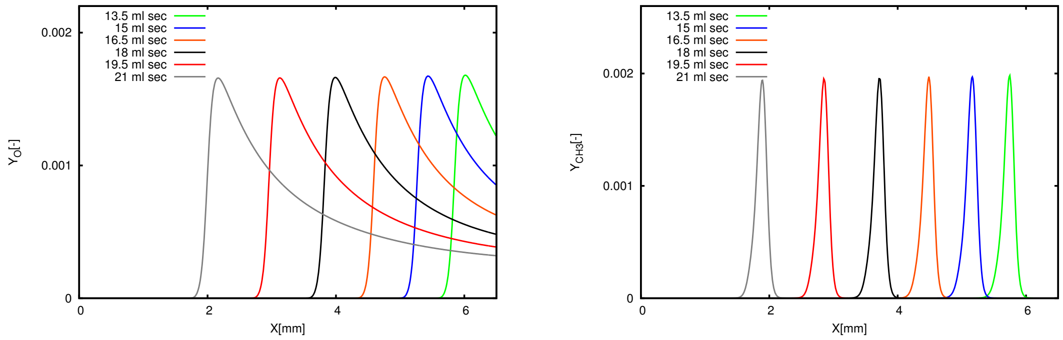

(a) O (b) CH_3

Figure 7.2: Plots of the mass fraction profiles of CH_3 and O during the propagating phase from $0.013[s]$ to $0.021[s]$.

SENSING THE WALL AND QUENCHING

This phase is the first phase during which the flame interacts with the wall. The presence of the wall is felt by the flame when it enters a specific zone, which for the methane-air mixture in this particular simulation is a distance approximately equal to $45\,[\mu m]$ from the wall. This number is in agreement with the results by Popp et al. [103] who reports 2 flame thicknesses as the wall influence zone.

In figure 7.3, the profiles of the maximum heat release rate ω_T, the temperature and some species mass fractions, which are especially important in flame-wall interaction, are demonstrated. One has to notice that within this time interval starting the moment when the flamelet feels the presence of the wall and ending when it quenches, everything happens very quickly. It takes only about $10^{-4}\,[s]$ for the flame to penetrate this zone, sense the wall, interact with the wall, exchange heat with the wall, and finally quench. Profiles are plotted from $23.07\,[ms]$ to $23.4\,[ms]$. The time step, in which the flame senses the wall can be identified following the changes in flame characteristics at the wall, namely the gradient of the temperature profile or the maximum value of the heat release rate. As we can see in figure 7.3a, the maximum rate of the heat release grows slightly after $t = 23.07\,[ms]$. This trend continues for approximately $0.2\,[ms]$ when the distance from the wall is around $30\,[\mu m]$. After that the peak of the profile drops but the gradient of ω_T and its value at the wall increase until it quenches. The profiles at the quenching moment are plotted in black.

The onset of flame-wall interaction can be also recognized from the gradient of temperature profile. When the wall begins to influence the flame, the gradient of temperature profile increases. This tendency remains until quenching when the gradient reaches its maximum. Some researchers take this very idea as the definition of quenching moment [102, 101, 103]. It is said that there is a distance y_q at which the flame stops and quenches. At this distance

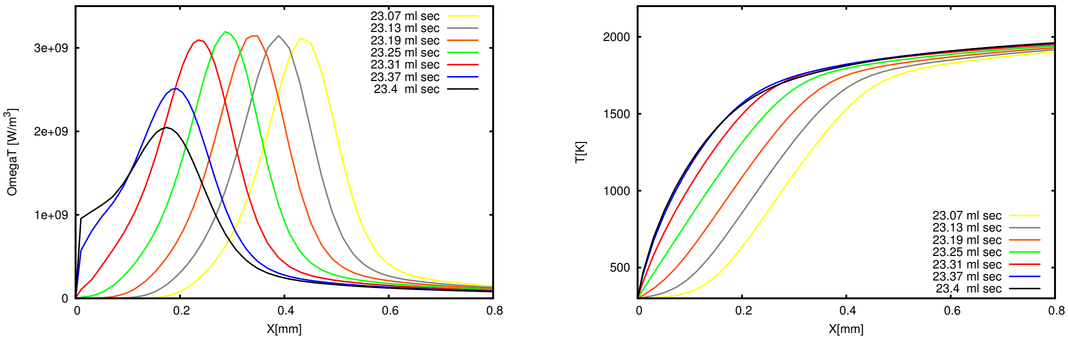

(a) $\omega_T[W/m^3]$ (b) T[K]

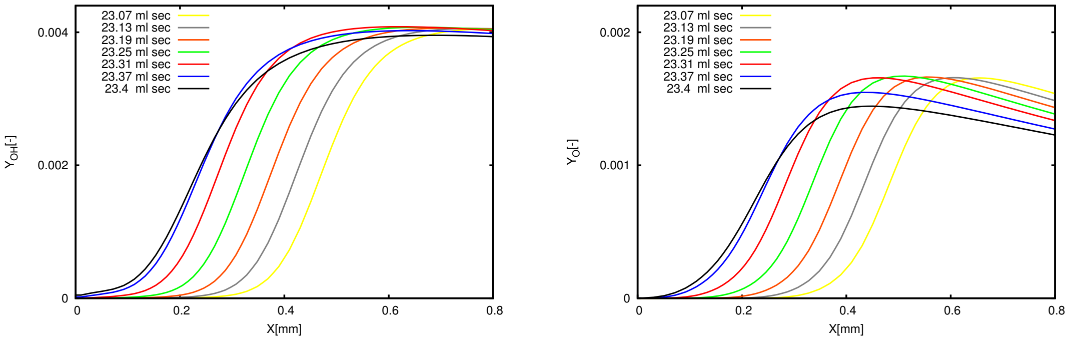

(c) OH (d) O

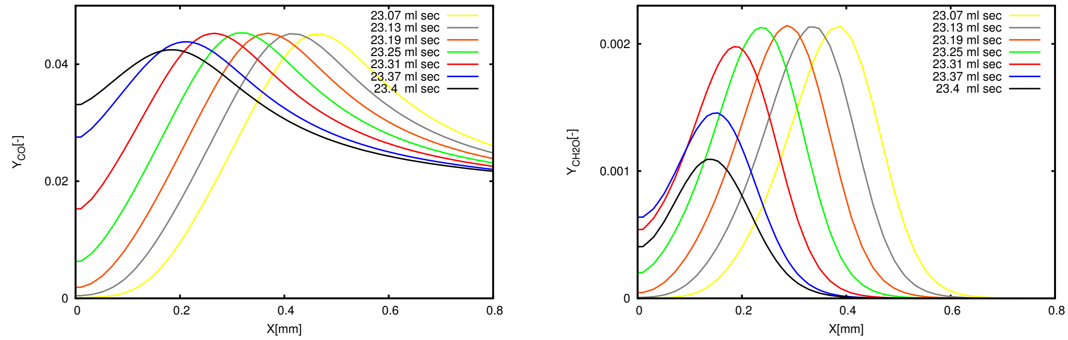

(e) CO (f) CH_2O

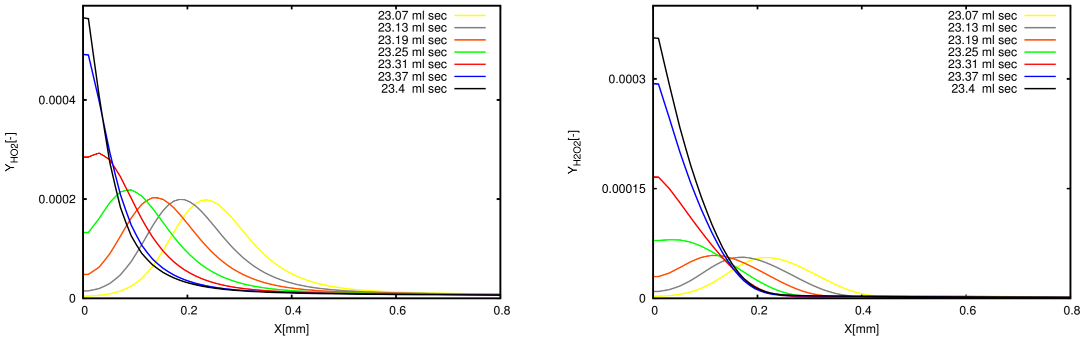

(g) HO_2 (h) H_2O_2

Figure 7.3: Plots of the temperature, and mass fraction profiles of OH, O, CO, CH_2O HO_2 and H_2O_2 after flame senses the wall from $t = 0.02307\,[s]$ until $t = 0.0234\,[s]$ when it quenches. The black lines indicate profiles at quenching moment.

the heat flux toward the wall reaches its maximum [101].

$$\Phi_q = \max\ \lambda \frac{\partial T}{\partial x}\bigg|_{wall} , \tag{7.2}$$

where Φ_q is the heat flux to the wall at the quenching moment, with the assumption that there is no radiation and the wall heat flux is diffusion-controlled. This monotonic increase of heat flux is responsible for the quenching. As the consequence of the increasing heat flux at the wall, the flame becomes cooler until it quenches. It is hypothesized that the flame propagates toward the wall as long as the heat loss to the wall has not reached almost 30% of the flame power [101].

The species behave in etirely different ways during the flame-wall interaction. The mass fraction profiles of O and OH, figures 7.3c and 7.3d, do not show significant changes indicating the presence of the wall, whereas those of CH_3 and CH_2O at the wall, exhibit an increase. The CH_3 increases until $0.06\,[ms]$ has passed the time step, at which moment the rate of heat release reaches its maximum value after it starts being affected by the wall. Next, CH_3 decreases until the flame quenches. Figure 7.3f indicates that CH_2O increases until $t = 23.37\,[ms]$ which is $0.06\,[ms]$ after CH_3 starts decreasing, but the general behavior is similar to CH_3. The other species i.e. CO, HO_2, and H_2O_2 increase at the wall right from the beginning, when the flame enters the wall's territory! This behavior continues until the flame quenches (see figures 7.3e, 7.3g, and 7.3h). At the wall, HO_2 and H_2O_2 increase gradually until they reach a certain value which is considerably higher than that of a freely propagating flamelet of a stoichiometric methane-air mixture, interestingly.

AFTER QUENCHING

Although there are some multi-component chemical mechanisms with which it is not possible to simulate after quenching, with Smooke mechanism it is possible to investigate the complete interaction of the wall and flame, from long time, before the flame senses the wall, until long time after quenching. This can be counted as an advantage of this mechanism.

Figure 7.4 illustrates the behavior of the flame after quenching from $t = 23.34\,[ms]$, which is short before quenching, until $t = 23.68\,[ms]$. As mentioned before, temperature profile reaches its highest gradient at the quenching moment. After that, the gradient decreases gradually until it affects the temperatures farther from the wall. This means, starting from the wall toward the flame, temperature drops gradually. This can be seen in figure 7.4b. The yellow line shows the final time step which indicates a considerably lower temperature at the right side of the figure compared to the other lines. With decreasing temperature gradients, the heat release rate at the wall decreases too. This can be seen in figure 7.4a, which shows that the curve is more flattened as the time goes by passed the quenching. Similar to the previous phase, the behavior of mass fractions can be classified into categories from which the most important species will be discussed here.

Mass fraction profiles of O and OH are given in figures 7.4d and 7.4c. Analogous to previous phase, there is no dramatic change at the wall. However, further into the domain their values decrease, as the temperature drops. On the other hand, CH_3 and CH_2O continue their decline at the wall. This is plotted for CH_2O, representatively of its group, in figure 7.4e. The maximum values, which take place around $20\,[\mu m]$ from the wall, become

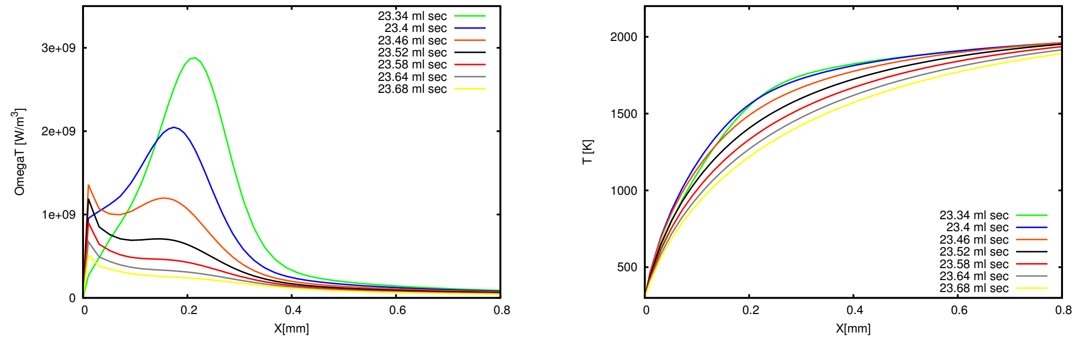

(a) ω_T (b) T[K]

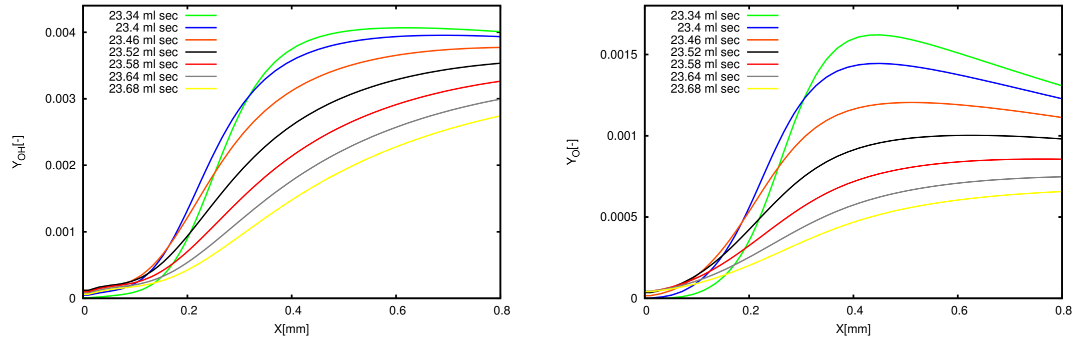

(c) OH (d) O

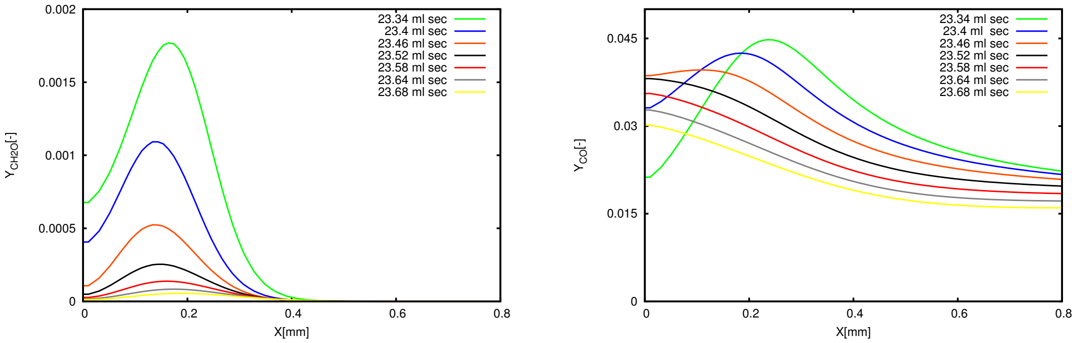

(e) CH_2O (f) CO

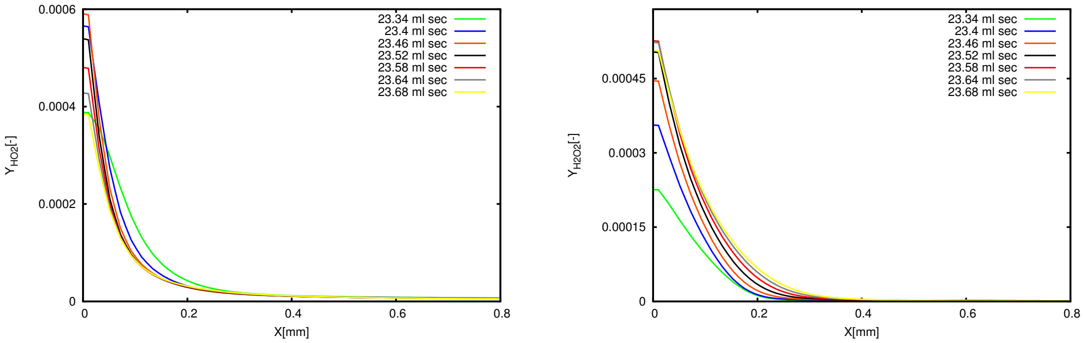

(g) HO_2 (h) H_2O_2

Figure 7.4: Plots of temperature and mass fraction corresponding to OH, O, CO, CH_2O HO_2, and H_2O_2, for time instances short before quenching $t = 0.02334\,[s]$ until short after $t = 0.0237\,[s]$. The blue lines indicate the profiles at quenching moment.

smoother as the simulation proceeds. CO, HO_2, and H_2O_2, which are the most important species in near-wall combustion, indicate an entirely different trend and develop further after quenching.

For CO the corresponding mass fraction profiles are shown in figure 7.4f. As the plot indicates, the mass fraction continues growing after quenching until $t = 23.46\,[ms]$. After this time, CO starts decreasing. Similar to CH_2O and CH_3, its maximum within the domain decreases and the curves start becoming flatter. At $t = 23.52\,[ms]$ and afterwards the maximum value is exactly at the wall. HO_2 behaves exactly the same: it increases after quenching until the same time step and then decreases gradually. This growth trend lasts longer than any other species in the case of H_2O_2. This is shown in figure 7.4e. This behavior takes about $0.22\,[ms]$. After that, H_2O_2 follows the same pattern as HO_2.

DISCUSSION: FREELY PROPAGATING FLAME

In near-wall combustion, the flame characteristics are uniquely affected by the mechanism. We intend to explain the flame-wall interaction with regard to the Smooke mechanism in methane-air combustion. As given by table 3.2, we have

$$\mathrm{CH_4 = CH_3 + H} \qquad \text{(10) start reaction} \tag{7.3}$$
$$\mathrm{CH_4 + H = CH_3 + H_2} \qquad \text{(11) propagating reaction} \tag{7.4}$$
$$\mathrm{CH_4 + OH = CH_3 + H_2O} \qquad \text{(12) propagating reaction} \tag{7.5}$$

Giving enough energy to CH_4 molecules, enables the H-atoms to separate from CH_4 and build a CH_3 radicals. Another part of the existing methane in the mixture reacts with the produced H-atoms in previous reaction through reaction (7.4)) and produces another part of CH_3. Alkyl radicals are produced also through reaction (7.5). Both these reactions are chain propagating which help the combustion to follow the path. The start reaction of the mechanism or the reaction which describes the preparatory decomposition of methane is strongly endothermic. The zone in which the methane breaks down is called the induction or, in other words, the preheat zone. The shape of the flame, which demonstrates the induction zone is plotted for two completely different time steps in figure 7.5.

After these three reactions, the CH_3 radicals react with O radicals to deliver formaldehyde and hydrogen atoms,

$$\mathrm{CH_3 + O = CH_2O + H} \qquad \text{(13) propagating reaction} \tag{7.6}$$

Through two sequential reactions,

$$\mathrm{CH_2O + H = HCO + H_2} \qquad \text{(14) terminating reaction} \tag{7.7}$$
$$\mathrm{CH_2O + OH = HCO + H_2O} \qquad \text{(15) terminating reaction} \tag{7.8}$$

The HCO radicals are formed while formaldehyde is reacting with OH and H radicals. Both latter reactions (7.7) and (7.8) are terminating reactions. Consequently, the HCO radicals decompose either through reacting with H through (7.9) or through collisions with a second body (7.10) yielding CO and H.

$$\mathrm{HCO + H = CO + H_2} \qquad \text{(16) branching reaction} \tag{7.9}$$
$$\mathrm{HCO + M = H + CO + M} \qquad \text{(17) branching reaction} \tag{7.10}$$

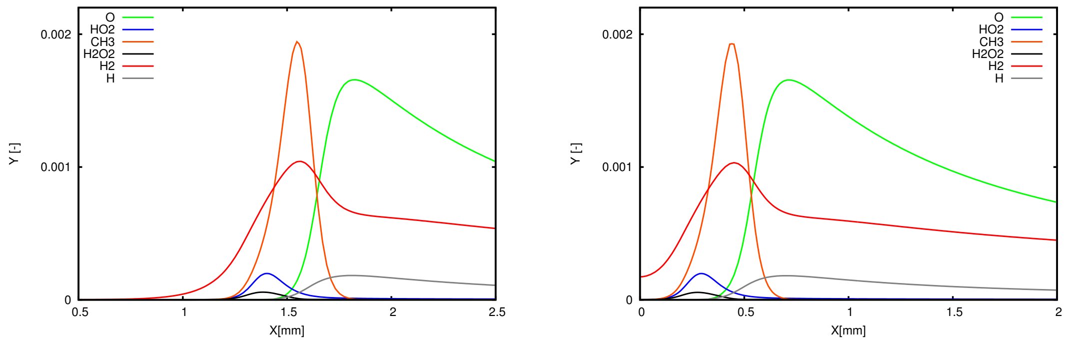

(a) $0.012[s]$ (b) $0.023[s]$

Figure 7.5: Mass fraction profiles of of some species showing the induction zone of the flame for two different time steps; left, $t = 0.012\,[s]$ after starting the simulation; right, $t = 0.023\,[s]$ short before the flamelet is affected by the wall.

This reaction path dictates the flame shape [126]. As it can be observed in figure 7.5, the flame structure remains the same through the reaction and will be preserved even after the flame quenches but with insignificant differences. As an example, consider the distance between the maximum of the CH_3 profile and that of the H2. They always move side-by-side and the relative velocity between their peaks is zero. The same behavior holds for for all other species profiles, both minor and major, that are not shown here.

DISCUSSION: WHY FLAME QUENCHES

To decompose the methane and alkyl radicals through (7.4), (7.5), and (7.6) and make the whole process continue, the H, O and OH radicals are needed. These radicals are produced through following reactions

$$\begin{aligned} \mathrm{H} + \mathrm{O_2} &= \mathrm{OH} + \mathrm{O} && \text{(1) branching reaction} && (7.11)\\ \mathrm{O} + \mathrm{H_2} &= \mathrm{OH} + \mathrm{H} && \text{(2) propagating reaction} && (7.12)\\ \mathrm{OH} + \mathrm{H_2} &= \mathrm{H_2O} + \mathrm{H} && \text{(3) propagating reaction} && (7.13) \end{aligned}$$

These latter three reactions are highly endothermic and have relatively high activation energies. Again inspecting the figure 7.5, one can see that the peak of profile of the HO_2 mass fraction is always in front of that of other species like CH_3, O and H_2. Being nearer to the wall for HO_2 radicals means that its profile is actually the beginning of the pre-heating zone. Therefore this intermediate can freely diffuse toward the wall without needing to go through other annoying reactions. A look at the mechanism reveals that HO_2 radicals are produced through the following reaction

$$\mathrm{H} + \mathrm{O_2} + \mathrm{M} = \mathrm{HO_2} + \mathrm{M} \qquad \text{(5) propagating reaction} \qquad (7.14)$$

which is a propagating reaction and has **zero activation energy**. This means that the H radicals and O_2 molecules required for the reaction (7.11) and consequently for (7.12)) and (7.13) to produce OH and O, are consumed in reaction (7.14). This also decelerates (7.4), (7.5) (7.6) to go on with their previous rates. That is the reason for accumulation of the HO_2 at the wall.

As mentioned before, the production of HO_2 in (7.14) takes place next to the cold wall. The reactions (7.6), (7.9), and the following reaction have zero activation energy

$$HO_2 + HO_2 = H_2O_2 + O_2 \qquad \text{(21) terminating reaction} \tag{7.15}$$

Through these reactions, CH_2O, CO, and H_2O_2 are produced. As we thoroughly explained, all of these species experience an increase phase after the flame senses the wall. This is because these reactions take over the competitor reactions which need the same reactants and consequently their products increase near the wall. Consider equation (7.15), for instance, and compare it to the following reactions

$$H + HO_2 = H + O_2 \qquad \text{(7) terminating reaction} \tag{7.16}$$

$$OH + HO_2 = H_2O + O_2 \qquad \text{(8) terminating reaction} \tag{7.17}$$

Contrary to reaction (7.15), both of these reactions are endothermic. That means (7.15) takes over the reactions (7.16) and (7.17). On this account, the H_2O_2 follows the pattern of HO_2 and accumulates near the wall. The fact that H_2O_2 keeps increasing, even after HO_2 begins to decrease, (figures 7.4g and 7.4e) can be explained through reaction (7.15). This reaction is responsible for consumption of HO_2 directly at the cold wall.

Long enough after quenching, the whole mixture is affected by the wall including production of the reaction (7.14) and consequently reaction (7.15). Then H_2O_2 experiences a decrease of mass fraction at the wall.

INCREASING THE HEAT RELEASE

As stated earlier, HO_2 radicals recombine through reaction (7.15). Although this reaction is not exothermic, the fact that reactions (7.16) and (7.17), both endothermic, are overtaken by a reaction with zero activation energy to consume HO_2, results in a faster heat release. That means the more H_2O_2 production, the faster the heat release. This supports the observed growth of heat release rate after the flame is affected by the wall.

7.1.1.4 Scatter plots of CO concentration versus temperature

Mann et al. conducted a series of experiments to examine the thermo-kinetics of the transient flame-wall interaction [86]. He provided a scatter plot of the mole fractions of carbon monoxide versus temperature at six different probe locations, starting far from the wall at $X = 1.7\,[mm]$ all the way to $X = 0.1\,[mm]$ close to the wall. His measurements can be seen in figure 7.6.

From these plots, one can see that far from the wall e.g. at $X = 1.7\,[mm]$ the points show two branches. The left branch belongs to the unburnt mixture, before the flame propagates through the designated probe position and the second branch indicates the post flame zone. The nearer the measurement point is to the wall, the more the two branches converge to each other. This behavior is pronounced especially at distances less than $0.3\,[mm]$ from the wall. This behavior reoccurs through figure 7.4f, also considering the behavior of the freely propagating flame.

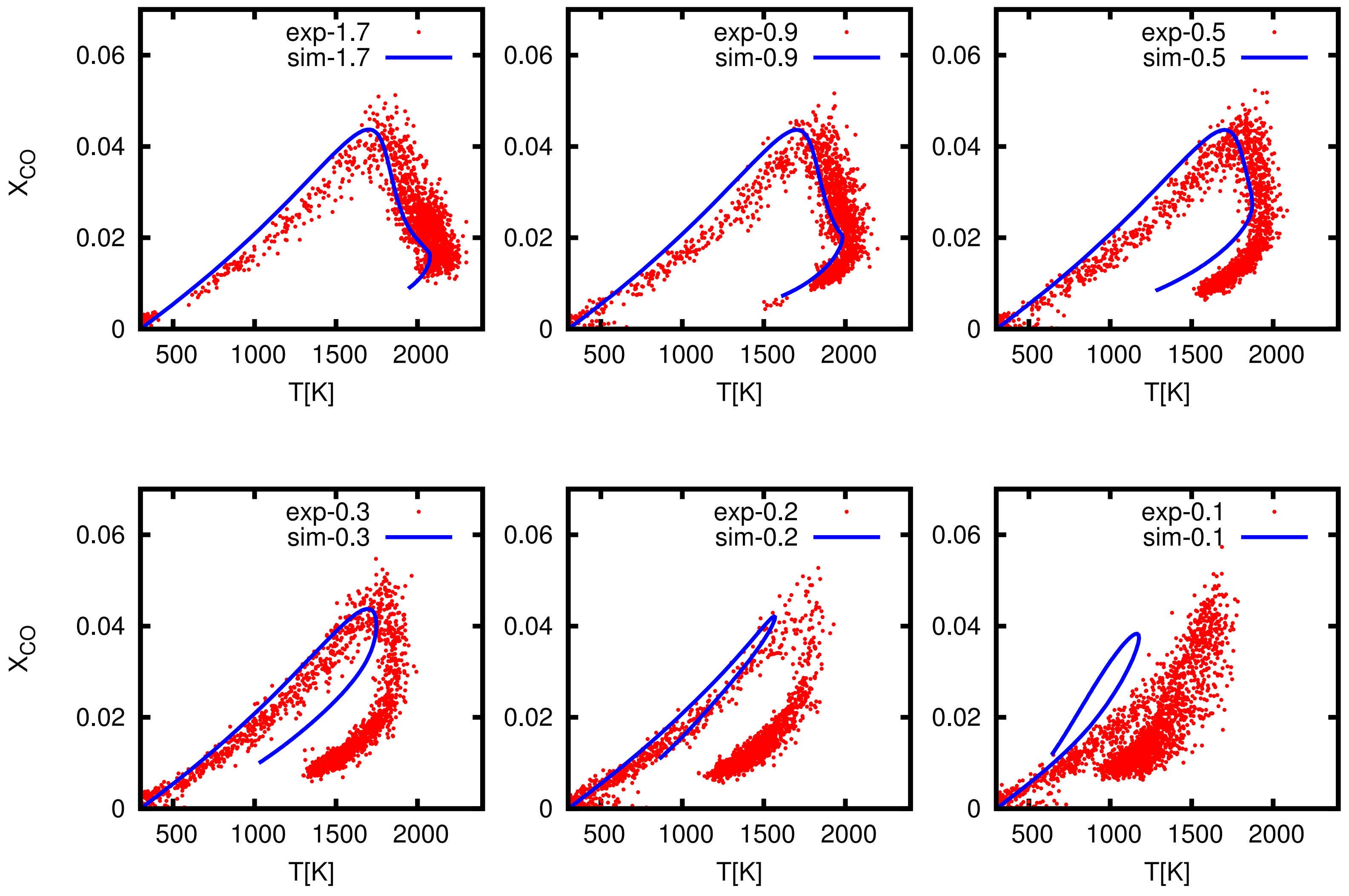

Figure 7.6: CO mole fraction scatter plots for a stoichiometric methane-air flame at different distances from a cold wall. The points indicate measurements. The solid lines indicate the numerical results. Top-left, the results at 1.7 $[mm]$. Bottom-right, the results at 0.1 $[mm]$.

Far from the wall, before the flame passes through $X = 1.7\,[mm]$, the flamelet is not under influence of the wall. During the movement of the flame, mole fraction of CO increases gradually until it reaches its maximum. This happens through reactions (7.9) and (7.10) of the mechanism. Since the flame has not sensed the wall yet, there are enough OH radicals which have been produced through reactions (7.11) and (7.12). These reactions provide enough reactants, OH, to consume the CO. But this happens in the post flame zone, where temperature is high. Near the wall, as explained before, the reaction does not follow the normal path and the flame is strongly under the impact of the wall. The CO increases as the probes get closer to the wall. For more comprehensive description of the experiment see [86].

To compare the numerical results with the experimental data, the previously explained HOQ configuration was simulated on three different meshes which measure 10 $[\mu m]$, 20 $[\mu m]$, and 40 $[\mu m]$ respectively. The results obtained from the latter simulation differed slightly with the first two simulations. Therefore only the results of the first simulation on the finest mesh are presented here. Every 1000 time steps, one data point was output from the simulation, and the results were overlaid on the scatter plot. Next, the CO mole fraction versus temperatures were plotted. The numerical results are the blue lines in the figure 7.6. One would say that far from the wall, where the flame has not yet been affected by the wall, the numerical results are in good agreement with experimental data. As the flame propagates toward the wall, simulation starts to deviate from the experiment. The convergence of the two branches of the profiles in numerical simulation is stronger, and the experimental data shows lower mole fraction of CO for a given value of temperature. For example consider corresponding value of CO when the $T = 1500\,[K]$ at $0.2\,[mm]$ distance from the wall. The simulation predicts $X_{CO} = 0.037$ whereas the experiment indicates a mole fraction equal to 0.01 at the post flame zone. Moreover, the last measurement point shows completely different trend in numerical predictions compared to the scatter points at $0.1\,[mm]$ relatively far from the wall. At this point numerical simulation anticipates higher mole fraction of CO at the post flame zone than the experimental scatter plot (for example at $1000\,[K]$).

Our numerical simulation of flame-wall interactions have been verified by comparison to the works of Popp et al. Here are some probable sources of deviations and discrepancies

- convective velocity
- mechanism
- Soret and Dufour effect
- measurement

which we explain shortly.

7.1.1.5 Probable sources of deviation

1) IMPACT OF CONVECTIVE VELOCITY

The axial velocity of the flow in the experiment is reported $u_0 = 2.62\,[m/s]$. This velocity does not exist in the numerical setting, since the convective velocity was set to zero. In transient configuration of HOQ, the flamelet is permitted to propagate with the laminar burning velocity of the mixture and zero convective velocity. Given the laminar burning velocity of a stoichiometric methane-air flame as $s_l = 0.367[m/s]$, these two velocities have to be summed up to deliver the relative velocity of the movement of the flame front toward the cold wall. This extra velocity in the experimental setup pushes the flame toward the wall with it momentum. Because of that, higher temperatures have been recorded in the pre- and post-flame zones near the wall. For example one can consider a point at $0.1\,[mm]$ distance from the wall, where the highest predicted temperature is $T \approx 1300\,[K]$, whilst the experiment reports $T \approx 1600\,[K]$.

2) IMPACT OF MECHANISM

The simulations in this work are performed using the Smooke mechanism having the C_1 path (4 elements, 16 species and 25 elementary reactions). There are alternative Smooke mechanisms which are more complicated and bear more details. For instance, the one for C_1 path with 4 elements, 16 species and 47 reactions. Obviously the mechanism used by van Oijen [119] and also in this work is a reduced version of this mechanism. As reported by Popp et al. [104], in order to examine the flame-wall interaction using multi-component mechanisms which can provide a more complex chemistry, one needs a reliable mechanism.

This mechanism has been extensively verified in predicting the laminar burning velocity in different settings (Le = 1 and mixture-averaged), adiabatic temperature, mass fraction profiles in different flame zones. Nevertheless, since none of the above mentioned test cases include transient and non-adiabatic near-wall simulations, it remain unclear whether the mechanism could be a source of discrepancy.

To be able to rule out the uncertainty of the mechanism, same simulation can be repeated using a complete form of the Smooke mechanism. To investigate the impact of the C_2 path, the HOQ configuration can be simulated using either the Smooke and Giovangigly mechanism, i.e. C_2 path with 4 elements, 20 species and 62 reactions, or a more complex mechanism like GRI-3.0 with 53 species and 325 reactions, which also considers the C_2 path. Performing a simulation with such detailed chemistry is computationally expensive, but in return it can guaranties the reliability of the mechanism.

3) SORET AND DUFOUR EFFECTS

To calculate the diffusion velocities which are explained in a simplified form in chapter 2 for a gas mixture consisting of N species, the following system has to be solved [131]

$$\nabla_x X_i = \sum_{j=1}^{N} \frac{X_i X_j}{D_{ij}} (V_j - V_i) + (Y_i - X_p) \left(\frac{\nabla_x p}{p} \right) + \left(\frac{\rho}{p} \right) \sum_{j=1}^{N} Y_i Y_j (f_i - f_j) + \frac{\kappa_i}{T} \frac{\partial T}{\partial y} \,, \quad (7.18)$$

with $i = 1, ..., N$. This is the complete form of the multi-component diffusion equation in which, the $f_i - f_j$ accounts for the difference in the body force per unit mass, acting on two different species i and j and

$$\kappa_i \equiv \sum_{j=1}^{N} \left(\frac{X_i X_j}{\rho D_{ij}} \right) \left(\frac{D_{T,j}}{Y_j} - \frac{D_{T,i}}{Y_i} \right) \,, \quad (7.19)$$

where $D_{T,i}$ is the thermal diffusion coefficient of species i in the corresponding multi-component mixture and κ represents the thermal diffusion or the so called Soret effect and describes the mass flux due to temperature gradient. There is the similar effect or the twin effect appearing in energy equation, named Dufour effect which describes the energy flux due to mass concentration gradient. These two effects together are called cross diffusion effect and are neglected (they are assumed to be negligible in simulations performed in this work) in most combustion codes. But the cross diffusion effects, including the Soret effect, may in some cases form around the ordinary diffusion processes and may even change the stability character of the flame [131].

Equation 7.18 suggests that the Soret effect can be taken into account wherever there is a temperature gradient. The larger this temperature gradient, the bigger the error of neglecting the Soret effect. The same interpretation holds for Dofour effect in the energy equation i.e. it becomes important in a multi-component mixture, whenever there is a considerable mass concentration gradient.

Looking back at the head-on quenching results, we could say that neglecting the cross diffusion effects might be a source of error, since at the vicinity of the wall there are extreme high temperature and mass concentration gradients. Figure 7.3b indicates that within less than a millisecond the flame thickness drops approximately by one order of magnitude, which is inversely proportional to temperature gradient. This could be theoretically important, in predicting the maximum temperature and CO mole fractions in figure 7.6.

4) MEASUREMENT INACCURACY

Although the measurement instruments have improved almost to the point of perfection, one might say, the accuracy of measurement will always be bounded and therefore an inevitable source of error. For instance let us focus on the length scales involved in the problem at hand. While the flame thickness is of the order of $0.1\,[mm]$, one tenth of millimeter displacement could result in $1000\,[K]$ discrepancy (figure 7.6) which is not negligible at all. As shown in the figures 7.2-7.4, the distance from the wall plays a substantial role in flame-wall interaction, especially in the zone affected by the wall. In that zone even the allowable tolerance of the measurement instrument could result in considerable error, which might affect the results with which the flame-wall interaction is characterized.

7.2 Side-wall quenching

Although there is vast theoretical, experimental, and numerical body of research on the head-on configuration of the flame-wall interaction, there are few works concerning the side-wall configuration, either in laminar or in turbulent flame regimes. The main reason for that is the cost of computation. While the HOQ simulations can be performed using one-dimensional finite difference code, the side-wall quenching has to be simulated using two-dimensional domain, for the laminar combustion regime and three-dimensional domain, for turbulent flame-wall interactions.

Improved computation capacity of research centers has made it possible to delve into this topic and better understanding the SWQ configuration. Gruber et al. [47] have recently performed a three-dimensional direct numerical simulation to investigate the interaction between the wall and a turbulent hydrogen-air flame using multi-component reaction mechanism. Prior to his work there have been experimental and theoretical studies mostly, and numerically simulations were performed based on simple chemistry only. Alshaalan et al. [1] tried to study turbulent premixed flame-wall interactions in a Couette channel flow and performed some direct numerical simulations but only for a chemistry based on a *single-step* reaction with heat release. Long before that, Ezekoye [36] performed DNS on SWQ configuration, again assuming simple chemistry.

Lack of sufficient theoretical and numerical works in this area makes it more difficult to acquire enough information to characterize the flame-wall interaction in side-wall quenching. These reasons are enough motivation to carry out more sophisticated direct numerical simulations on near-wall combustion. The simulations in this work have been performed for a typical geometry on premixed methane-air near-wall flame. Two different two-dimensional (a quasi 3-D) direct numerical simulations were performed.

7.2.1 Configurations

7.2.1.1 SWQ - transient configuration

Figure 7.7a represents the laminar premixed methane-flame, interacting with the wall in a transient side-wall quenching configuration. The simulation has been performed on a quasi three-dimensional geometry, which is $0.02\,[m]$ long and $0.01\,[m]$ wide, discretized with uniform $20\,[\mu m]$ cells in both direction.

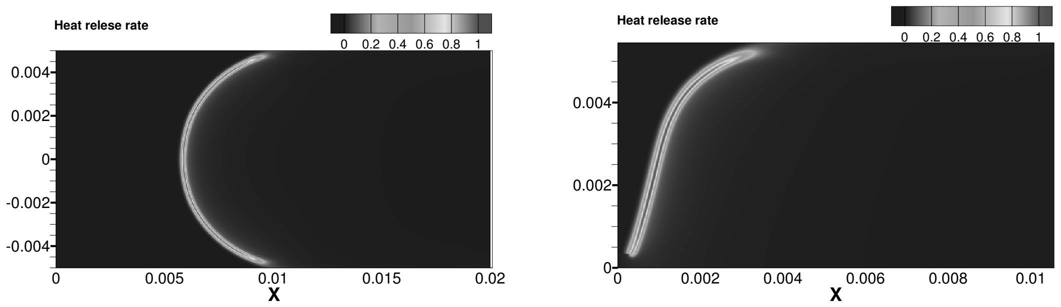

(a) SWQ-transient configuration

(b) SWQ-pilit stabilized flame

Figure 7.7: Configurations used for direct nimerical simulation of the side-wall quenching of a stoichiometric premixed methane-air flame. The contours show the heat release rate normalized the corresponding value of a freely propagating flamelet obtained by the same mixture. a)transient configuration. b)pilot-stabilized

BOUNDARY AND INITIAL CONDITIONS

The initial and boundary conditions of this simulation are similar to that of the corresponding head-on quenching configuration. The inlet temperature is set to $300\,[K]$. The surfaces $Y = \pm 5[mm]$ are the walls with temperatures equal to inlet temperature. Both surfaces fulfill symmetry condition in Z-direction. Similar to producing a flamelet, the inlet velocity is assumed equal to the laminar burning velocity of the mixture which is

$u_{in} = 0.36749728\,[m/s]$, and the flow direction is from left to right. The pressure is assumed to be constant everywhere and equal to ambient pressure. The outlet is set to convective outflow boundary condition, which has been precisely explained before.

The simulation is initialized similar to one-dimensional simulations extended to the second dimension – here the Y-direction. For the temperature a gradually increasing profile from $300\,[K]$ to $2227\,[K]$ is used. To avoid a density jumpa bubble function – multiplication of hyperbolic tangent in X and Y directions – is employed. The species are initialized using a hyperbolic tangent that provides a smooth translation between the stoichiometric mixture and air. Finally the initial velocity is assumed to be equal to the inlet velocity.

At the beginning of the simulation, since the initialized flame is far from the final solution, the simulation needs considerable time to build up the flame and the radicals. Then the flame spreads out until it confronts the wall. Although the inlet velocity is equal to s_l of the methane-air mixture, in the proximity of the cold wall, the burning velocity is not equal to the laminar burning velocity of a freely propagating flame anymore—it is in fact smaller. This results in a positive "flow-flame front" relative velocity which forces the flame front to propagate toward the outlet, though very slowly but not negligible. This means that a straight (not curved) flame front vertical to the wall is not easily attainable.

The flame front builds a parabolic-shaped flame after some time. The longer the simulation is running, the more the flame strains in the middle of the domain at $Y = 0\,[mm]$. The strained flame has not anymore the characteristics of the freely propagating flame. This means the burning velocity of the flame changes as the flame is strained, which results in a moveming flame front. On this account, this configuration is called transient.

7.2.1.2 SWQ: pilot-stabilized flame configuration

The configuration used to simulate side-wall quenching of pilot-stabilized laminar stoichiometric premixed methane-air flame is demonstrated in figure 7.7b. The length of the domain is $L_x = 0.01024\,[m]$ and its width is $L_y = 5.44\,[mm]$. The mesh consists of $(256 + 16) \times 512$ uniform cells $20\,[\mu m]$ each.

BOUNDARY AND INITIAL CONDITIONS

To be able to simulate a pilot-stabilized flame, two different inlets are defined. One for the reactable mixture and the other one for piloting the main flow. Knowing that the flow runs from left to right, $0.32\,[mm]$ of the lowest part of the inlet is set aside for a co-flow. Hot burnt methane-air mixture, with the mass fractions and temperature equal to those of the equilibrium state of the corresponding burnt mixture of the main flow, is designated as the co-flow. The inlet velocity for the co-flow is set to $1\,[m/s]$. The upper side of the inlet has the same conditions as the transient configuration, except the inlet velocity is allowed to vary if required. The entire domain is filled with air and the reactants can flow inside the domain through the upper inlet. The pressure is set to $1\,[bar]$ and surfaces in Z-direction and the $Y = 0$ surfaces are set to symmetry condition. The upper surface $Y = 5.44[mm]$ is assumed a solid wall, with wall temperature equal to $T_w = 300\,[K]$.

The hot burnt mixture flowing toward the outlet, confronts the unburnt mixture along the domain and builds the flame front along the velocity-temperature gradient of the two flows. The larger velocity of the co-flow forces the flame front to attach to the wall at

$Y = 5.44\,[mm]$. For lower velocity differences, the distance of the attachment point of the flame front to the wall from the inlet is larger. This makes it possible to adjust the two velocities to build a more vertical flame toward the wall. Despite piloting the flow, the far end of the flame is not vertical to the wall. This is, again, the result of changing the burning velocity at the vicinity of the cold wall.

7.2.1.3 Results

At this point the results of both simulations will be presented. The illustrations might have visual resemblance those presented by Gruber [46], which is intentional, in order to facilitate a comparison between the behavior of the hydrogen-air flame and the methane-air flame when interacting with the wall. Besides, most of the figures are normalized by the value of the freely propagating flamelet of the same mixture to give a clearer impression of magnitudes compared to HOQ.

The first step to analyze the flame-wall interaction in the side-wall configuration is to find out, where the flame quenches. This, of course, requires a quantitative criterion. One can say, the flame quenches where the heat flux at the wall reaches its maximum. Based on the results already obtained from the head-on configuration, we know also the H_2O_2

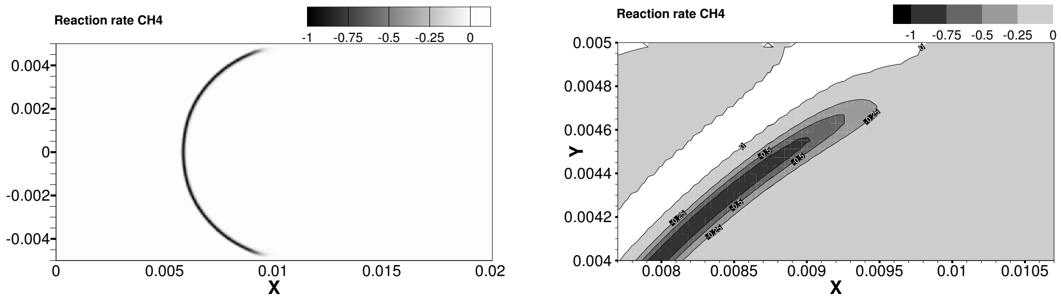

(a) Transient (b) Transient - magnified

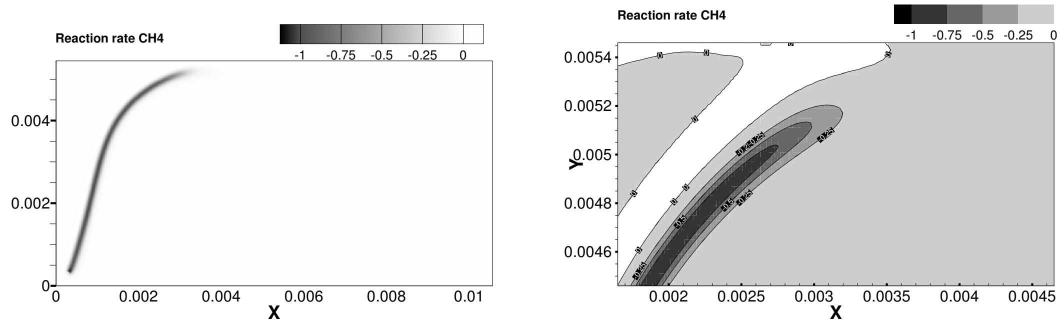

(c) pilot-stabilized (d) pilot-stabilized - magnified

Figure 7.8: Comparison of reaction rates of methane. Field is normalized by corresponding value in a freely propagating laminar flamelet. Top-left: reaction rate of CH_4 in transient configuration. Bottom-left: the same quantity in pilot-stabilized configuration. Top- and bottom-right: magnified version of the left plot at quenching point.

attains its maximum. This gives a clear definition of the quenching point.

REACTION RATE OF CH4

Figure 7.8 demonstrates contours and iso-lines of the instantaneous CH_4 reaction rate, normalized with respect to corresponding parameter of the freely propagating flamelet. In figures 7.8a and 7.8c, although the reaction rate of methane is of the same order as the stationary one-dimensional flamelet, this rate seems to be higher in the pilot-stabilized configuration. This difference might be a momentarily effect due to different burning velocities of the mixture along the flame front in the two configurations. Despite that, both configurations behave similarly in the vicinity of the wall, where the flame quenches. This can be seen in figures 7.8b and 7.8d. In both flames near the wall, the reaction rate of CH_4 vanishes. This is also demonstrated in the work of Gruber for hydrogen-air flame.

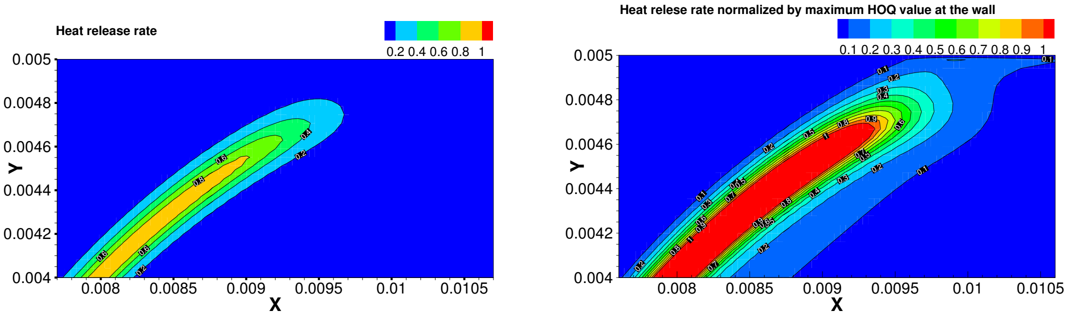

(a) Transient - norm. by flamelet value (b) Transient - norm. by HOQ value

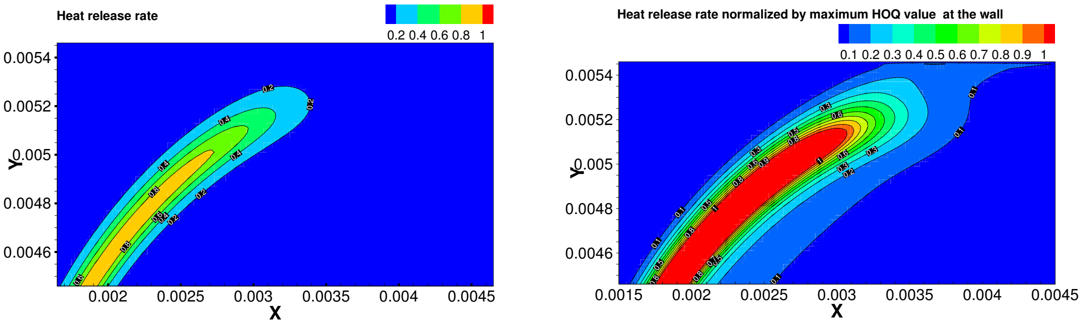

(c) pilot-stabilized - norm. by flamelet value (d) pilot-stabilized - norm. by HOQ value

Figure 7.9: Contour plots of heat release rate. Right: fields are normalized by maximum value at quenching moment in head-on quenching configuration. Left: fields are normalized by the value obtained in a freely propagating flamelet. Up-Transient side-wall quenching. Down-pilot-stabilized side-wall quenching.

HEAT RELEASE RATE

Figure 7.9 indicates instantaneous snapshots of the heat release rate contours for both side-wall quenching configurations. Left figures, demonstrate the heat release rate filed, which is normalized by the maximum value of the heat release rate of freely propagating flame. Obviously, the heat release rate in both configurations tends to zero at the wall. This means that the flame does not exist there anymore. This observation has not been reported by Gruber for the hydrogen-air flame, which has a second reaction mode. The second reaction mode in that flame was the result of the radical recombination in the exothermic reactions of the hydrogen mechanism used for that particular simulation. That shows, contrary to hydrogen, methane-air flame does not result a secondary increasing mode of the heat release rate at the wall. To provide more information on the comparison of the side-wall quenching in the head-on quenching configuration, heat release rate has been also normalized, this time, by the maximum value of the heat release rate at the moment when the one-dimensional flame quenches in the head-on configuration. This can be seen in figures 7.9b and 7.9d.

Comparing these two figures with 7.3a gives better understanding of the flame in the proximity of the wall, when the flow direction is parallel to the wall. Looking at both figures, one can see that the heat release in both configurations show similar behavior. It is considerably lower next to the wall. Interestingly, the maximum value of the head-on quenching takes place at 0.2 $[mm]$ distance from the wall. This value also confirms that the heat release rate near the wall is dramatically lower than that of HOQ configuration.

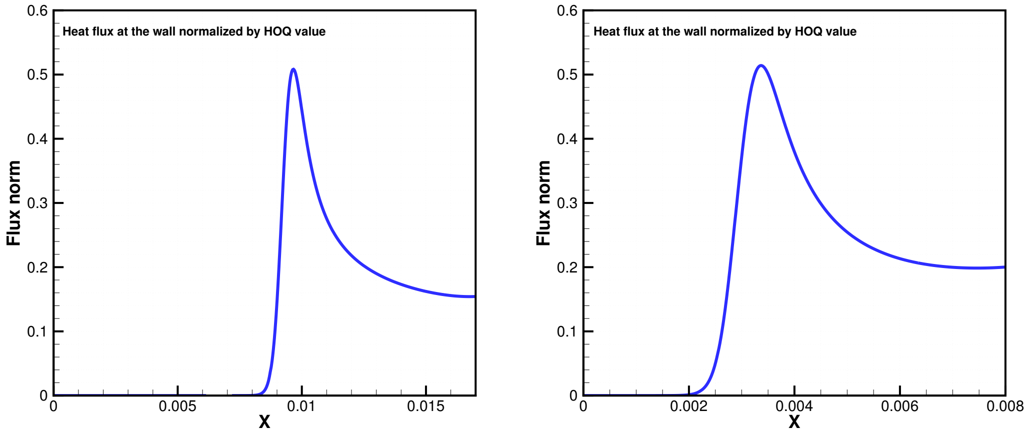

(a) Φ_w - Transient (b) Φ_w - pilot-stabilized

Figure 7.10: Normalized heat flux at the wall along the domain length. Normalization has been done by the heat flux calculated for the head on quenching. Left-Transient SWQ configuration. Right-pilot-stabilized.

HEAT FLUX TO THE WALL

As explained at the beginning of this chapter, one of the most important aspects of near-wall combustion is the heat flux at the wall in flame-wall interaction. This heat transfer is believed to be the reason for quenching. To compare the heat flux in the SWQ with HOQ, first, its value from head-on quenching should be known. Equation 7.2 yields the heat flux to the wall, at the quenching moment for that configuration, which is obtained as $\Phi_q = 0.58\,[MWm^{-2}]$.

Based on this, one can normalize the heat flux to the wall in side-wall quenching configuration. Extracting the heat flux to the wall, at the last cell next to the wall and normalizing it to the corresponding value leaves us with what can be observed in figure 7.10. Interestingly, both configurations reached exactly the same value of heat flux at their maximum. This means, the maximum heat flux to the wall is not dependent on the SWQ-configuration, but on the mixture. It can be seen in both figures that the heat flux at the wall increases suddenly and reaches its maximum exactly, where the flame is located to quench.

Downstream from the maximum, the burnt flame cools down along the channel and due to the heat flux to the wall, until it reaches 40% of its value in the transient configuration and 50%, in the pilot-stabilized. This difference between two configurations might be because of the different lengths, along which the flame is able to cool down. That could also be due to the short length of the simulation domain, which is to make sure the simulation will not be affected by the outflow boundary condition. This means, both simulations might yield the same results for heat flux at outlet, if their domain has the same length.

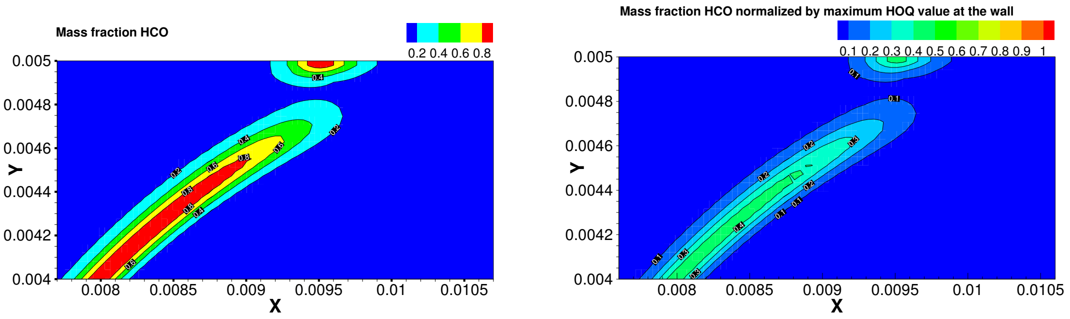

(a) Transient - norm. by flamelet value (b) Transient - norm. by HOQ value

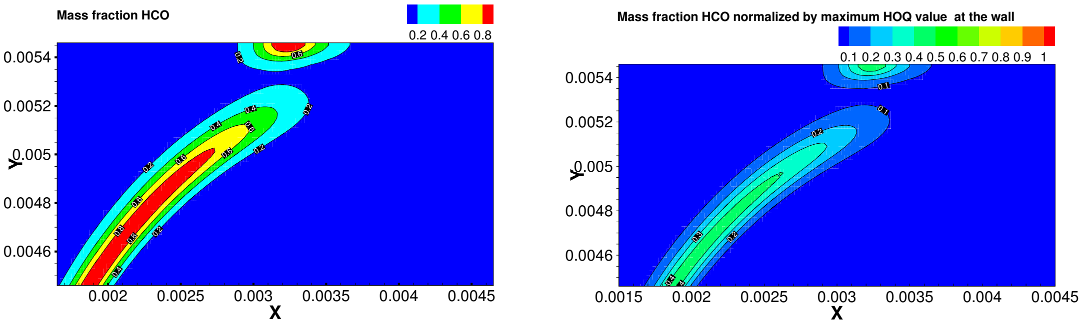

(c) pilot-stabilized - norm. by flamelet value (d) pilot-stabilized - norm. by HOQ value

Figure 7.11: Comparison of the contours plotted for the mass fraction of the HCO. Right-Both fields are normalized by the corresponding maximum value of HCO at quenching moment in the head-on quenching configuration presented before in this chapter. Left-Both fields are normalized by the value of the same parameter in a freely propagating flamelet. Up-Transient side-wall quenching. Down-pilot-stabilized side-wall quenching.

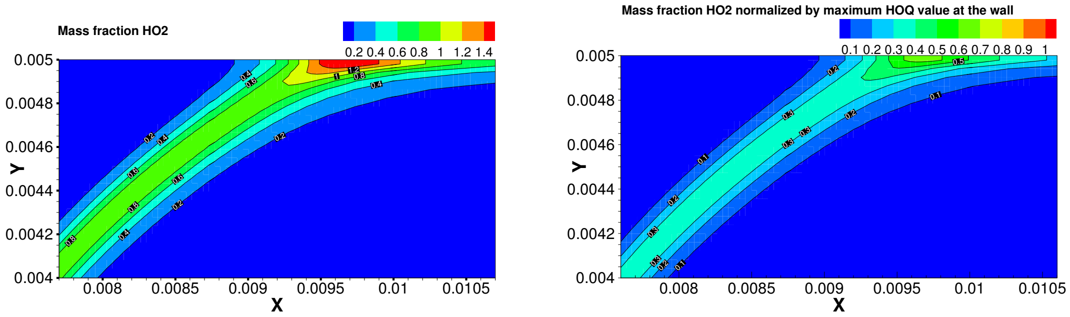

(a) Transient - norm. by flamelet value

(b) Transient - norm. by HOQ value

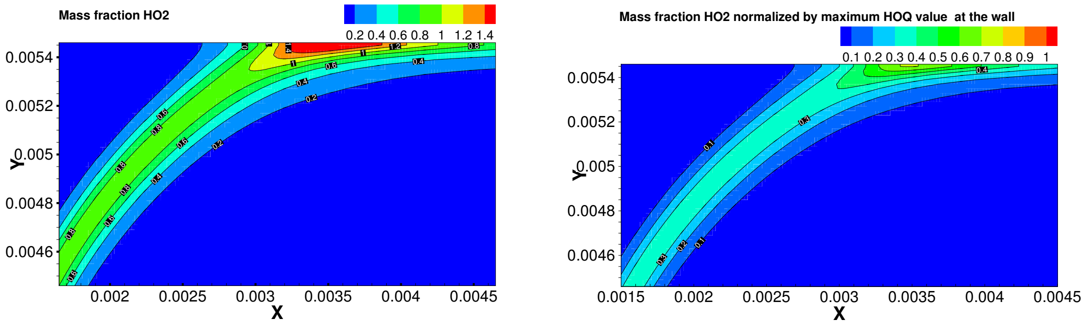

(c) pilot-stabilized - norm. by flamelet value

(d) pilot-stabilized - norm. by HOQ value

Figure 7.12: Comparison of the contours plotted for the mass fraction of the HO_2. Right-Both fields are normalized by the corresponding maximum value of HO_2 at quenching moment in the head-on quenching configuration presented before in this chapter. Left-Both fields are normalized by the value of the same parameter in a freely propagating flamelet. Up-Transient side-wall quenching. Down-pilot-stabilized side-wall quenching.

MASS FRACTION OF HCO

The second reaction mode, observed in the DNS of hydrogen-air flame in side-wall configuration by Gruber is cannot be observed in the methane-air simulation. Nevertheless, the contours of HCO mass fraction reveal that it attains a second peak, at the point where the temperature gradient reaches its maximum in the proximity of the wall. This means, it decreases toward the wall and again locally increases at the quenching point. This might be because of the radical recombination at the cold wall, so that it prevents the HCO to be consumed at the cold wall. Similar local growth is seen in the head-on configuration, which indicates that the global SWQ phenomenon follows a similar process as HOQ.

MASS FRACTION OF HO2

Figure 7.12 shows that the mass fraction of HO_2 increases exactly at the point where it has been determined as the quenching point of the flame. This confirms that, the combustion near the wall, in the SWQ configurations, follows similar pathway as HOQ, and this accumulation has also been observed there. At the neighborhood of the wall, where the flame-wall distance reduces and the flame is affected by the cold wall, because of the heat flux to the wall the sequence of the reaction mechanism changes. That means the mass fraction profile of HO_2 is ahead of others, except H_2O_2 which is the result of the reaction of HO_2 itself, and is the first species to meet the wall. There, HO_2 has only the opportunity to diffuse toward the wall and not back into the flame. This confirms again, the high impact of the reactions (7.14) and (7.15) which overtake the other reactions and make the radicals recombine and stop the process.

In both transient- and pilot-stabilized configurations, the HO_2 mass fraction is of the same order magnitude and slightly higher – around 50% – than that of the freely propagating flame. The same species, normalized by the maximum value of the HOQ, at the quenching moments shown in figures 7.12b and 7.12d, reveals that HO_2 accumulation in these configurations is less than HOQ. In side-wall quenching, although the HO_2 accumulates, it never reaches the same value as the HOQ. On the other hand, the accumulation is not only in a point but rather over an area of the domain. A cell-by-cell examination of the near-wall region shows that there is just one cell in which the heat flux reaches maximum (consequently also H_2O_2). However, where the heat flux to the wall is around one third of the flame power, it is said that the flame is under impact of the wall and quenches, which causes the HO_2 to increase within a sub-domain.

MASS FRACTION OF H2O2

Accumulated HO_2 in the proximity of the cold wall, where the flame loses heat, forces the mechanism to go through reaction (7.15), in which H_2O_2 is produced. This increases H_2O_2 value at the wall. This happens for both configurations alike. Here, the difference is that the H_2O_2 spreads over a broader area and not just one cell as in HOQ.

The mass fraction of this intermediate is shown in figure 7.13. Figures 7.13a and 7.13c demonstrate, that H_2O_2 concentration has the same order in both cases. But the maximum reached in the pilot-stabilized case is 25% higher than that in transient case. Indeed this is a momentarily and local increase of the H_2O_2 and is just because of the angle of the flame toward the wall. In fact, the angle at which the flame front meets the wall is wider in the pilot-stabilized case compared to the transient configuration. Therefore the instantaneous snapshot of the pilot-stabilized configuration has a closer resemblance to the HOQ configuration concerning the angle toward the wall.

Investigating the results obtained in other time steps supports this observation. It reveals that although the characteristics of a certain flame during the interaction with the wall and the related quantities remain the same, stabilizing the flame in the side-wall quenching is not that easy as the burning velocity at the wall is smaller than in the middle of the domain. Consequently, the flame tip at the wall reaches the wall with different angles. Although it might seem not that important, in the cases, like this laminar configuration, it could be significant in turbulent combustion. In such flow regimes the flame wrinkles and continuously changes its position and angle toward the wall and even the flame distance from the wall might change. Though the mean value of the parameters might be constant, but the fluctuating values have to be considered for calculating the material fatigue.

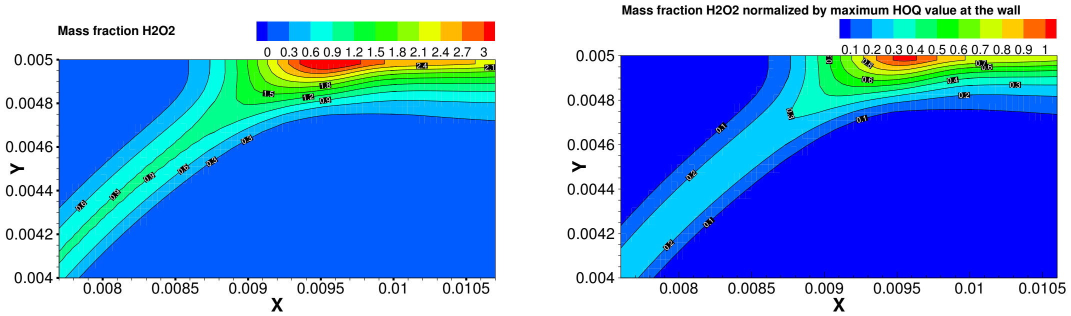

(a) Transient - norm. by flamelet value (b) Transient - norm. by HOQ value

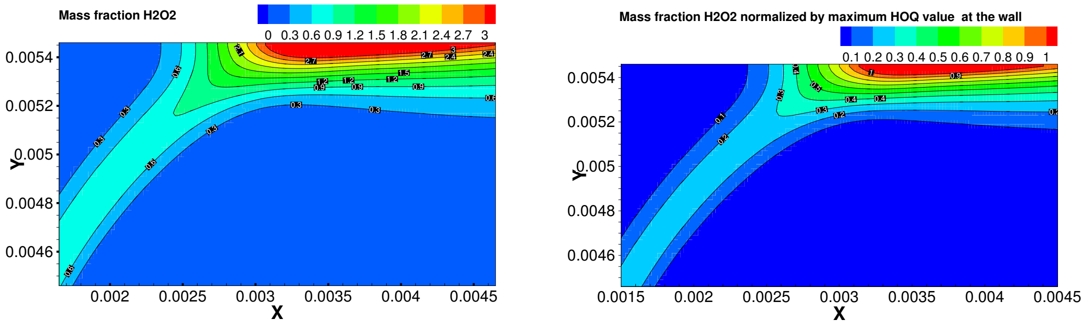

(c) pilot-stabilized - norm. by flamelet value (d) pilot-stabilized - norm. by HOQ value

Figure 7.13: Comparison of the contours plotted for the mass fraction of the H_2O_2. Right-Both fields are normalized by the corresponding maximum value of H_2O_2 at quenching moment in the head-on quenching configuration presented before in this chapter. Left-Both fields are normalized by the value of the same parameter in a freely propagating flamelet. Up-Transient side-wall quenching. Down-pilot-stabilized side-wall quenching.

7.2.1.4 Comparison of the CO production at the wall in head-on quenching with side-wall quenching

Figure 7.14 gives a qualitative comparison of CO production in head-on quenching and side-wall quenching, near the wall. For side-wall quenching a snapshot of data on nodes located at a specific distance from the wall was taken at a particular instant of time. For head-on quenching the plots are not based on data extracted from different grid points at a specific time instant (snapshot), but instead from different time steps at a fixed node. The node sits there and gathers data samples as the flame passes through. This method of sampling carries the same amount of information as a snapshot and is equally comprehensive.

The figures indicate that the two SWQ configurations have exactly the same overall behavior along the extraction lines, except at the far end, where they diverge. This divergence is not a physical effect due to configuration difference but rather the result of different domain sizes. Another reason could be the influence of the outflow. Far from the wall, especially at $1.7\,[mm]$, the side-wall quenching configurations reach the same maximum temperatures as the head-on quenching. CO is produced the most when temperature is approximately around $T \approx 1650\,[K]$, and is higher in SWQ than in HOQ.

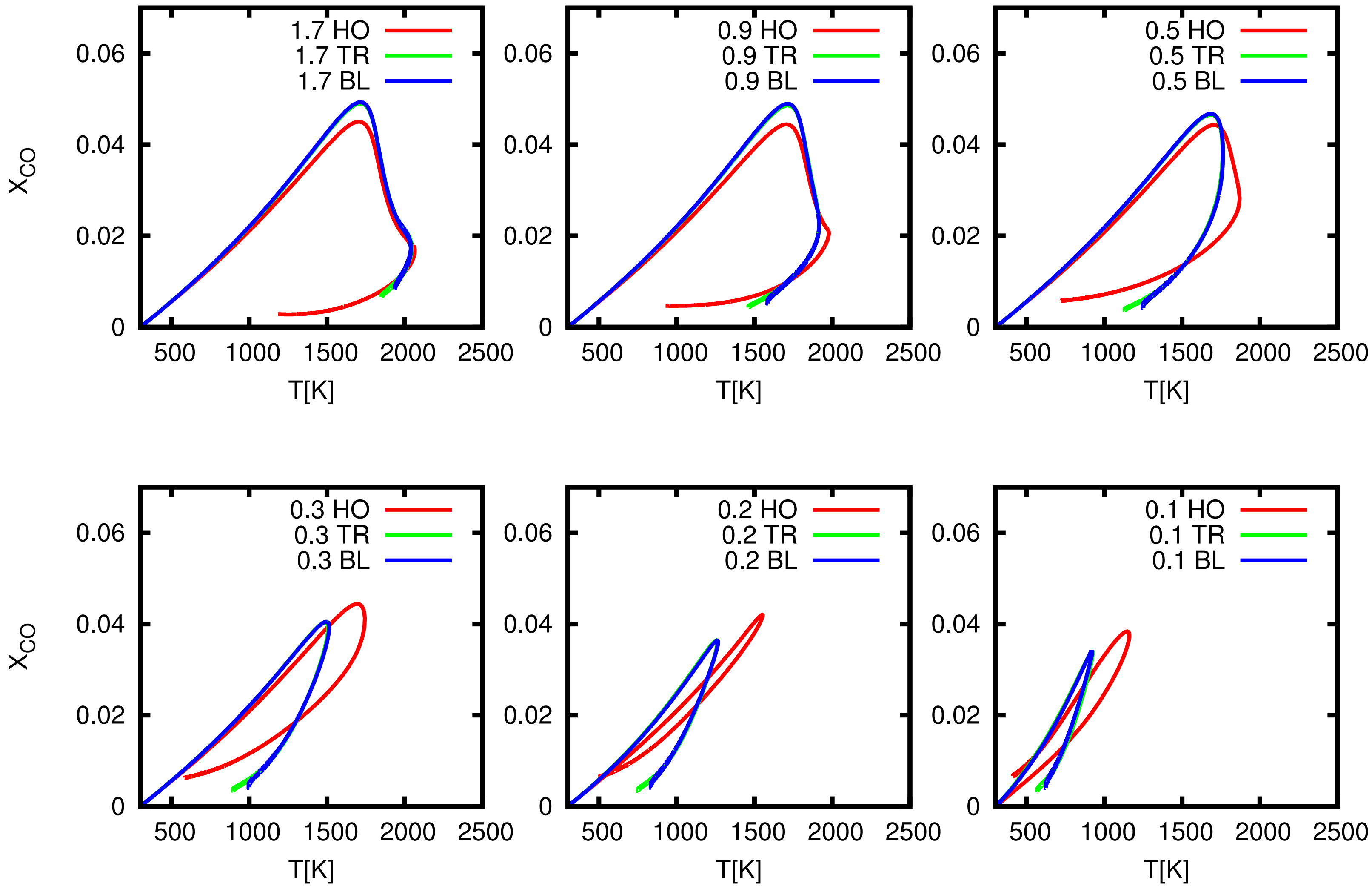

Figure 7.14: A qualitative comparison of the co production in head-on quenching configuration with the two different side-wall quenching configurations. Red lines- The CO scatter plots in head-on quenching configuration. Green- CO value extracted from a instantaneous snapshot at fixed mentioned along the channel of the transient side-wall quenching configuration. Blue- CO value plotted for pilot-stabilized SWQ. Data extraction similar to transient configuration

As the data extraction lines approach the wall the results deviate further from the scatter plots of the CO mole fraction. The highest temperature reached in one dimensional quenching remains always higher for the distances lower than $0.5\,[mm]$ from the wall. At $0.3\,[mm]$ distance the maximum temperature and the largest mass fraction belongs to head-on quenching by far. This might be the result of the direction of the flame toward the wall in HOQ, so that the flame can reach higher temperatures near the wall. The burning velocity of the mixture at these points in the side-wall quenching could also differ from the head-on quenching, while it remains the same as freely propagating laminar flamelet unless it enters the wall interaction zone.

7.2.1.5 Conclusion

One can generally say that the heat flux toward the wall is almost the same for both side-wall configurations, as is the rate of heat release near the wall and in the domain. The snapshots of the mass fractions of species in both SWQ configurations also follow the same trends near the wall. Slight differences are observed in the contour plots of HCO and H_2O_2, between the two SWQ configurations due to the angle between the flame tip and the wall. As this angle gets closer to 90 degrees, the mass fractions species grow larger at the wall.

Another point, is the accumulation of species near the wall in side-wall quenching. Although there is a point where heat flux toward the wall is the highest, since the flame sits on the wall and in the vicinity of these point there is still considerable heat flux toward the wall and the flame is still affected by the wall, these species got still high value in these neighborhood, compared to that in the middle of the domain.

Mass fractions of species HO_2, H_2O_2 and CO attain lower peaks in side-wall quenching than in head-on quenching. This behavior can be clearly seen in the scatter plots of CO mole fractions versus temperature.

Chapter 8

Summary

The objective of this work was to investigate the side-wall quenching of the laminar premixed flame in a quasi three-dimensional configuration, performing direct numerical simulations coupled with a multi-component chemical solver. To this end the three-dimensional in-house Navier-stokes solver, FASTEST-3D has been developed to be able to import the chemical source terms calculated by chemical solver. As the chemical solver, DASAC the non-ordinary differential equation solver, built in SENKIN, was used. The SENKIN itself is a sub-program packet of the CHEMKIN.

The readily available code was modified to calculate the mixture averaged flow properties of a gas mixture including density, mean molar mass, etc. The code was then extended to include mass fraction and energy transport equations for a multi-component gas mixture. Two different methods for calculation of the transport properties have been implemented, namely $\mathrm{Le} = 1$ and mixture averaged. These methods have a strong impact on calculation of the laminar burning velocity of the flame.

The developed program was then verified based on the accuracy of source terms, the convective term, and the diffusion term in chemical and energy equations. A general one-dimensional test case was employed to verify the code by comparing its results to the widely used one-dimensional flamelet generator Chem1D.

The code was then examined for a stoichiometric laminar methane-air flame taking the Le number equal to one to compute the transport coefficients. This step was carried out successfully and the results were in excellent agreement with those of Chem1D based on mass fractions of the species. Moving on to the next level of complexity in calculation of transport coefficient namely the mixture averaged, the same test case was used putting in lean, stoichiometric, and rich configurations where again the code was in good agreement with Chem1D especially for cells finer than $25\,[\mu m]$. A two-dimensional test case was then taken to see how the results keep up in multi-dimensional cases. Again the results showed high accuracy in the same sense. Thus far, the code was able to simulate and predict different modes of combustion from premixed, stratified- and triple-flames, to pure diffusion flames with high accuracy.

To further study the near-wall combustion, the Smooke mechanism was employed in a head-on quenching configuration. A one-dimensional head-on quenching configuration for the stoichiometric methane-air flame was simulated in a one-dimensional DNS setting. The results were exact match to the same simulation reported by Popp et al. [103]. The choice of mechanism correctly predicted the maximum heat flux at the wall, and the mechanism path fits precisely to the quenching pathway. Accumulation of HO_2 and H_2O_2 was successfully predicted. It was indicated that the heat flux toward the wall and the radical recombination change the mechanism pathway, and are responsible for flame quenching.

Moreover, the results confirmed that our choice of chemical mechanism remains completely valid and functional in post-quenching phase. This makes it possible to completely simulate the flame-wall interaction in a wide variety of configurations.

The head-on quenching simulation was compared to the experimental data reported by Mann et al. [87]. Scatter plots of CO mole fractions versus temperature were compared in different distances from the wall. The results show very good agreement in the pre-heat zone but for the post-flame zone there were discrepancies except far from the wall where flame is not actually affected by the wall. Both cases indicate that this deviation could be due to the following reasons:

1. deviation of convective velocities in the simulation from the measurement,
2. complexity of the multi-component mechanism,
3. neglecting the Soret and Dofour effects, and
4. limited measurement precision.

Next, two direct numerical simulations of flame-wall interaction were performed in the case where the flow is parallel to the wall. Transient configuration of the side-wall quenching was modeled in which the flame is allowed to move freely within the domain. Then a pilot-stabilized configuration of the side-wall quenching was considered. These results were extensively compared to the results from head-on quenching in order to understand how side-wall quenching differs from from head-on quenching in terms of maximum heat flux to the wall, heat release rate in the neighborhood of the wall, the quality of the quenching concerning the multi-component mechanism, and the influence of species on quenching. The two simulations show similar behavior in how the heat release rate increases. The second mode of reaction which can be seen in DNS of the turbulent premixed hydrogen-air combustion cannot be seen in these configurations. Similar to Gruber's reports for the hydrogen flame in a similar setting, the reaction rate of methane completely vanished near the wall. The heat fluxes at the wall normalized with respect to the corresponding value in head-on quenching coincide for the two configurations. The location where heat flux reaches its maximum is also the point where the reaction rate of the methane disappears. One would say that this point is the quenching point.

An instantaneous snapshot of mass fractions of important species in near-wall combustion was acquired from simulations. One again, similarities between the two side-wall quenching cases were observed. Most interestingly, the HCO contour at the quenching area decreases and then a increases locally. The same behavior is observed in head-on quenching configuration. The HCO contours were in agreement for both configurations. In the case of HO_2 and H_2O_2, the local areas of accumulation were observed. This confirmed that the side-wall quenching follows the same chemical pathway as the head-on quenching. At the quenching point where H_2O_2 accumulates, the pilot-stabilized side-wall quenching predicts the same order of magnitude for H_2O_2, only slightly higher. This might be a momentary effect of the angle between the flame front and the wall.

The heat flux to the wall for both side-wall quenching configurations was almost half the value obtained for the head-on configuration. The heat release rate at the wall in side-wall quenching and the mass fractions of the aforementioned species show higher values in head-on quenching compared to side-wall quenching.

Finally, to examine the mole fraction of CO near the wall in side-wall quenching, its values were extracted along six equidistant lines extended through the flame parallel to the wall all the way from inlet to outlet. These values were then plotted against temperature overlaid upon the scatter plots of CO obtained from head-on quenching simulations. The two side-wall quenching configurations delivered the exact same plots up to a deviation at the far end of the curve. This was due to different lengths of the domain. The results revealed very good agreement with those of head-on quenching far from the wall. But as the extraction lines get closer to the wall, the discrepancy grows so that the head-on quenching reaches considerably higher temperature and also higher CO concentrations at the wall especially in the post flame zone.

Chapter 9

Outlook

Although the results of our implementation were in very good agreement with the available experimental and DNS data in different combustion modes; from diffusion flames to fully premixed and partially premixed flames, triple flames, and even stratified flames; there is obviously room for improvement and further investigation as is the case for any scientific work. Here we would like to address few possible extensions towards which further research can be directed.

The first issue that comes to mind is implementing an adaptive time stepping, since in principle any direct numerical simulation of flame-wall interaction requires very small time steps, especially at the beginning of simulation where convergence is not attained and simulation is susceptible to initialization. This could improve the computing performance drastically.

Another candidate for extension of the present project would be to equip the code with more sophisticated versions of transport coefficients which, for instance, include cross diffusion effects, or the Soret and Dofour effects. The mass and temperature gradients can grow very large in flame-wall interaction, especially if the wall temperature is higher than $700\,[K]$ or continuously varies, as it does in internal combustion engines. Therefore it makes complete sense to at least include the cross diffusion effects. Also a more powerful, complex, and detailed multi-component mechanism like **GRI-3.0** can be chosen to examine the dependency of solution on the mechanism.

And finally the elephant in the room: one could venture to perform a direct numerical simulation of the interaction of a turbulent premixed methane-air flame with the wall using a multi-component chemistry mechanism coupled with a complex transport coefficient method, e.g. including the Soret and Dofour effect, in a side-wall quenching configuration. This simulation would be computationally much more expensive at this time, however it would serve as an significant development in near-wall combustion research.

Appendix A

Reaction mechanism for H_2 combustion

Reaction no.	**Reaction**	**A**	β	E_a
1	H+O2+M=HO2+M	3.61E17	-0.72	0.
	H2O/18.6/ H2/2.86/			
2	H+H+M=H2+M	1.0E18	-1.0	0.
3	H+H+H2=H2+H2	9.2E16	-0.6	0.
4	H+H+H2O=H2+H2O	6.0E19	-1.25	0.
5	H+OH+M=H2O+M	1.6E22	-2.0	0.
	H2O/5/			
6	H+O+M=OH+M	6.2E16	-0.6	0.
	H2O/5/			
7	O+O+M=O2+M	1.89E13	0.0	-1788.
8	H2O2+M=OH+OH+M	1.3E17	0.0	45500.
9	H2+O2=2OH	1.7E13	0.0	47780.
10	OH+H2=H2O+H	1.17E9	1.3	3626.
11	O+OH=O2+H	3.61E14	-0.5	0.
12	O+H2=OH+H	5.06E4	2.67	6290.
13	OH+HO2=H2O+O2	7.5E12	0.0	0.
14	H+HO2=2OH	1.4E14	0.0	1073.
15	O+HO2=O2+OH	1.4E13	0.0	1073.
16	2OH=O+H2O	6.0E+8	1.3	0.
17	H+HO2=H2+O2	1.25E13	0.0	0.
18	HO2+HO2=H2O2+O2	2.0E12	0.0	0.
19	H2O2+H=HO2+H2	1.6E12	0.0	3800.
20	H2O2+OH=H2O+HO2	1.0E13	0.0	1800.

Table A.1: Hydrogen-air reaction mechanism.

Bibliography

[1] Tareq M Alshaalan and Christopher J Rutland. Turbulence, scalar transport, and reaction rates in flame-wall interaction. In *Symposium (International) on Combustion*, volume 27, pages 793–799. Elsevier, 1998.

[2] John David Anderson. *Computational Fluid Dynamics: The Basics With Applications*. McGraw-Hill Education, 1995.

[3] John David Anderson and JF Wendt. *Computational fluid dynamics*, volume 206. Springer, 1995.

[4] S Arrhenius. On the reaction rate of the inversion of non-refined sugar upon souring. *Z Phys Chem*, 4:226–248, 1889.

[5] Ivo Babuska and J Tinsley Oden. Verification and validation in computational engineering and science: basic concepts. *Computer Methods in Applied Mechanics and Engineering*, 193(36):4057–4066, 2004.

[6] M Bellenoue, T Kageyama, SA Labuda, and J Sotton. Direct measurement of laminar flame quenching distance in a closed vessel. *Experimental thermal and fluid science*, 27(3):323–331, 2003.

[7] M Bellenoue, T Kageyama, SA Labuda, and J Sotton. Direct measurement of laminar flame quenching distance in a closed vessel. *Experimental thermal and fluid science*, 27(3):323–331, 2003.

[8] R Byron Bird, Warren E Stewart, and Edwin N Lightfoot. *Transport phenomena*. John Wiley & Sons, 2007.

[9] RICHARD J BLINT and JAMES H BECHTEL. Flame/wall interface: theory and experiment. *Combustion Science and Technology*, 27(3-4):87–95, 1982.

[10] RJ Blint and JH Bechtel. Hydrocarbon combustion near a cooled wall. Technical report, SAE Technical Paper, 1982.

[11] B Boust, J Sotton, SA Labuda, and M Bellenoue. A thermal formulation for single-wall quenching of transient laminar flames. *Combustion and flame*, 149(3):286–294, 2007.

[12] Kathryn Eleda Brenan, Stephen L Campbell, and Linda Ruth Petzold. *Numerical solution of initial-value problems in differential-algebraic equations*, volume 14. Siam, 1996.

[13] John Charles Butcher. *The numerical analysis of ordinary differential equations: Runge-Kutta and general linear methods*. Wiley-Interscience, 1987.

[14] RS Cant and Epaminondas Mastorakos. *An introduction to turbulent reacting flows*. World Scientific, 2008.

[15] Yunus A Cengel, Michael A Boles, and Mehmet Kanoglu. *Thermodynamics: an engineering approach*, volume 1056. McGraw-Hill New York, 1998.

[16] Jacqueline H Chen. Petascale direct numerical simulation of turbulent combustion – fundamental insights towards predictive models. *Proceedings of the Combustion Institute*, 33(1):99–123, 2011.

[17] JH Chen, A Choudhary, B De Supinski, M DeVries, ER Hawkes, S Klasky, WK Liao, KL Ma, J Mellor-Crummey, N Podhorszki, et al. Terascale direct numerical simulations of turbulent combustion using s3d. *Computational Science & Discovery*, 2(1):015001, 2009.

[18] RK Cheng, RG Bill Jr, and F Robben. Experimental study of combustion in a turbulent boundary layer. In *Symposium (International) on Combustion*, volume 18, pages 1021–1029. Elsevier, 1981.

[19] Alexandre J Chorin and Jerrold E Marsden. A mathematical introduction to fluid dynamics, 1993.

[20] Alexandre Joel Chorin. Numerical solution of the navier-stokes equations. *Mathematics of computation*, 22(104):745–762, 1968.

[21] TJ Chung. *Computational fluid dynamics*. Cambridge university press, 2010.

[22] TJ Chung. *Computational fluid dynamics*. Cambridge university press, 2010.

[23] Charles W Clendening Jr, William Shackleford, and Rodger Hilyard. Raman scattering measurements in a side-wall quench layer. In *Symposium (International) on Combustion*, volume 18, pages 1583–1590. Elsevier, 1981.

[24] I Connelly, T Ogasawara, D Lee, R Greif, RF Sawyer, and OA Ezekoye. Fall meeting western states section of the combustion institute, wsci 93-077, 1993.

[25] L Connelly, R Greif, RF Sawyer, and D Lee. Fall meeting. *Combustion Institute/Western States Section, Berkeley, CA*, pages 92–109, 1992.

[26] F Dabireau, Benedicte Cuenot, O Vermorel, and Thierry Poinsot. Interaction of flames of h< sub> 2</sub>+ o< sub> 2</sub> with inert walls. *Combustion and flame*, 135(1):123–133, 2003.

[27] WA Daniel. Flame quenching at the walls of an internal combustion engine. In *Symposium (International) on Combustion*, volume 6, pages 886–894. Elsevier, 1957.

[28] LPH de Goey, JA van Oijen, RTE Hermanns, and H Bongers. Chem1d: a package for the simulation of one-dimensional flames, 2003.

[29] G Desoutter, B Cuenot, C Habchi, and T Poinsot. Interaction of a premixed flame with a liquid fuel film on a wall. *Proceedings of the Combustion Institute*, 30(1):259–266, 2005.

[30] F Durst and M Schäfer. A parallel block-structured multigrid method for the prediction of incompressible flows. *International Journal for Numerical Methods in Fluids*, 22(6):549–565, 1996.

[31] Masaru Enomoto. Head-on quenching of a premixed flame on the single wall surface. *JSME International Journal Series B*, 44(4):624–633, 2001.

[32] Bernd Epple, Reinhard Leithner, Wladimir Linzer, and Heimo Walter. *Simulation Von Kraftwerken Und Warmetechnischen Anlagen.* Springer-Verlag, 2009.

[33] Alexandre Ern and Vincent Giovangigli. *Multicomponent transport algorithms*, volume 24. Springer Science & Business Media, 1994.

[34] Jesús Contreras Espada. *Numerical Simulation of Reacting Flows Under Laminar Conditions with Detailed Chemistry.* dissertation, TU Darmstadt, 2010.

[35] O Ezekoye, R Greif, and RF Sawyer. Increased surface temperature effects on wall heat transfer during unsteady flame quenching. In *Symposium (International) on Combustion*, volume 24, pages 1465–1472. Elsevier, 1992.

[36] OA Ezekoye. Heat transfer consequences of condensation during premixed flame quenching. *Combustion and flame*, 112(1):266–269, 1998.

[37] OA Ezekoye and R Greif. A comparison of one and two dimensional flame quenching: heat transfer results. Technical report, Lawrence Berkeley Lab., CA (United States), 1993.

[38] Joel H Ferziger and Milovan Perić. *Computational methods for fluid dynamics*, volume 3. Springer Berlin, 2002.

[39] Advisory Council for Aeronautics Research in Europe (ACARE). Aeronautics and air transport: beyond vision 2020 (towards 2050). Technical report, ACARE, 2010.

[40] Raymond Friedman and WC Johnston. The wall-quenching of laminar propane flames as a function of pressure, temperature, and air-fuel ratio. *Journal of Applied Physics*, 21(8):791–795, 1950.

[41] Raymond Friedman and WC Johnston. Pressure dependence of quenching distance of normal heptane, iso-octane, benzene, and ethyl ether flames. *The Journal of Chemical Physics*, 20(5):919–920, 1952.

[42] Shoichi Furuhama and Yoshiteru Enomoto. Heat transfer into ceramic combustion wall of internal combustion engines. Technical report, SAE Technical Paper, 1987.

[43] Irvin Glassman, Richard A Yetter, and Nick G Glumac. *Combustion*. Academic press, 2014.

[44] Pierre-Alexandre Glaude, Frédérique Battin-Leclerc, René Fournet, Valérie Warth, Guy-Marie Côme, and Gérard Scacchi. Construction and simplification of a model for the oxidation of alkanes. *Combustion and Flame*, 122(4):451–462, 2000.

[45] KA Green and JT Agnew. Quenching distances of propane-air flames in a constant-volume bomb. *Combustion and Flame*, 15(2):189–191, 1970.

[46] A Gruber, R Sankaran, ER Hawkes, and JH Chen. Turbulent flame–wall interaction: a direct numerical simulation study. *Journal of Fluid Mechanics*, 658:5–32, 2010.

[47] Andrea Gruber, Prashant S Salimath, and Jacqueline H Chen. Direct numerical simulation of laminar flame–wall interaction for a novel h 2-selective membrane/injector configuration. *International Journal of Hydrogen Energy*, 39(11):5906–5918, 2014.

[48] Margaret E Harris, Joseph Grumer, Guenther von Elbe, and Bernard Lewis. Burning velocities, quenching, and stability data on nonturbulent flames of methane and propane with oxygen and nitrogen: Application of theory of ignition, quenching, and stabilizationto flames of propane and air. In *Symposium on Combustion and Flame, and Explosion Phenomena*, volume 3, pages 80–89. Elsevier, 1949.

[49] C Hasse, M Bollig, N Peters, and HA Dwyer. Quenching of laminar iso-octane flames at cold walls. *Combustion and flame*, 122(1):117–129, 2000.

[50] Evatt R Hawkes and Jacqueline H Chen. Direct numerical simulation of hydrogen-enriched lean premixed methane–air flames. *Combustion and Flame*, 138(3):242–258, 2004.

[51] Martin Hertzberg. The theory of flammability limits. *Natural Convection. RI*, 8127, 1976.

[52] Charles Hirsch. *Numerical Computation of Internal and External Flows: The Fundamentals of Computational Fluid Dynamics: The Fundamentals of Computational Fluid Dynamics*, volume 1. Butterworth-Heinemann, 2007.

[53] JD Hirschfelder. Curtis. *CoT., and Bird, RB, Molecular Theory of Gases and Liquids, John iley and Sons, New York*, 1954.

[54] W Hocks, N Peters, and G Adomeit. Flame quenching in front of a cold wall under two-step kinetics. *Combustion and Flame*, 41:157–170, 1981.

[55] WM Huang, SR Vosen, and R Greif. Heat transfer during laminar flow flame quenching: effect of fuels. Technical report, Lawrence Berkeley Lab., CA (USA), 1985.

[56] Frank P Incropera. *Fundamentals of heat and mass transfer*. John Wiley & Sons, 2011.

[57] Frank P Incropera. *Introduction to heat transfer*. John Wiley & Sons, 2011.

[58] Jósef Jarosiński. Flame quenching by a cold wall. *Combustion and Flame*, 50:167–175, 1983.

[59] Jozef Jarosinski, Jerzy Podfilipski, and Tadeusz Fodemski. Properties of flames propagating in propane-air mixtures near flammability and quenching limits. *Combustion science and technology*, 174(1):167–187, 2002.

[60] Mark J Jennings. Multi-dimensional modeling of turbulent premixed charge combustion. Technical report, SAE Technical Paper, 1992.

[61] Mark J Jennings and Thomas Morel. A computational study of wall temperature effects on engine heat transfer. Technical report, SAE Technical Paper, 1991.

[62] Theodore von Kármán and Gregorio Millán. Thermal theory of a laminar flame front near a cold wall. In *Symposium (International) on Combustion*, volume 4, pages 173–177. Elsevier, 1953.

[63] RJ Kee, G Dixon-Lewis, J Warnatz, ME Coltrin, JA Miller, and HK Moffat. Transport: a software package for the evaluation of gas-phase, multicomponent transport properties. *Chemkin Collection*, 1999.

[64] Robert J Kee, Michael E Coltrin, and Peter Glarborg. *Chemically reacting flow: theory and practice*. John Wiley & Sons, 2005.

[65] Robert J Kee, Joseph F Grcar, MD Smooke, JA Miller, and E Meeks. Premix: a fortran program for modeling steady laminar one-dimensional premixed flames. *Sandia National Laboratories Report*, 1985.

[66] Robert J Kee, Fran M Rupley, and James A Miller. Chemkin-ii: A fortran chemical kinetics package for the analysis of gas-phase chemical kinetics. Technical report, Sandia National Labs., Livermore, CA (USA), 1989.

[67] Thomas M Kiehne, Ronald D Matthews, and Dennis E Wilson. The significance of intermediate hydrocarbons during wall quench of propane flames. In *Symposium (International) on Combustion*, volume 21, pages 481–489. Elsevier, 1988.

[68] Wolfgang Kollmann. Computational fluid dynamics. *Washington, DC, Hemisphere Publishing Corp., 1980. 616 p (For individual items see A80-37231 to A80-37239)*, 1, 1980.

[69] MA Kramer, JM Calo, H Rabitz, and RJ Kee. Aim: the analytically integrated magnus method for linear and second-order sensitivity coefficients. Technical report, Sandia Labs., Livermore, CA (USA), 1982.

[70] Mark A Kramer, Herschel Rabitz, Joseph M Calo, and Robert J Kee. Sensitivity analysis in chemical kinetics: Recent developments and computational comparisons. *International Journal of Chemical Kinetics*, 16(5):559–578, 1984.

[71] Erwin Kreyszig. *Advanced engineering mathematics*. John Wiley & Sons, 1988.

[72] Erwin Kreyszig. *Advanced engineering mathematics*. John Wiley & Sons, 2010.

[73] G Kuenne, A Ketelheun, and J Janicka. Les modeling of premixed combustion using a thickened flame approach coupled with fgm tabulated chemistry. *Combustion and Flame*, 158(9):1750–1767, 2011.

[74] Martin Wilhelm Kutta. Beitrag zur näherungsweisen integration totaler differentialgleichungen. *Zeitschrift für Mathematik und Physik 46: 435–453*, 1901.

[75] Sergei Labuda, Maxime Karrer, Julien Sotton, and Marc Bellenoue. Experimental study of single-wall flame quenching at high pressures. *Combustion Science and Technology*, 183(5):409–426, 2011.

[76] Chung K Law. *Combustion physics*. Cambridge University Press, 2006.

[77] T Lehnhäuser and M Schäfer. Improved linear interpolation practice for finite-volume schemes on complex grids. *International journal for numerical methods in fluids*, 38(7):625–645, 2002.

[78] Thomas Lehnhäuser. *Eine effiziente numerische Methode zur Gestaltsoptimierung von Strömungsgebieten*. Shaker, 2003.

[79] PJ Linstrom and WG Mallard. Nist chemistry webbook, nist standard reference database number 69, july 2001, national institute of standards and technology, gaithersburg, md 20899. *webbook. nist. gov*, 2014.

[80] JH Lu, O Ezekoye, R Greif, and RF Sawyer. Unsteady heat transfer during side wall quenching of a laminar flame. In *Symposium (International) on Combustion*, volume 23, pages 441–446. Elsevier, 1991.

[81] AE Lutz, RJ Kee, and JA Miller. Senkin: A Fortran Package for Predicting Homogenous Gas Phase, Chemical Kinetics, Sandia Report SAND87-8248. *UC4, Sandia, Livermore, California*, 1987.

[82] Andrew E Lutz, Robert J Kee, and James A Miller. Senkin: A fortran program for predicting homogeneous gas phase chemical kinetics with sensitivity analysis. Technical report, Sandia National Labs., Livermore, CA (USA), 1988.

[83] Ulrich Maas and Stephen B Pope. Simplifying chemical kinetics: intrinsic low-dimensional manifolds in composition space. *Combustion and Flame*, 88(3):239–264, 1992.

[84] Theodore H Maiman. Stimulated optical radiation in ruby. *Nature*, 187:493–494, 1960.

[85] G. M. Makhviladze and V. I. Melikov. *Flame propagation in a closed chanel with cold side wall.* UDC Plenum Publishing Corporation, 1991.

[86] Markus Mann. *Laserbasierte Untersuchung der Flamme-Wand-Interaktion.* Optimus-Verlag, 2013.

[87] Markus Mann, Christopher Jainski, Matthias Euler, Benjamin Böhm, and Andreas Dreizler. Transient flame–wall interactions: Experimental analysis using spectroscopic temperature and co concentration measurements. *Combustion and Flame*, 2014.

[88] Smooke M.D. and Giovangigli V. *Formulation of the premixed and non premixed test problems, in Reduced kinetic mechanisms and asymptotic approximations for methane-air flames.* Springer Verlag, 1991.

[89] Thomas Morel, Syed Wahiduzzaman, and Edward F Fort. Heat transfer experiments in an insulated diesel. Technical report, SAE Technical Paper, 1988.

[90] Kanury A Murty. *Introduction to combustion phenomena*, volume 2. CRC Press, 1975.

[91] William L Oberkampf and Christopher J Roy. *Verification and validation in scientific computing.* Cambridge University Press, 2010.

[92] JA van Oijen and LPH De Goey. Modelling of premixed laminar flames using flamelet-generated manifolds. *Combustion Science and Technology*, 161(1):113–137, 2000.

[93] Rebecca Owston, Vinicio Magi, and John Abraham. Interactions of hydrogen flames with walls: Influence of wall temperature, pressure, equivalence ratio, and diluents. *International Journal of Hydrogen Energy*, 32(12):2094–2104, 2007.

[94] Rebecca Owston, Vinicio Magi, and John Abraham. A numerical study of thermal and chemical effects in interactions of n-heptane flames with a single surface. *Combustion and flame*, 148(3):127–147, 2007.

[95] M Necat Ozisik. *Inverse heat transfer: fundamentals and applications.* CRC Press, 2000.

[96] Necati Ozisik. *Finite difference methods in heat transfer.* CRC press, 1994.

[97] Stanford S Penner. *Chemistry problems in jet propulsion*, volume 1. Pergamon Press, 1957.

[98] Norbert Peters. *Turbulent combustion.* Cambridge university press, 2000.

[99] Linda R Petzold. Description of dassl: a differential/algebraic system solver. Technical report, Sandia National Labs., Livermore, CA (USA), 1982.

[100] LR Petzold. Dassl code, version 1989. *Computing and Mathematics Research Division, Lawrence Livermore National Laboratory L*, 316, 1989.

[101] T. Poinsot and D. Veynante. *Theoretical and Numerical Combustion.* Edwards, 2005.

[102] TJ Poinsot, DC Haworth, and G Bruneaux. Direct simulation and modeling of flame-wall interaction for premixed turbulent combustion. *Combustion and Flame*, 95:118–132, 1993.

[103] P Popp and M Baum. Analysis of wall heat fluxes, reaction mechanisms, and unburnt hydrocarbons during the head-on quenching of a laminar methane flame. *Combustion and Flame*, 108(3):327–348, 1997.

[104] P Popp, M Smooke, and M Baum. Heterogeneous/homogeneous reaction and transport coupling during flame-wall interaction. In *Symposium (International) on Combustion*, volume 26, pages 2693–2700. Elsevier, 1996.

[105] CM Rhie and WL Chow. Numerical study of the turbulent flow past an airfoil with trailing edge separation. *AIAA journal*, 21(11):1525–1532, 1983.

[106] K Richter, R Friedrich, and L Schmitt. Large-eddy simulation of turbulent wall boundary layers with pressure gradient. In *6th Symposium on Turbulent Shear Flows*, volume 1, pages 22–3, 1987.

[107] Patrick J Roache. *Verification and validation in computational science and engineering.* Hermosa, 1998.

[108] Patrick J Roache. *Fundamentals of verification and validation.* hermosa publ., 2009.

[109] Michael Schäfer. *Numerik im Maschinenbau.* Springer-Verlag, 1999.

[110] Gregory P Smith, David M Golden, Michael Frenklach, Nigel W Moriarty, Boris Eiteneer, Mikhail Goldenberg, C Thomas Bowman, Ronald K Hanson, Soonho Song, William C Gardiner Jr, et al. Gri 3.0 mechanism. *Gas Research Institute (http://www. me. berkeley. edu/gri_ mech)*, 1999.

[111] MD Smooke, J Crump, K Seshadri, and V Giovangigli. Comparison between experimental measurements and numerical calculations of the structure of counterflow, diluted, methane-air, premixed flames. In *Symposium (International) on Combustion*, volume 23, pages 463–470. Elsevier, 1991.

[112] L MT SOMERS and LPH De Goey. A numerical study of a premixed flame on a slit burner. *Combustion science and technology*, 108(1-3):121–132, 1995.

[113] Richard Edwin Sonntag, Claus Borgnakke, Gordon John Van Wylen, and Steve Van Wyk. *Fundamentals of thermodynamics*, volume 6. Wiley New York, 1998.

[114] J Sotton, B Boust, SA Labuda, and M Bellenoue. Head-on quenching of transient laminar flame: heat flux and quenching distance measurements. *Combustion science and technology*, 177(7):1305–1322, 2005.

[115] JH Spurk. Strömungslehre-einführung in die theorie der strömungen, darmstadt, 1996.

[116] Herbert L Stone. Iterative solution of implicit approximations of multidimensional partial differential equations. *SIAM Journal on Numerical Analysis*, 5(3):530–558, 1968.

[117] Olaf Thiele, Stefan Seefeldt, Ing Robin Vanhaelst, et al. Measurement of in-cylinder mixture formation by optical indication. *MTZ worldwide*, 74(6):26–30, 2013.

[118] Stephen R Turns et al. *An introduction to combustion*, volume 287. McGraw-hill New York, 1996.

[119] JA Van Oijen, FA Lammers, and LPH De Goey. Modeling of complex premixed burner systems by using flamelet-generated manifolds. *Combustion and Flame*, 127(3):2124–2134, 2001.

[120] Jeroen van Oijen. *Flamelet-generated manifolds: development and application to premixed laminar flames.* Technische Universiteit Eindhoven, 2002.

[121] Gordon John Van Wylen, Richard Edwin Sonntag, and Gordon J Wylen. *Fundamentals of classical thermodynamics.* Wiley Singapore, 1985.

[122] Henk Kaarle Versteeg and Weeratunge Malalasekera. *An introduction to computational fluid dynamics: the finite volume method.* Pearson Education, 2007.

[123] SR Vosen, R Greif, and CK Westbrook. Unsteady heat transfer during laminar flame quenching. In *Symposium (International) on Combustion*, volume 20, pages 75–83. Elsevier, 1985.

[124] S Wahiduzzaman and T Morel. Effects of ceramics translucence on heat barrier effectiveness in diesel engines. Technical report, SAE Technical Paper, 1989.

[125] Jürgen Warnatz. The mechanism of high temperature combustion of propane and butane. *Combustion Science and Technology*, 34:177–200, 1983.

[126] Jürgen Warnatz, Ulrich Maas, and Robert W Dibble. *Combustion: physical and chemical fundamentals, modeling and simulation, experiments, pollutant formation.* Springer, 2006.

[127] JF Wehner. On the theory of flammability limits. *Combustion and Flame*, 7:309–313, 1963.

[128] Charles K Westbrook, Andrew A Adamczyk, and George A Lavoie. A numerical study of laminar flame wall quenching. *Combustion and Flame*, 40:81–99, 1981.

[129] Indrek S Wichman and Gilles Bruneaux. Head-on quenching of a premixed flame by a cold wall. *Combustion and flame*, 103(4):296–310, 1995.

[130] CR Wilke. A viscosity equation for gas mixtures. *The journal of chemical physics*, 18(4):517–519, 1950.

[131] F.A. Williams. *Combustion Theory: The Fundamental Theory of Chemically Reacting Flow Systems.* Combustion science and engineering series. Perseus Books Group, 1985.

[132] Forman Arthur Williams, Marcel Barrère, and NC Huang. Fundamental aspects of solid propellant rockets. Technical report, DTIC Document, 1969.

[133] Gerhard Woschni, Walter Spindler, and Konrad Kolesa. Heat insulation of combustion chamber walls – a measure to decrease the fuel consumption of ic engines? Technical report, SAE Technical Paper, 1987.

[134] KUO-CHUN WU and SIMONE HOCHGREB. The roles of chemistry and diffusion on hydrocarbon post-flame oxidation. *Combustion science and technology*, 130(1-6):365–398, 1997.

[135] Gang Zhou, Lars Davidson, and Erik Olsson. Transonic inviscid/turbulent airfoil flow simulations using a pressure based method with high order schemes. In *Fourteenth International Conference on Numerical Methods in Fluid Dynamics*, pages 372–378. Springer, 1995.

Lebenslauf

Name	Roozbeh Haghighi
Geburtsdatum	27.06.1979
Geburtsort	Teheran

Studium

09/1997 - 09/2003 **Tabriz Universität, Iran**

Fachrichtung: Mechanical Engineering
Vertiefung: Thermo and Fluid

Abschluss zum B.Sc.

10/2005 - 06/2008 **Ruhr-Universität Bochum**

Fachrichtung: Maschinenbau
Vertiefung: Energie- und Verfahrenstechnik

Abschluss zum Dipl.-Ing.

Wissenschaftlicher Mitarbeiter

11/2010 - 02/2015 **Technische Universität Darmstadt**

Wissenschaftlicher Mitarbeiter am Fachgebiet für Energie- und Kraftwerkstechnik (EKT)